



Universitat Autònoma  
de Barcelona

SPECTROSCOPY AND CONFOCAL IMAGING OF COMPLEX  
FERROIC SYSTEMS

Development of a Polarization Sensitive Confocal Microscope

Ondřej Vlašín

January 2014

Doctoral Thesis

SUPERVISOR

Gervasi Herranz

TUTOR

Javier Rodríguez Viejo

Universitat Autònoma de Barcelona  
Department of Physics, Faculty of Science  
Doctoral Program: Material Science

Institut de Ciència de Materials de Barcelona ICMAB-CSIC  
Laboratory of Multifunctional Oxides and Complex Structures

Ondřej Vlašín: *Spectroscopy and Confocal Imaging of Complex Ferroic Systems*, Development of a Polarization Sensitive Confocal Microscope, © 2014

**SUPERVISOR:**  
Gervasi Herranz

**LOCATION:**  
Barcelona

**TIME FRAME:**  
October 2009 - January 2014



Gervasi Herranz Casabona, Tenured Scientist at Insitut de Ciència de Materials de Barcelona and Javier Rodríguez Viejo, Applied Physics Professor at Universitat Autònoma de Barcelona

CERTIFY

that Ondřej Vlašín, Master in Physics, carried out under their direction work entitled "Spectroscopy and Confocal Imaging of Complex Ferroic Systems " and qualifies for the degree of Doctor in Material Science.

And for that record, sign this certificate

Bellaterra, January 2014

Dr. Gervasi Herranz Casabona

Prof. Javier Rodríguez Viejo



## ABSTRACT

---

New applications of ferroic systems often consider domain wall as carrier of information. Understanding of the nature of domain structure and its dynamics is therefore essential. At the same time the omnipresent need of keeping up with Moore law demands the dimensions of commercialized devices to decrease drastically. Hence the resolution of classical optical Kerr microscopy does not suffice anymore. Methods for studying domain dynamics at nanoscale are available, but are very time consuming and expensive. It's extremely complicated to measure both magnetic and electric properties simultaneously. This creates a need for an intermediate method that offers sub-micron lateral resolution and short measurement times, yet produces enough information about all ferroic properties of a system.

To address this issue we developed several optical methods that expand the possibilities of multiferroic characterization. An electric field frequency spectrum magneto-optical Kerr effect setup allows for an effective separation and quantification of surface and strain mediated magnetoelectric coupling effects as demonstrated on Co/ lead zirconate titanate (PZT) ferroic multilayers. Direct electro-magnetic domain mapping with sub-micron lateral resolution was made possible with cryostat ready polarization sensitive confocal microscope. Magnetic field induced changes in ferro-electric response around 50% with 20% variations were observed on barium titanate (BTO)/ lanthanum strontium manganite (LSMO) structure.

Furthermore, enhancements to magneto-optical Kerr-effect (MOKE) spectroscope enabled study of the origin of magneto-optical enhancement at plasmonic frequencies in magneto-photonic crystals. This paves the way to plasmon-devices with optimal performance for applications in optical communications and sensing. In this line, we developed a unified theoretical frame for modeling of both saturating and non-saturating magneto-optical effects in diluted colloidal dispersions of magnetic nanoparticles. The model shows remarkably good agreement with experimental data obtained from nickel nanoparticles in hexane and toluene using only tabulated data and no fitting. Hence we can envision the use of optimized hybrid metal/ dielectric composites as platforms for new optical devices and especially for innovative plasmon-based sensors exploiting light polarization instead of reflectance.

## RESUMEN

---

En las nuevas aplicaciones basadas en sistemas ferroicos a menudo se consideran las paredes de dominio como portadores de la información. Asimismo, la necesidad de satisfacer la ley de Moore requiere una reducción drástica de las dimensiones de los dispositivos a comercializar. Aunque ya existen métodos para estudiar la dinámica de los dominios a nanoescala, éstos son muy lentos y caros, además es muy complicado medir las propiedades magnéticas y eléctricas simultáneamente. Esto crea la necesidad de un método intermedio que ofrezca resolución lateral submicrométrica y cortos tiempos de medición y que, al mismo tiempo, proporcione suficiente información sobre todas las propiedades ferroicas de un sistema.

Para solucionar este problema, hemos desarrollado varios métodos ópticos que amplían las posibilidades de caracterización multiferroica. Por un lado, hemos desarrollado un montaje experimental magneto-óptico Kerr que permite trabajar bajo campos eléctricos aplicados in-situ en un rango de frecuencias ajustables. Mediante esta aproximación experimental, hemos podido separar y cuantificar diferentes contribuciones al acoplamiento magnetoeléctrico (mediado por tensión superficial y/o por efectos de superficie) y hemos podido analizar su dinámica específica por separado. Por otro lado, hemos podido obtener una cartografía directa del acoplamiento magnetoeléctrico con una resolución lateral submicrónica, mediante el desarrollo de un microscopio confocal sensible a la polarización de la luz. En experimentos realizados en *BTO* / *LSMO* se observaron cambios inducidos por un campo magnético en la respuesta ferroeléctrica en torno al 50 % en promedio, con variaciones de hasta un 20 %.

Finalmente, hemos estudiado el origen del aumento de la respuesta magneto-óptica a frecuencias resonantes con plasmones en cristales magnetofotónicos. Estos resultados abren nuevas perspectivas en dispositivos basados en la física de plasmones, con aplicaciones en comunicaciones ópticas y en detección. En esta línea, hemos desarrollado un marco teórico unificado que permite modelar las señales magneto-ópticas de soluciones coloidales en un rango amplio de frecuencias en el visible. El modelo que proponemos muestra una excelente concordancia con los datos medidos experimentalmente en soluciones coloidales de nanopartículas de níquel en hexano y en tolueno, utilizando solamente las propiedades ópticas tabuladas de los materiales, sin ajustar ningún parámetro. Estos resultados abren nuevas perspectivas en materiales compuestos metal/dieléctrico, para dispositivos innovadores basados en plasmones, que explotan la polarización de la luz en vez de los cambios en reflectancia óptica.

## PUBLICATIONS

---

Some ideas and figures have appeared previously in the following publications:

M. Rubio-Roy, O. Vlašín, O. Pascu, J. M. Caicedo, M. Schmidt, A. R. Goñi, N. G. Tognalli, A. Fainstein, A. Roig, and G. Herranz. Magneto-optical enhancement by plasmon excitations in nanoparticle/metal structures. *Langmuir*, 28(24): 9010–9020, 2012. doi: 10.1021/la301239x. URL <http://pubs.acs.org/doi/abs/10.1021/la301239x>

Imaging Dynamic Magnetoelectric Coupling in Multiferroic Bilayers; Oral presentation, Conference MMM 2013, Denver, Colorado, USA

Dynamic Magnetoelectric Coupling in Co/PZT Bilayers; Oral presentation, Conference MMM 2013, Denver, Colorado, USA

Magneto-optical enhancement by plasmon excitations in nanoparticle/metal structures; Oral presentation, Conference EMRS 2012, Strasbourg, France

Shaping Magneto-Optical Spectra with Plasmonic Resonances, Oral presentation, Conference CEN 2012, Carmona, Spain



## ACKNOWLEDGMENTS

---

All the development of new equipment, internship, conferences and travels were financially supported by Consejo Superior de Investigaciones Científicas (CSIC) [Projects MAT2011 -29269 -CO3, NANO-SELECT CSD2007 -00041] and Generalitat de Catalunya [2009 SGR 00376]. CSIC JAE-predoc grant supported me for most of the time I spent working on this thesis.

Special thanks go to my supervisor Gervasi Herranz, for hundreds of fruitful discussions and huge support during last four years.

Number of high quality samples analyzed here were grown in pulsed laser deposition (PLD) or sputtering chambers at Institut de Ciència de Materials de Barcelona (ICMAB) by Florencio Sánchez, Nico Dix and Diego Gutiérrez. Magnetic nanoparticles were synthesized by Oana Pascu and Mathieu Caillau in the group of Anna Roig, photonic crystals by the group of A. Fainstein in Argentina and by Miguel Rubio, multiferroic bilayers by Salia Cherifi who I'm especially grateful to for an amazing four month internship at Institute of Physics and Chemistry of Materials of Strasbourg (IPCMS) which was also supported by the JCJC ANR program [DYNAMECS 2011 -JS10 -009-01]. Thanks to Marcos Paradinas and Carmen Ocal for the atomic force microscopy (AFM) and piezo force microscopy (PFM) measurements on periodically poled lithium niobate (PPLN) samples. I acknowledge the personnel of the STnano cleanroom facility in Strasbourg for their technical support. The superconducting quantum interference device (SQUID) magnetometer measurements on Co/ PZT sample have been performed at the INAC-NM Laboratory at the CEA-Grenoble by Matthieu Jamet.

I extend gratitude to Josep Fontcuberta who has always had his finger on the pulse of all the research in our group and steered it in the right direction. I thank Jose Caicedo who helped me out a lot especially at the very beginning and to David Pesquera, Miguel Rubio and Matheus Scigaj for collaboration on various projects. I would like to thank Ignasi Fina for development of electronic setup for ferroelectric measurements and his help with implementation of ferroelectric optical imaging and to Blai Cassals for patiently learning all about the current state of my development at ICMAB to continue where I left. I would also like to thank Xavier Marti for fruitful discussions and support and to Josh Malowney, Patrizia Lavicoli, Mathieu Gonidec, Cesar Diez, Elisa Elizondo and all the other wonderful people that made my work in Barcelona a pleasure.

But the biggest thanks go to my great source of inspiration and motivation, woman that I could hardly imagine finishing this work without, my wife Ingrid.





# CONTENTS

---

1	INTRODUCTION	1
2	POLARIZATION OF LIGHT	3
2.1	Polarization . . . . .	3
2.1.1	Linear Polarization . . . . .	3
2.1.2	Circular Polarization . . . . .	4
2.2	Jones Matrix Formalism . . . . .	4
2.3	Magnetic Field Induced Polarization Effects . . . . .	6
2.3.1	Magneto-optical Kerr Effects . . . . .	8
2.3.2	Magneto-refractive effect . . . . .	9
2.4	Polarization of Light and Ferroelectrics . . . . .	10
2.4.1	Ferroelectric Polarization . . . . .	10
2.4.2	Pockels and Kerr Effect . . . . .	10
2.5	Polarization of Light and Strain . . . . .	10
2.5.1	Strain Induced Birefringence . . . . .	10
2.5.2	Magnetostriction . . . . .	11
i	EXPERIMENTAL	13
3	MAGNETO-OPTICAL SPECTROSCOPY	15
3.1	Modes of Operation . . . . .	16
3.1.1	Magnetic Circular Dichroism . . . . .	16
3.1.2	Magnetic Linear Dichroism . . . . .	16
3.1.3	Magnetic Circular Birefringence . . . . .	16
3.1.4	Magnetic Linear Birefringence . . . . .	17
3.1.5	Kerr Effect . . . . .	18
3.2	Data Processing . . . . .	19
4	POLARIZATION SENSITIVE CONFOCAL MICROSCOPY	21
4.1	Confocality . . . . .	21
4.2	Scanning . . . . .	23
4.3	Modes of Operation . . . . .	24
4.4	Domain Imaging . . . . .	26
4.5	Dynamic Measurements . . . . .	28
4.5.1	Pattern Scanning . . . . .	29
4.5.2	Dynamics by decomposition . . . . .	31
4.5.3	Locking-in the Electric and the Magnetic Field . . . . .	32
5	HIGH FREQUENCY MAGNETO-ELECTRIC COUPLING SETUP	33
5.1	Limitations . . . . .	35
5.2	Detection modes . . . . .	36
ii	MAGNETOELECTRIC DOMAIN IMAGING WITH SUB-MICRON LATERAL RESOLUTION	37
6	MAPPING THE OPTICAL BIREFRINGENCE	43
7	VISUALIZATION OF DOMAIN WALLS	47

8	MAPPING FERROELECTRICITY, MAGNETISM AND STRAIN	51
9	MAPPING THE MAGNETOELECTRIC COUPLING STRENGTH	55
9.1	Non-uniform Magnetolectric Coupling Strength . . . . .	56
iii	MAGNETO-ELECTRIC COUPLING DYNAMICS	59
10	HIGH FREQUENCY MAGNETO-ELECTRIC COUPLING	61
11	SEPARATING MAGNETO-ELECTRIC COUPLING EFFECTS	63
12	MAGNETO-ELECTRIC COUPLING STRENGTH IN FREQUENCY SPECTRA	71
iv	MAGNETO-OPTIC SPECTROSCOPY OF MNP-BASED SYSTEMS	75
13	PLASMONIC MAGNETO-PHOTONIC CRYSTALS	77
13.1	Sample Preparation . . . . .	79
13.2	Nanoparticle Synthesis and Characterization . . . . .	80
13.3	Methods . . . . .	81
13.4	Morphology . . . . .	82
13.5	Reflectometry . . . . .	83
13.5.1	<i>Au Void Array</i> . . . . .	83
13.5.2	<i>Au Nanodisk Arrays</i> . . . . .	85
13.6	Magneto-Optical Spectroscopy . . . . .	86
13.6.1	Magneto-Optical Spectra of the Au Void Surface Infiltrated with Nickel Nanoparticles. . . . .	87
13.6.2	Magneto-Optical Spectra of the Au Nanodisk Arrays Infiltrated with Iron Oxide Nanoparticles . . . . .	90
13.7	Origin of Magneto-optical Enhancements . . . . .	94
13.8	Conclusions . . . . .	95
14	FARADAY SPECTROSCOPY OF DILUTED MAGNETIC LIQUIDS	97
14.1	Conclusions . . . . .	108
14.2	Experimental . . . . .	108
14.2.1	Simulation . . . . .	108
14.2.2	Magneto-optic characterization . . . . .	109
14.2.3	Synthesis and characterization of the Ni nanoparticles . . . . .	109
14.2.4	Measurement Precision Factors . . . . .	110
	Conclusions	113
	Further Development	115
	BIBLIOGRAPHY	119

## LIST OF FIGURES

---

Figure 1	Polarization ellipse . . . . .	4
Figure 2	Magnetic effects changing polarization of light . .	7
Figure 3	Magnetic circular dichroism (MCD) and birefringence (MCB) in Faraday geometry . . . . .	8
Figure 4	Magnetic linear dichroism (MLD) and birefringence (MLB) in Voigt geometry . . . . .	9
Figure 5	Configuration of magneto-optical spectrometer in transmission . . . . .	15
Figure 6	Magneto-optic Kerr effect measurement setup, longitudinal configuration . . . . .	17
Figure 7	Main functional unit of PS-CFM . . . . .	22
Figure 8	Topography images of periodically poled lithium niobate (PPLN) and test grating . . . . .	24
Figure 9	Detail of sample mounted in ferroelectric measurements sample holder . . . . .	26
Figure 10	Lock-in operation of PS-CFM for direct magneto-electric coupling measurement. . . . .	27
Figure 11	Comparison of optical and scanning probe microscopy images . . . . .	28
Figure 12	Polarization sensitive confocal microscope principle of operation . . . . .	29
Figure 13	Pattern scanning example . . . . .	30
Figure 14	Field pattern scanning . . . . .	30
Figure 15	Detailed model of the high-frequency magneto-electric coupling setup . . . . .	33
Figure 16	High frequency magneto-electric setup . . . . .	35
Figure 17	Temperature dependence of the magnetization of the LSMO thin film, measured by SQUID . . .	39
Figure 18	Hysteresis loops measured at room temperature for magnetic fields applied along different in-plane directions. . . . .	40
Figure 19	A biaxial magnetic anisotropy is evident from these measurements. Note that at fields above 20 Oe the magnetic anisotropy is suppressed. . .	40
Figure 20	Ferroelectric polarization – electric field loop of the Pt/ BTO/ LSMO sample . . . . .	41
Figure 21	Sketch of the confocal optical arrangement used to map out the birefringence . . . . .	43
Figure 22	Micrograph showing two Pt electrodes on top of the BaTiO <sub>3</sub> / La <sub>2/3</sub> Sr <sub>1/3</sub> MnO <sub>3</sub> bilayer . . . . .	44
Figure 23	Example of quick evaluation of FE response of a sample using field pattern . . . . .	45

Figure 24	Schematics of scanning pattern . . . . .	46
Figure 25	Signal (black) is overlaid with Fourier transforms of the first and second harmonic of the applied electric (blue $e_1$ , $e_2$ ) and magnetic (red $m_1$ , $m_2$ ) fields. For higher contrast, the topography signal was suppressed (white cross in the center). White dots close to the center correspond to the suppression in the filter of the power line frequency. . . . .	47
Figure 26	The diffraction limited measurement spot (red) is inevitably convoluted in the measured shape of domain walls (blue line). Even if actual domain walls have sharp edges the optically measured domain walls will have the curvature determined by diffraction limit. . . . .	48
Figure 27	Because the typical ferroelectric domain size is smaller than the diffraction limit its domain structure cannot be resolved while the bigger magnetic domains are visible . . . . .	49
Figure 28	Mapping out the electro-(magneto-) optic signal and strain from birefringence . . . . .	51
Figure 29	Dynamic magnetoelectric response from optical birefringence maps . . . . .	54
Figure 30	Schematics of magnetoelectric coupling calculation	55
Figure 31	The magnetoelectric coupling strength map . . .	56
Figure 33	Schematic description of the sample layout and experiment geometry . . . . .	61
Figure 32	Schematics of used Co/PZT samples . . . . .	61
Figure 34	Longitudinal Kerr signal measured in 10nm and 7nm thick Co deposited on PZT . . . . .	62
Figure 35	Dynamic PE loops measured at 2 kHz in Co 7nm, Co 10nm and Co onm samples . . . . .	64
Figure 36	As-measured rotation angle variation with the electric field E swept at 3 kHz . . . . .	64
Figure 37	A fit based on the analytical model and the corresponding split into two components . . . . .	65
Figure 38	Even-parity birefringence in Co 10nm, Co 7nm and Co onm samples . . . . .	66
Figure 39	Even-parity birefringence under various magnetic fields at 3 KHz . . . . .	67
Figure 40	Electric field induced optical response of Co 7nm sample at 3 kHz, under magnetic fields . . . . .	68
Figure 41	Magneto-electric factor in strain MEC loop . . . .	69
Figure 42	Magneto-electric factor in surface MEC loop . . .	70
Figure 43	Strain MEC factor as a function of frequency of applied electric field . . . . .	71

Figure 44	Surface MEC factor as a function of frequency of applied electric field . . . . .	72
Figure 45	SEM images of the studied structures . . . . .	77
Figure 46	TEM micrographs of used nanoparticles . . . . .	78
Figure 47	Optical reflectivity spectrometer . . . . .	82
Figure 48	Reflectometry of nanocavities . . . . .	83
Figure 49	Angular optical reflection spectrometry . . . . .	84
Figure 50	Nanodots reflectometry . . . . .	86
Figure 51	Comparison of magneto-optical enhancement on nanodisks . . . . .	88
Figure 52	Magneto-optical enhancement in Fresnel coefficients . . . . .	89
Figure 53	Diagonal and off-diagonal contributions to magneto-optical enhancement . . . . .	91
Figure 54	Magneto-optical spectra of nanodisk arrays . . . . .	92
Figure 55	Fresnell coefficients spectra . . . . .	93
Figure 56	Sketch of the theoretical frame of our MEMT model . . . . .	98
Figure 57	TEM image of the Ni nanoparticles . . . . .	100
Figure 58	Decomposition of Faraday rotation loop . . . . .	101
Figure 59	Schematics of the action of the magnetic colloidal system on the light polarization, whereby rotation and ellipticity are induced by the medium.	102
Figure 60	DLS hydrodynamic size of the colloidal Ni MNPs suspended in hexane . . . . .	103
Figure 61	MEMT model theory and experiment comparison	104
Figure 62	SQUID magnetization versus magnetic field at 298K . . . . .	106
Figure 63	MEMT model, standard model and experiment comparison . . . . .	107
Figure 64	Field cooled-zero field magnetization curves versus temperature . . . . .	110
Figure 65	Basic principle of Yokogawa® disc confocal microscope . . . . .	116
Figure 66	Basic principle of diamond magnetometer . . . . .	117

## ACRONYMS

---

AFM	atomic force microscopy
BTO	barium titanate
CCD	charge-coupled device
CFM	con-focal microscope
CSIC	Consejo Superior de Investigaciones Científicas
DAQ	data acquisition unit
DC	direct current
DLS	dynamic light scattering
HFMEC	high-frequency magneto-electric coupling
ICFO	Institut de Ciències Fotòniques
ICMAB	Institut de Ciència de Materials de Barcelona
ICP-MS	inductively coupled plasma mass spectrometry
IPCMS	Institute of Physics and Chemistry of Materials of Strasbourg
LCP	left circularly polarized light
LSAT	lanthanum strontium aluminum tantalum oxide
LSMO	lanthanum strontium manganite
LSPR	localized surface plasmon resonance
MCB	magnetic circular birefringence
MCD	magnetic circular dichroism
ME	magneto-electric
MEC	magneto-electric coupling
MEMT	modified effective medium theory
MFM	magnetic force microscopy
MGA	Maxwell-Garnett effective medium approximation
MLD	magnetic linear dichroism
MNP	magnetic nanoparticles

MOCFM magneto-optical confocal microscopy  
MOKE magneto-optical Kerr-effect  
NA numerical apperture  
PEM photo-elastic modulator  
PFM piezo force microscopy  
PLD pulsed laser deposition  
PPLN periodically poled lithium niobate  
PSCFM polarization sensitive confocal microscopy  
PZT lead zirconate titanate  
RCP right circularly polarized light  
SAED selected area electron diffraction  
SEM scanning electron microscopy  
SERS surface enhanced Raman spectroscopy  
SNR signal-to-noise ratio  
SQUID superconducting quantum interference device  
STO strontium titanate  
TE transverse-electric  
TEM transmission electron microscopy  
TM transverse-magnetic  
TGG terbium gallium garnet  
YIG yttrium iron garnet

## NOMENCLATURA

---

$\Theta_{h,k}^f$	filtered Fourier space transform
$f$	frequency
$\gamma$	magneto-optic anomaly correction
$\varphi_A$	amplitude of modulation
$\omega$	angular frequency
$N_A$	Avogadro number
$J_N$	Bessel function of the first kind of order N
$\mathbf{E}_{\text{in}}$	complex amplitude vector of incident light
$\mathbf{E}_{\text{out}}$	complex amplitude vector of light after an interaction
$\sigma$	conductivity
$\rho$	density
$m$	electron mass
$E_c$	coercive field
$H$	magnetic field
$w_{h,k}$	Fourier space filter
$\theta_{h,k}^f$	Fourier space filtered image of Kerr rotation
$\nu_b$	frequency of scanning of balanced detector
$\nu_e$	frequency of applied electric field
$\nu_m$	frequency of applied magnetic field
$r_{xy}$	Fresnel coefficient in reflection
$t_{xy}$	Fresnel coefficient in transmission
$\mathbf{I}_\omega$	first harmonic signal
$\mathbf{I}_{2\omega}$	second harmonic signal
$\mathbf{I}_{\text{DC}}$	signal not amplified by lock-in
$\dagger$	Hermitian adjoint
$f_{i,d}(E, c, s, q)$	function modeling hysteresis loop



$\theta_{h,k}$	image of Kerr rotation, h x k pixels
$n$	index of refraction
$\mathbf{I}$	intensity of electric field
$I_X$	intensity of light on detector X
$\Gamma$	modulated part of light transformation
$\Gamma_0$	non-modulated part of light transformation
$\mathbb{M}$	Jones matrix of modulator
$\mathbb{P}$	Jones matrix of polarizer
$\eta_{s,p}$	s- and p- Kerr effect
$\varepsilon$	Kerr ellipticity
$\theta$	Kerr rotation
$\Delta M$	saturated magnetization
$\Delta_{MEC}$	effective magneto-electric coupling
$\alpha_{ME}$	magnetoelectric effect figure of merit
$M$	molar mass
$N_H$	number of horizontal pixels in a recorded image
$N_V$	number of vertical pixels in a recorded image
$\epsilon$	permittivity
$\phi$	phase difference
$\alpha_{pl}$	polarization from plasmonic effects
$\alpha_{sol}$	polarization of solvent
$P_S$	spontaneous polarization
$\varphi_0$	residual birefringence
$\varphi$	retardation - a delay introduced between two components of light after propagation through a device
$c$	speed of light
$P$	vapour pressure
$\mathcal{V}$	Verdet constant
$\nu$	number of particles per unit volume
$\lambda$	wavelength of light



## INTRODUCTION

---

Ferroic systems exhibit physical properties (magnetization or electric polarization) that can be used as a platform to store, manipulate, process and transmit information in the form of magnetic bits or states of electric polarization. Many prospective technologies are based on magneto-electric systems (magnetic and ferro-electric, with cross-coupled ferroic orders) that would allow to go well beyond conventional electronics. On the other hand, the polarization state of light is also relevant to carry information in communications as well as in sensor applications. The use of nanoparticles in these applications has many advantages (versatility, flexibility, easy implementation) but requires a high-sensitivity and large signal-to-noise ratio (SNR). Optical characterization is an ideal tool for characterization of these systems (ferroic materials, magnetoelectric systems, nanoparticle arrays and colloidal dispersions). It provides non-invasive fast characterization, that allows for dynamic measurements.

In the course of this PhD. thesis several optical experimental systems were developed. A cryostat ready magneto-optical confocal microscope for submicronic dynamic imaging of magneto-electric and magnetic domains was developed at [ICMAB](#) in Barcelona and the high frequency magneto-electric coupling setup was developed at [IPCMS](#) in Strasbourg in order to study dynamics of magneto-electric coupling in kHz range. Finally a magneto-optical spectroscopy setup was further developed at [ICMAB](#) to allow for characterization of nanoparticle/plasmonic structures and diluted magnetic liquid dispersions.

New methods of measurement are introduced for quick evaluation of ferroelectricity, ferromagnetism and magneto-electric coupling.



## POLARIZATION OF LIGHT

Many measurement techniques used and developed during this work exploit the polarization of light . This chapter sums up its basic principles.

## 2.1 POLARIZATION

Monochromatic light of frequency  $f$  and angular frequency  $\omega = 2\pi f$  traveling in  $z$  direction with velocity  $c$  has an electric field:

$$\mathbf{E}(z, t) = \Re \left\{ \mathbf{E}_0 \exp \left[ i\omega \left( t - \frac{z}{c} \right) \right] \right\}$$

where  $\mathbf{E}_0$  is its complex amplitude vector and  $t$  is time. It can be split into two components:

$$\begin{aligned} E_x &= E_{x0} \cos \left[ \omega \left( t - \frac{z}{c} \right) + \phi_x \right] \\ E_y &= E_{y0} \cos \left[ \omega \left( t - \frac{z}{c} \right) + \phi_y \right] \end{aligned}$$

where  $\phi = \phi_x - \phi_y$  is the phase difference and  $E_{x0}$ ,  $E_{y0}$  are the magnitudes of each component. The above equations form a parametric expression of an ellipse (figure 1). Denoting the ratio of the magnitudes of the two components of light  $r = \frac{E_{y0}}{E_{x0}}$ , we can write:

$$\tan 2\theta = \frac{2r}{1-r^2} \cos \phi \quad (1)$$

$$\sin 2\varepsilon = \frac{2r}{1+r^2} \sin \phi \quad (2)$$

where  $\theta$  is the rotation and  $\varepsilon$  is the ellipticity of the polarization [1].

## 2.1.1 Linear Polarization

The polarization is linear when the ellipticity is zero. From equation 2 it is clear that this condition is satisfied when the phase difference  $\phi = 0$  or  $\pi$  or when one of the components vanishes ( $E_{x0} = 0$  or  $E_{y0} = 0$ ). The orientation of a linear polarization in reflection is traditionally defined with respect to the plane of incidence (the plane made by the propagation direction and a vector perpendicular to the plane of a reflecting surface). The polarization state of light with the electric field component parallel to this plane is denoted p- (parallel)

and the component perpendicular to this plane is termed s- (from senkrecht, German for perpendicular). P-polarized light is said to be a transverse-magnetic (TM) wave. S-polarized light is also called a transverse-electric (TE) wave.

### 2.1.2 Circular Polarization

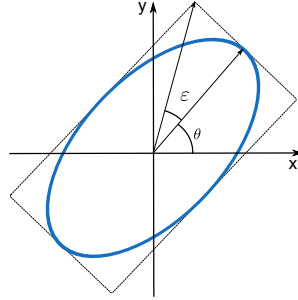


Figure 1: Polarization ellipse

When the phase difference  $\phi = \pm\pi/2$  and  $r = 1$  the polarization is circular. In fact any polarization state can also be thought of as a superposition of left circularly polarized light (LCP) and right circularly polarized light (RCP). In any plane perpendicular to the propagation vector of circularly polarized light, the trajectory of electric field vector is a circle.

## 2.2 JONES MATRIX FORMALISM

If the state of polarization is fully described by its complex amplitude vector

$$\mathbf{E}_0 = \begin{bmatrix} E_{x0} \\ E_{y0} \end{bmatrix}$$

any change of it is fully described by a complex 2x2 matrix:

$$\mathbf{E}_{\text{out}} = \mathbb{J}\mathbf{E}_{\text{in}}$$

where  $\mathbf{E}_{\text{in}}$  is complex amplitude vector of light incident on an optical element and  $\mathbf{E}_{\text{out}}$  is complex amplitude vector of light after an interaction with that optical element described by matrix  $\mathbb{J}$ .

Such matrix fully describes any lossless polarization change and is called Jones matrix. Examples of Jones matrices for some basic optical components are given in the following:

A sample is described by its reflection  $S_R$  and transmission  $S_T$  matrices

$$S_R = \begin{bmatrix} r_{ss} & r_{ps} \\ r_{sp} & r_{pp} \end{bmatrix}$$

$$S_T = \begin{bmatrix} t_{ss} & t_{ps} \\ t_{sp} & t_{pp} \end{bmatrix}$$

where  $r_{xy}$  and  $t_{xy}$  are Fresnel reflection and transmission coefficients respectively.

A polarizer blocks one component of light and transmits the other, its matrix is therefore

$$\mathbb{P} = \begin{bmatrix} 1 & 0 \\ 0 & 0 \end{bmatrix}$$

Polarizer rotated by angle  $a$  is described as

$$\mathbb{A}_a = \mathbb{R}_{-a} \mathbb{P} \mathbb{R}_a = \begin{bmatrix} \cos a \cos a & \cos a \sin a \\ \sin a \cos a & \sin a \sin a \end{bmatrix}$$

where the rotation matrix

$$\mathbb{R}_a = \begin{bmatrix} \cos a & \sin a \\ -\sin a & \cos a \end{bmatrix}$$

Any optical component that induces a retardation (phase shift) between the two components of light is fully described by matrix

$$\mathbb{M} = \begin{bmatrix} 1 & 0 \\ 0 & e^{-i\varphi} \end{bmatrix}$$

where  $\varphi$  is the retardation. In case of a photoelastic modulator (PEM) the retardation is time variable  $\varphi = \varphi_0 + \varphi_A \sin \omega t$ , where  $\varphi_0$  is the residual birefringence and  $\varphi_A$  is the amplitude of modulation. If the phase retarder is a quarter wave plate  $\varphi = \pi/2$ , in the case of a half wave plate  $\varphi = \pi$ .

The calculations with Jones matrices can be further simplified noting that all the optical elements that introduce a phase change  $\varphi$  (modulator, compensator, half-wave plate...) can be expressed in terms of polarizers:

$$\mathbb{R}_{-a} \mathbb{M} \mathbb{R}_a = \mathbb{A}_a + e^{-i\varphi} \mathbb{A}_{a+\pi/2}$$

Because a modulator can be expressed as a sum of modulated and non-modulated part and matrix multiplication distributes over matrix addition ( $A(B+C) = AB+AC$ ) we can write:

$$\mathbf{E}_{\text{out}} = (\Gamma_0 + e^{-i\varphi} \Gamma) \mathbf{E}_{\text{in}} \quad (3)$$

where  $\Gamma_0$  is and  $\Gamma$  is modulated part [2].

The detected signal is not the electric field but its intensity  $\mathbf{I}$ , so we can write

$$\begin{aligned}\mathbf{I} &= \mathbf{E}^\dagger \mathbf{E} = \left(\Gamma_0 + e^{-i\varphi}\Gamma\right)^* \left(\Gamma_0 + e^{-i\varphi}\Gamma\right) \\ &= |\Gamma_0|^2 + |\Gamma|^2 + 2 \cos \varphi \Re \{\Gamma\Gamma_0^*\} + 2 \sin \varphi \Im \{\Gamma\Gamma_0^*\}\end{aligned}\quad (4)$$

where, as always an asterisk denotes complex conjugate and  $\dagger$  the Hermitian adjoint.

If we now assume the residual birefringence of the photo-elastic modulator (PEM) to be zero, its retardation is  $\varphi = \varphi_A \sin \omega t$  and we can expand the sine and cosine using Bessel function of the first kind and  $N$ th order ( $J_N$ ) as

$$\begin{aligned}\sin \varphi &= 2J_1(\varphi_A) \sin \omega t + \dots \\ \cos \varphi &= J_0(\varphi_A) + 2J_2(\varphi_A) \sin 2\omega t + \dots\end{aligned}$$

and rewrite the equation 4 as

$$\begin{aligned}\mathbf{I} &= \mathbf{I}_{\text{DC}} + \mathbf{I}_\omega + \mathbf{I}_{2\omega} \\ \mathbf{I}_{\text{DC}} &= |\Gamma_0|^2 + |\Gamma|^2 + 2J_0(\varphi_A) \Re \{\Gamma\Gamma_0^*\} \\ \mathbf{I}_\omega &= 4J_1(\varphi_A) \Im \{\Gamma\Gamma_0^*\} \\ \mathbf{I}_{2\omega} &= 4J_2(\varphi_A) \Re \{\Gamma\Gamma_0^*\}\end{aligned}\quad (5)$$

$$\mathbf{I}_{2\omega} = 4J_2(\varphi_A) \Re \{\Gamma\Gamma_0^*\} \quad (6)$$

where  $\mathbf{I}_\omega$  is first harmonic signal of PEM,  $\mathbf{I}_{2\omega}$  is signal recovered at the second harmonic of PEM and  $\mathbf{I}_{\text{DC}}$  is the signal not amplified by lock-in. In table 1 of chapter 3 we show how this relates to measured magneto-optical effects.

### 2.3 MAGNETIC FIELD INDUCED POLARIZATION EFFECTS

Any polarized light undergoes various changes when reflected from a surface of a sample or transmitted through it. The amount and type of change depends on the current state of the sample. In order to quantify the changes in the material we simply need to analyze the change of polarization.

There are many different mechanisms of interaction between a magnetic material and polarized light. It is useful to separate them by the relative orientation of the magnetic field and the light propagation vector. If the light propagates parallel to the magnetic field we talk about Faraday geometry. If it is perpendicular to the magnetic field we are dealing with Voight geometry. Changes in the reflected light are due to the magneto-optical Kerr effect.

A schematic overview of these effects is given in figure 2.

A change of polarization occurs when different polarizations are either absorbed differently or propagate through a medium at different speeds. Thus we can sort these effects into four categories:



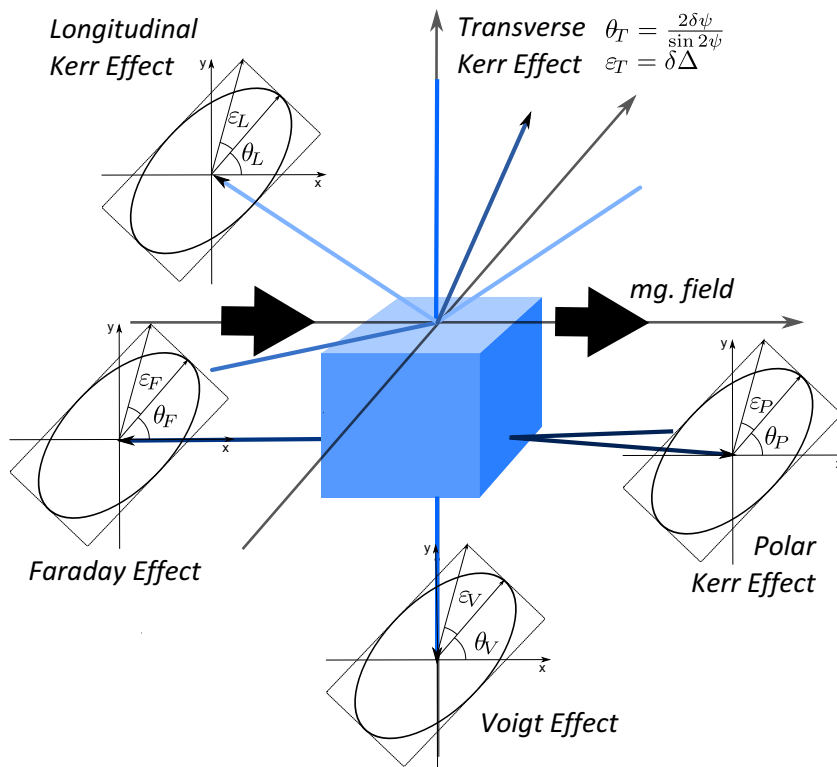


Figure 2: Magnetic effects changing polarization of light.  $\Delta$  and  $\psi$  are elliptic angles.

### MCD - Magnetic Circular Dichroism

When a sample absorbs differently **LCP** and **RCP** light under magnetic field it shows magnetic circular dichroism (**MCD**). This effect usually occurs in Faraday geometry, when light propagates through a sample along the direction of magnetic field.

Monochromatic light linearly polarized at  $45^\circ$  with respect to the axis of the **PEM** set to  $\lambda/4$  retardation is changed periodically to left circular and right circular polarization. If the sample under magnetic field shows **MCD**, there will be difference in amplitude between transmitted circularly polarized light with left rotation (blue line in figure 3) and right rotation (red line in figure 3). This difference causes a change in ellipticity of transmitted light and can therefore be measured as Faraday ellipticity.

### MCB - Magnetic Circular Birefringence

Birefringence is a difference of index of refraction of a material for different polarizations of light. Circular birefringence means that **LCP** and **RCP** light propagate through the material at different speeds. This

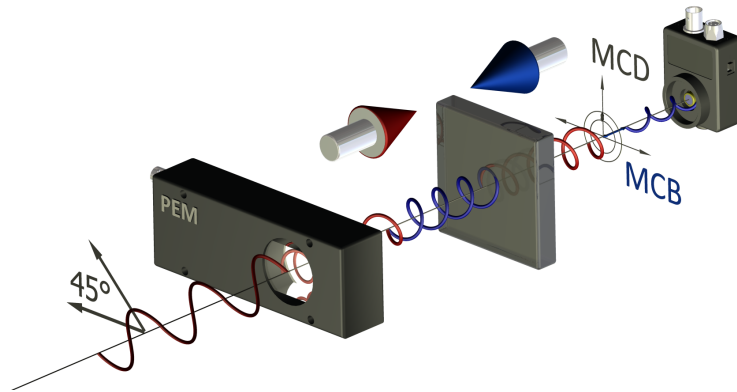


Figure 3: Magnetic circular dichroism (MCD) and birefringence (MCB) in Faraday geometry

difference causes a phase shift between the two components of light (figure 3), which results in rotation of polarization plane. This effect occurs typically with magnetic field along the direction of propagating light and can therefore be measured as Faraday rotation.

#### *MLD - Magnetic Linear Dichroism*

This effect changes the rotation of linearly polarized light propagating through a sample usually perpendicular to the direction of magnetic field. It is caused by different absorption of the two components of linearly polarized light.

Monochromatic light linearly polarized at  $45^\circ$  with respect to the axis of PEM set to  $\lambda/2$  retardation is changed periodically to parallel and perpendicular linear polarization (figure 4). Under magnetic field the ratio of the amplitudes of these two components will change and cause a rotation of polarization plane of the propagating light. This effect usually occurs with magnetic field perpendicular to the direction of propagating light and can be therefore measured as Voigt rotation.

#### *MLB - Magnetic Linear Birefringence*

Linear birefringence means that the two components of linearly polarized light propagate through the material at different speeds. This difference causes a phase shift between the two components of light which results in ellipticity of the transmitted light (figure 4). It's therefore measured as Voigt ellipticity.

##### *2.3.1 Magneto-optical Kerr Effects*

Any polarization change induced directly by magnetic field in reflected light is referred to as magneto-optical Kerr effect. We recog-

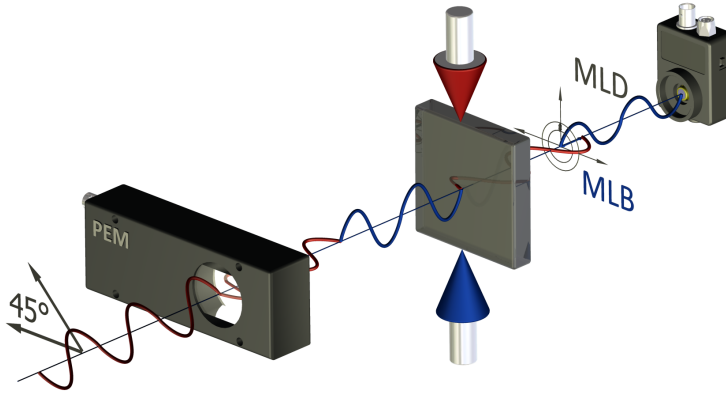


Figure 4: Magnetic linear dichroism (MLD) and birefringence (MLB) in Voigt geometry

nize three different magneto-optical Kerr effects based on the relative direction of magnetic field and plane of incidence (figure 2).

#### *Longitudinal Magneto-optical Kerr effect*

Magnetic field is in plane of incidence and in sample plane. Comes from longitudinal component of magnetization vector.

#### *Polar Magneto-optical Kerr effect*

Magnetic field is in the plane of incidence and normal to the sample plane. Originates in out-of-plane component of magnetization vector.

#### *Transverse Magneto-optical Kerr effect*

Magnetic field is normal to the plane of incidence and in sample plane. Comes from component of magnetization vector perpendicular to the external magnetic field.

#### 2.3.2 *Magneto-refractive effect*

Realignment of magnetization changes conductivity which causes change in refractive index which in turn changes polarization. It's been demonstrated for the first time in [3]. Because permittivity is

$$\epsilon = 1 + i \frac{4\pi\sigma}{\omega}$$

it is clear that changes of conductivity  $\sigma$  are changes of permittivity. Magneto-refractive effect linked to magnetopolaron conduction in magnetic transition metal oxides has been studied in depth in the thesis of J.M. Caicedo Roque and references therein [4].

## 2.4 POLARIZATION OF LIGHT AND FERROELECTRICS

### 2.4.1 *Ferroelectric Polarization*

Each ferroelectric material has its spontaneous polarization that can be changed by application of electric field. There is a minimal voltage needed to switch orientation of ferroelectric polarization. Once this value is reached, the material will keep some of this polarization even after the electric field is switched off. Ferroelectric polarization will therefore produce typical saturating hysteresis loop with electric field.

### 2.4.2 *Pockels and Kerr Effect*

The index of refraction is generally a function of applied electric field  $n(E)$ . The function can be approximated as:

$$n(E) = n + a_p E + a_K E^2$$

where  $a_p$  and  $a_K$  are coefficients proportional to Pockels and Kerr effect. Signal linear with electric field comes from Pockels effect, signal quadratic with electric field is called Kerr effect. These electrooptic effects appear only in non-centrosymmetric systems like ferroelectrics and can be used for their characterization.

It can't be neglected that both Pockels and Kerr effect differ with direction of applied field with respect to the crystal structure [5]. For each crystallographic group an electro-optic  $6 \times 3$  matrix  $r_{ij}$  can be derived with several dependent or independent coefficients.

$$\Delta B = r_{ij} E_k$$

where  $\Delta B$  are field induced changes and  $E_k$  is applied electric field vector [6].

## 2.5 POLARIZATION OF LIGHT AND STRAIN

Both electric and magnetic fields applied to a sample can induce strain. Strain then induces changes in the lattice of a material which can cause change of index of refraction or induce birefringence for example. Interaction of the material with polarized light is therefore altered as a secondary effect.

### 2.5.1 *Strain Induced Birefringence*

All ferroelectrics are piezoelectrics, so there is always an electric field induced strain present that is detectable in reflected polarization through the birefringence it causes. In case of highly piezoelectric materials

like [PZT](#), this effect can be much stronger than ferroelectric polarization. Strain induced effects are not dependent on the direction of electric field, just its amplitude, they are even with field.

### 2.5.2 *Magnetostriction*

Magnetostriction is a change of shape or dimensions during magnetization. The magnetization changed due to the applied magnetic field, changes the magnetostrictive strain until reaching its saturation value. This effect was discovered in 1842 by James Joule [7]. Its inverse Villari effect was observed for the first time 25 years later [8].



## Part I

### EXPERIMENTAL

In the course of this work several experimental systems were developed. This part gives a thorough description of both their functionality and limitations. The first chapter is dedicated to an introduction of the basic principles needed for the understanding of later concepts. A home-built magneto-optical spectroscope is described, that was further developed during this work. Then the cryostat-ready polarization-sensitive confocal microscope developed as a main part of this thesis is presented. And finally a novel system designed for high-frequency magneto-electric coupling measurements is introduced. This part only deals with experimental aspect; the data treatment and applications are explained later.





## MAGNETO-OPTICAL SPECTROSCOPY

One of the basic tools for the characterization of magnetic materials is magneto-optical spectroscopy. Such a system was previously developed at ICMAB (figure 5) [4]. Only minor changes were introduced to this setup during this work. Further automatization, allowing for unassisted measurements of entire spectra and a multistep data processing procedure developed is described at the end of this chapter.

Both of these improvements have the same goal, improving signal recovery. Fully automated measurement means that the measurement can be done in a dark room reducing light background and temperature fluctuations to minimum. Data processing separates the signal from unwanted contributions as a temperature drift or a quadratic signal.

The spectroscope uses a 150 W Xe arc lamp (ZolixTechnology) and monochromator (Zolix I-150) that allows it to cover the entire visible spectrum. It is combined with cryostat for continuous temperature measurements from room temperature to 8K.

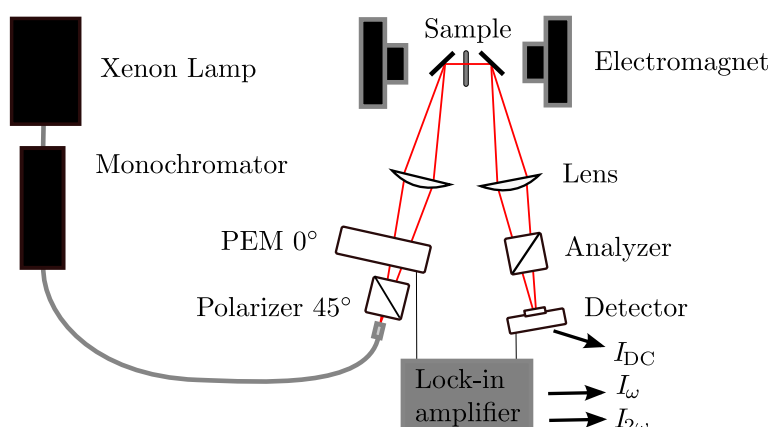


Figure 5: Configuration of magneto-optical spectrometer in transmission

Polarization changes of light after reflection are typically quite small and signal can quickly become weaker than the noise. Most effective way to detect a signal that is much weaker than the noise is by means of lock-in amplification. Lock-in amplifier is a device that can extract a signal with known carrier wave from a very noisy background. Such carrier wave is established by modulation.

Most straightforward way of light modulation is the modulation of intensity by periodic interruption. These intensity modulators are called choppers. For our purpose, however, it is more advantageous to modulate the polarization of light instead, using a PEM. Typical PEM has variable retardation and modulates the light at frequency of

50kHz. Its principle is very simple. A birefringent medium is placed between a pair (or two) of piezo actuators that induce variable stress on it. This stress changes the birefringence of the medium causing a speed difference between the two polarization components. This speed difference is conveniently expressed as a portion of the wavelength of the propagating light by which one polarization is delayed from the other and is referred to as retardation. If one of the polarizations is delayed by one quarter of the wavelength with respect to the other after passing through an optical element, we call this element a quarter wave plate. Half wave plate causes half wavelength retardation.

### 3.1 MODES OF OPERATION

#### 3.1.1 *Magnetic Circular Dichroism*

Circular dichroism is a difference in absorption of left and right circularly polarized light and it is typically very small comparing to absolute values so it can be practically recorded only using modulation. To generate modulated left and right circularly polarized light we set the PEM to a quarter wave retardation. The signal locked-in at the frequency of modulation (first harmonic signal) is then proportional to the difference between signal from left circular polarization and signal from right circular polarization (figure 3 in chapter 2). This signal normalized by the intensity of direct current (DC) signal (signal before lock-in amplification) is directly proportional to MCD.

$$\text{MCD} \propto I_{\omega}/I_{DC}$$

#### 3.1.2 *Magnetic Linear Dichroism*

If we set the PEM to half-wave retardation instead, the polarization of light will be changing from parallel to perpendicular to the plane of the PEM at double of its frequency, because minus half-wave retardation is equal to plus half-wave retardation. Signal locked-in at second harmonic of PEM will therefore be proportional to the difference in intensity between the two perpendicular linear polarizations of the transmitted light (figure 4 in chapter 2). After normalization by DC signal we obtain magnetic linear dichroism (MLD) signal.

$$\text{MLD} \propto I_{2\omega}/I_{DC}$$

#### 3.1.3 *Magnetic Circular Birefringence*

Circular birefringence causes a delay between two opposite circular polarizations. If we think of linear polarization as a composition of two in-phase circular polarizations, the rotation of polarization plane

becomes a phase-shift. So clearly a material showing magnetic circular birefringence will rotate polarization plane of linearly polarized light.

To measure magnetic circular birefringence (MCB) we set PEM again to half-wave retardation. To detect rotation of polarization plane we must introduce an analyzer (polarizer that will only let one of the components of the signal onto the detector). This signal amplified at second harmonic frequency of the PEM normalized by DC signal is than proportional to MCB.

$$\text{MCB} \propto I_{2\omega}/I_{DC}$$

### 3.1.4 Magnetic Linear Birefringence

Linear birefringence causes a phase difference between two perpendicular polarizations of propagating light therefore causing a non-zero ellipticity. Putting PEM and sample at an angle of  $45^\circ$  between a pair of crossed polarizers and using arbitrary retardation of the PEM, it can be shown [9] that

$$\text{MLB} = \sin^{-1} \left( \frac{1 - J_0(\varphi_A)}{J_1(\varphi_A)} \frac{I_\omega}{I_{DC}} \right)$$

where  $J_N$  is Bessel function of the first kind and order N,  $I_\omega$  is first harmonic signal and  $I_{DC}$  is non-amplified signal.

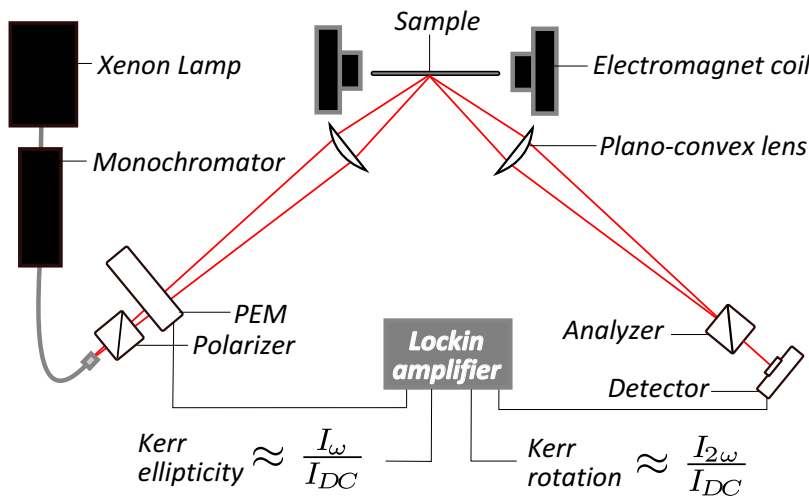


Figure 6: Magneto-optic Kerr effect measurement setup, longitudinal configuration

A general configuration of all magneto-optical transmission spectrometry measurements is in figure 5. Specific configuration for each measurement is in table 1 where N/A means the analyzer is removed for the corresponding type of measurement and nulling means that the analyzer is rotated prior to the measurement until the corresponding harmonic signal is zero.

effect	PEM retardation	analyzer angle	signal
MCD	$\lambda/4$	N/A	$\frac{I_\omega}{I_{DC}}$
MLD	$\lambda/2$	N/A	$\frac{I_{2\omega}}{I_{DC}}$
MCB	$\lambda/2$	$0^\circ$	$\frac{I_{2\omega}}{I_{DC}}$
MLB	$\varphi_A$	$-45^\circ$	$\sin^{-1}\left(\frac{1-J_0(\varphi_A)}{J_1(\varphi_A)}\frac{I_\omega}{I_{DC}}\right)$
$\theta_F$	$0.383\lambda$	nulling	$1.158\frac{I_{2\omega}}{I_{DC}}$
$\varepsilon_F$	$0.383\lambda$	nulling	$0.963\frac{I_\omega}{I_{DC}}$

Table 1: Configuration of magneto-optical spectroscopy in transmission for different types of measurements

### 3.1.5 Kerr Effect

As well as transmission measurements the setup can be used for measurements in reflection. All three conventional configurations are available, for measurement of longitudinal, polar and transverse Kerr effect allowing to obtain all three elements of magnetization vector.

The measurement configuration for magneto-optical Kerr effect is sketched in figure 6. Using equation 4 we can write the corresponding Jones matrix equation as:

$$\begin{aligned}
\mathbf{E}_{\text{out}} &= \mathbb{P}\mathbb{R}_a\mathbb{S}_R\mathbb{R}_{-m}\mathbb{M}_\varphi\mathbb{R}_m\mathbb{R}_{-p}\mathbb{P}\mathbf{E}_{\text{in}} \\
&= \mathbb{P}\mathbb{R}_a\mathbb{S}\left(\mathbb{A}_m + e^{-i\varphi}\mathbb{A}_{m+\pi/2}\right)\mathbb{R}_{-p}\mathbb{P}\mathbf{E}_{\text{in}} \\
&= (\Gamma_0 + e^{-i\varphi}\Gamma)\mathbf{E}_{\text{in}}
\end{aligned} \tag{7}$$

where  $\Gamma_0 = \mathbb{P}\mathbb{R}_a\mathbb{S}\mathbb{A}_m\mathbb{R}_{-p}\mathbb{P}$  and  $\Gamma = \mathbb{P}\mathbb{R}_a\mathbb{S}\mathbb{A}_{m+\pi/2}\mathbb{R}_{-p}\mathbb{P}$ ,  $a, m, p$  are the angles of analyzer, modulator and polarizer with respect to the plane of incidence, the  $\mathbb{M}_\varphi$  is modulator with retardation  $\varphi$ ,  $\mathbb{A}_m$  is a matrix of a polarizer rotated at an angle  $m$  and  $\mathbb{S}_R$  is reflection matrix of a sample.

The modulation is most efficient when the polarizer is at  $45^\circ$  with respect to the optical axis of the modulator. For simplification of the calculation it is also advantageous to put the optical axis of the modulator in the plane of incidence ( $m = 0^\circ$ ). Thus putting  $p = 45^\circ$  and  $m = 0^\circ$  in the equation 7 we immediately get

$$\mathbf{E}_{\text{out}} = \left[ (r_{ss} \cos a + r_{sp} \sin a) + e^{-i\varphi}(r_{ps} \cos a + r_{pp} \sin a) \right] \mathbf{E}_{\text{in}} \tag{8}$$

Kerr effect  $\eta$  is magnetic field induced change of one polarization state to the other. In terms of the complex sample-matrix elements it is either

$$\eta_s = \theta_s + i\varepsilon_s = r_{sp}/r_{ss} \tag{9}$$

or

$$\eta_p = \theta_p + i\varepsilon_p = r_{ps}/r_{pp} \tag{10}$$

based on which polarization component we take as reference. In equations 4, 5 and 6 we show that the problem can be simplified to solving element  $\Gamma_0^*$ . Combining equations 7 to 10 we can write

$$\Gamma_0^* = \rho |r_{ss}|^2 [\eta_p \cos^2 a + \cos a \sin a + \eta_s^* \sin^2 a] \quad (11)$$

where  $\rho = r_{pp}/r_{ss}$ .

Real and imaginary parts of  $\Gamma_0^*$  are directly proportional to first and second harmonic as shown in eq. 5 and 6. From equation 11 it is clear that by adjusting the analyzer we change ratio of  $\eta_s$  and  $\eta_p$ .

Specifically, for  $a = 0$  rad the equations 5 and 6 collapse to

$$\begin{aligned} \frac{I_{2\omega}}{I_{DC}} &= \frac{2J_2(\varphi_A)}{1 + J_0(\varphi_A)\theta_p} \theta_p \\ \frac{I_\omega}{I_{DC}} &= \frac{2J_1(\varphi_A)}{1 + J_0(\varphi_A)\theta_p} \varepsilon_p \end{aligned} \quad (12)$$

and for  $a = \pi/2$  rad we have

$$\begin{aligned} \frac{I_{2\omega}}{I_{DC}} &= \frac{2J_2(\varphi_A)}{1 + J_0(\varphi_A)\theta_s} \theta_s \\ \frac{I_\omega}{I_{DC}} &= \frac{-2J_1(\varphi_A)}{1 + J_0(\varphi_A)\theta_s} \varepsilon_s \end{aligned} \quad (13)$$

The ratio of the first harmonic signal and the DC signal is proportional to the Kerr ellipticity while ratio of the second harmonic signal and the DC signal is proportional to the Kerr rotation. Since retardation of the modulator  $\varphi_A$  is adjustable we can set  $J_0(\varphi_A) = 0$  when we put  $\varphi_A = 2.405$  rad in equations 12 and 13 and we can write

$$\theta_p = 1.158 \frac{I_{2\omega}}{I_{DC}} \quad (14)$$

$$\varepsilon_p = 0.963 \frac{I_\omega}{I_{DC}} \quad (15)$$

### 3.2 DATA PROCESSING

In magneto-optics the desired information is often carried by a mere few  $\mu\text{rad}$  of polarization contrast. Polarization changes on similar scale can unfortunately be caused by several other factors. The most inconvenient is probably the temperature drift which causes very slow changes in the polarization. It can be disentangled from the magnetic-field induced signal by averaging over multiple loops. This, however, becomes very inconvenient with materials that saturate at high magnetic fields. Time per loop increases significantly with growing amplitude magnetic field, while taking one magneto-optical spectra typically requires sequential measurement of around hundred different wavelengths. With usual three to five loops per wavelength, the

averaged loop is often deformed by temperature drift and drift corrections are needed. I applied two methods of drift correction, a high pass digital filter and drift function fitting. High pass digital filter suppresses all the frequencies that are much lower than the frequency of applied field. This method requires certain level of SNR and often fails when we get closer to the sensitivity limit and when the total temperature drift over the measurement time is bigger than amplitude of the ferromagnetic hysteresis loop. This is fortunately a requirement for successful drift elimination by fitting. The two methods thus complement each other.

Next step is averaging of drift corrected loops. For that we need to separate the two branches of hysteresis loop. If we take the current through the coil as a reference, the loops will be distorted as the actual field on the sample will be phase shifted from the current. Taking only signal from the magnetic field probe (Hall probe) is also limited by its range. Furthermore, the actual maximum magnetic field changes as the coil heats up. It's therefore convenient to take as a reference the combination of the two, the phase and the amplitude from the Hall probe and the value at each measurement point from the current.

The last important step is 2D filtering when all the loops of a spectra are plotted in magnetic field vs. wavelength coordinates. Using a rectangular filter very efficiently reduces the noise and eliminates random errors. However, if the used light source has a sharp spectral lines as in our case, they can appear in the processed data as a parasitic signal.

## POLARIZATION SENSITIVE CONFOCAL MICROSCOPY

---

The ultimate goal here is a simultaneous dynamic imaging of ferroelectric and magnetic domains and direct imaging of magnetoelectric domains. Because domains are simply regions with different polarization state, they induce different changes in interacting light. These changes are very small (typically below mrad) so it is critical to keep noise as low as possible in order to detect them. Confocal microscopy is very well suited for this purpose.

The polarization sensitive confocal microscope developed in the course of this doctoral work was adapted from the Attocube CFMI<sup>®</sup> cryostat ready confocal microscope. Although the cryostat operation of the microscope was not part of this thesis, all the extensions were kept fully cryostat compatible.

Attocube CFMI<sup>®</sup> was designed to be used with an optical fiber feed and fiber based detector. But because the leakage of optical fibers is well known to be dependent on mechanical stress and temperature drift, the intensity of light through the fiber varies slightly over time. This is then a parasitic signal in topography measurement. This intensity variation is not homogenous and so it makes it very problematic to maintain a polarization state of light while fiber guiding it to the detector even at short distances.

While this problem is negligible in standard microscopy, where intensity of light is measured, it is not acceptable when polarization state is the signal. The fiber feed has therefore been replaced with bench-top laser and fiber detector was replaced with free space detector.

The setup was also adjusted for simultaneous use of two lasers and two detectors which allows for simultaneous detection of topography (using randomly polarized laser) and polarization change (using polarized light) (figure 7).

The cryostat insert of the microscope is placed between the poles of a room temperature electromagnet capable of generating magnetic field up to around 1T.

For ferro-electric measurements a sample holder facilitating wire-bonding of structures on the sample has been added.

### 4.1 CONFOCALITY

The confocality gives the microscope its name. It is a simple principle of letting only in-focus light to reach the sample and then letting

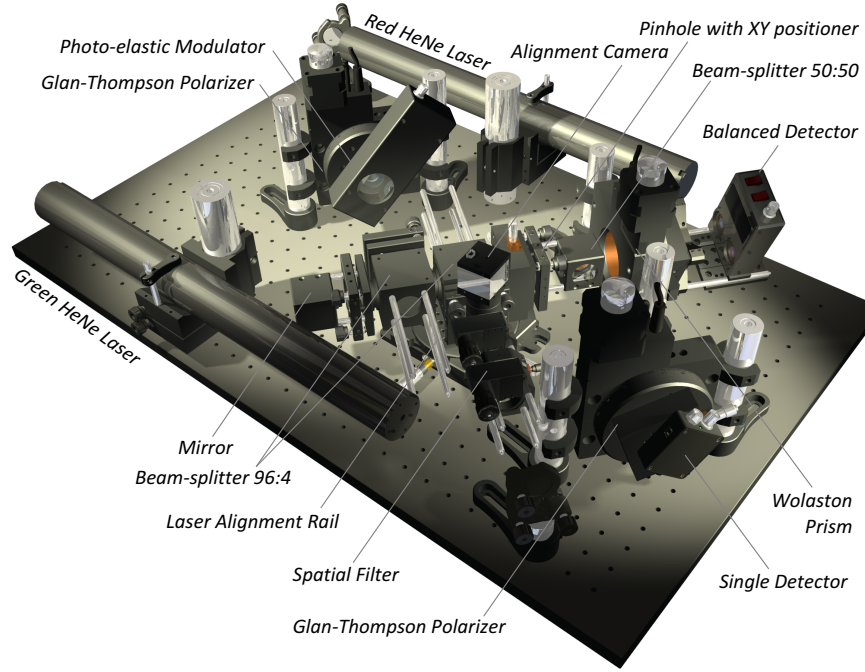


Figure 7: Main functional unit of PS-CFM

only in-focus reflected light to reach the detector (see figure 12b on page 29). Doing this, the fundamental limit of optical resolution can be reached.

There is of course a more precise mathematical description: A laser with cylindrical symmetry can be described by a combination of a Gaussian beam profile with a Laguerre polynomial. Each transverse mode of the laser beam (particular electromagnetic field pattern of radiation measured in a plane perpendicular (i.e., transverse) to the propagation direction of the beam) is denoted  $TEM_{pl}$ , where  $p$  and  $l$  are integers labeling the radial and angular mode orders, respectively. The intensity at a point  $r, \varphi$  (in polar coordinates) from the center of the mode is given by:

$$I_{pl}(\varrho, \varphi) = I_0 \varrho^l \left[ L_p^l(\varrho) \right]^2 \cos^2(l\varphi) e^{-\varrho} \quad (16)$$

where  $\varrho = 2r^2/w^2$ , and  $L_p^l$  is the associated Laguerre polynomial of order  $p$  and index  $l$  and  $w$  is the spot size of the mode corresponding to the Gaussian beam radius.

The only beam mode we want to allow to reach the sample is  $TEM_{00}$ . Some lasers are already adjusted to emit this mode only and so is ours. With other lasers, we can filter the desired mode passing the light through a pinhole.

The beam is then steered to a high numerical aperture objective lens by reflection from a beam splitter. Because the light will have to pass through the same beam splitter after reflection an asymmetric 96:4 beam-splitter ratio is chosen (96% transmitted, 4% reflected). Only



4% of laser light reaches sample, but 96% percent of light carrying information reaches the detector. The power of the laser is chosen accordingly  $25\times$  higher than desired power on the sample. We chose this power to be 30mW considering the light is being concentrated to a very small spot on the sample ( $\sim 5\mu m$ ). This is comparable to using 100mW laser with standard magneto-optical Kerr effect measurements where focal spot is around  $50\mu m$  wide.

Upon reflection from the sample, which is positioned in focal plane of the objective lens, the beam is passed through another pinhole filtering out all out-of-focus light and to a detector.

Using this simple principle the maximum optical resolution can be reached right at the diffraction limit  $0.44\lambda/NA$  [10], where NA is the numerical apperture of the objective lens and  $\lambda$  is the wavelength of light. In our case, using red He-Ne laser (632.8nm) and lens with numerical apperture (NA) = 0.68, the theoretical limit we can reach is resolution of 409nm. In the case of green He-Ne laser (543nm) the limit is 351 nm.

For polarization sensitive measurements the main advantage of confocal microscopy is the noise suppression. In certain situations we can also take advantage of axial resolution ( $1.5\lambda/NA$ ) for measurements on interfaces inside the sample. Lower resolution in comparison to scanning probe techniques is justifiable tradeoff for ability of simultaneous ferroelectric and magnetic imaging.

## 4.2 SCANNING

There are two general ways of scanning the beam across the sample. Moving the sample or moving the beam. Moving the light beam is much faster. The direction of the beam is changed rapidly using the same principle as an electron tube TV. This method however does not maintain constant focal distance and beam is not always passing through the center of the objective lens. While this is acceptable in standard microscopy, it is not so when we are interested in polarization. The light passing through the lens at different angles would experience different polarization and the signal that is usually at the order of 1mrad would be lost.

When moving the sample, the beam is static while we scan the sample in the focal plane of the objective lens by means of two piezo actuators. This way the light beam can be aligned to pass precisely through the center of the objective lens minimizing the polarization by the lens.

The maximum range of scanning is  $40\times 40\mu m$ . The maximum speed before distortions is about 1mm/s which corresponds to taking 1000 x 1000 samples at the rate of  $100\mu s$  per sample from region of  $40\times 40\mu m$ . Image like this will take exactly 200 seconds, because there are two

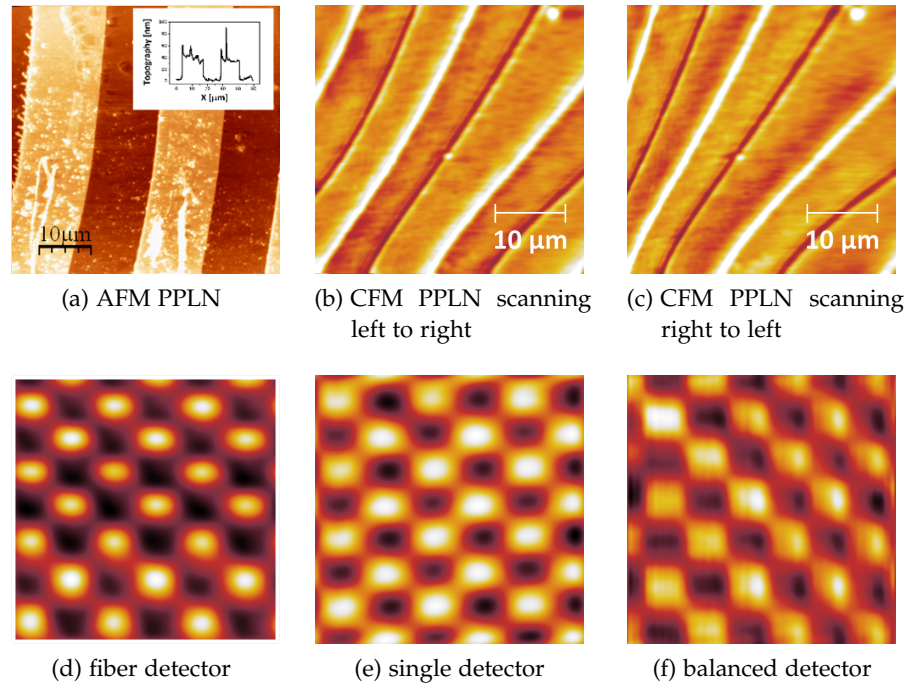


Figure 8: Topography images of periodically poled lithium niobate (PPLN) and test grating

images taken simultaneously one in forward (left to right) direction the other backward (right to left).

The modularity of our specific confocal microscopes allows for an eventual combination of con-focal microscope (CFM) with AFM which is why the precision of the piezo actuators is below 1nm.

#### 4.3 MODES OF OPERATION

The aim here is to extract as much information as possible from reflected light. Besides the changes in intensity of non-polarized light (topography) we want to analyze changes in linear and circular polarization.

##### *Topography*

It remains important to detect the topography of the sample as many elements on the surface of a sample can polarize or depolarize light. It is essential to separate the topography-induced polarization from polarization induced by the intrinsic effects of the material which are of our main interest. For the measurement of the sample topography, both polarizers are removed from the optical path (figure 7).

CFM topography images can be compared to AFM images for example on periodically poled lithium niobate prepared by the team of

Valerio Pruneri at Institut de Ciències Fotòniques (ICFO), Barcelona (figure 8a). Here the height difference between alternating stripes on the sample is 30 nm (inset in figure 8a).

Images 8b and 8c are taken at the same time with opposite direction of scanning. Taking images in both directions is important for elimination of scanning direction artefacts. As you can see by comparing the two images, some of the dark regions on the stripes are indeed artefacts of scanning direction. Different contrast on opposite edges on the other hand does not change with direction and is likely caused by a tilt of the sample.

Figures 8d , 8e and 8f are CFM images of test grating (silicon dots separated by  $2\mu m$ ) taken with various detectors. You can see slight variations of intensity on the image 8d caused by the aforementioned leakage in the optical fiber. Image taken with randomly polarized laser and single free-space detector without polarizers is in figure 8e. Figure 8f taken with balanced detector is included to demonstrate that topography also changes polarization. It is therefore crucial to efficiently disentangle the polarization changes caused by topography from polarization coming from intrinsic properties of the material.

### *Linear Polarization*

One of the simplest ways of detecting changes in the linear polarization state of light is splitting the reflected light into two perpendicular polarizations by means of Wollaston prism (figure 12a). The intensity of each perpendicular polarization is then measured by one of two identical balanced detectors. The rotation of polarization plane  $\theta$  can be then expressed as:

$$\theta = \frac{I_A - I_B}{2(I_A + I_B)}$$

where  $I_A$  is intensity at detector A and  $I_B$  is intensity on detector B. Before the measurement, the Wollaston prism and balanced detector assembly is rotated so that there is the same signal detected on both detectors. Only at this position equal changes of polarization plane in each direction will give zero differential signal on the balanced detector.

The frequency of scanning with this method is limited only by the refresh rate of the detector (1MHz in our case - Newport large area balanced photoreceiver, model: 2307). The scanning rate is important here, because while few minutes per loop is acceptable with magneto-optical spectroscopy in one point, when scanning millions of points with confocal microscope the time per loop has to be kept as short as possible. Not only for convenience, but also to minimize influence of temperature and piezo drift.

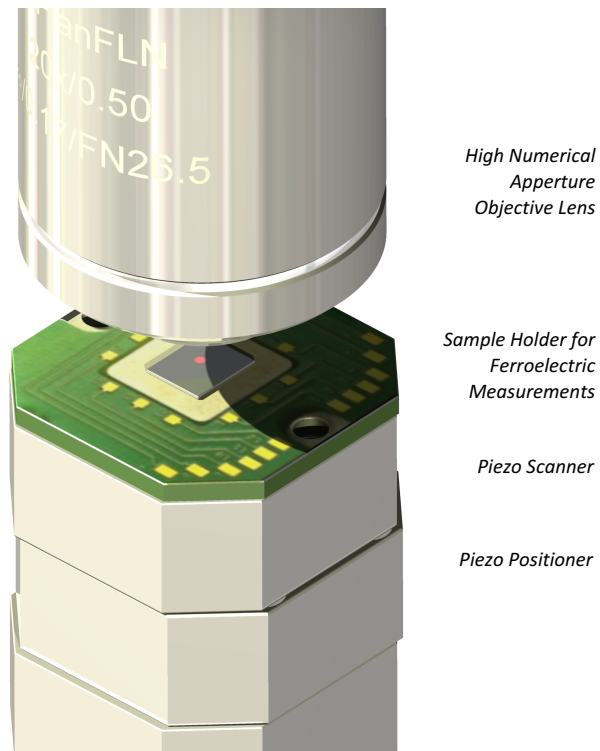


Figure 9: Detail of sample mounted in ferroelectric measurements sample holder

### *Circular Polarization*

For this mode of operation a PEM is used to generate modulated circularly polarized light. Signal is then recovered at the first or second harmonic frequency of the PEM using a lock-in amplifier to obtain Kerr rotation and Kerr ellipticity (eq. 14 and 15 on page 19). This type of measurement is limited by the frequency of PEM (50kHz).

#### 4.4 DOMAIN IMAGING

The main motivation for building this microscope was to study ferroelectric and ferromagnetic domain structure.

The great advantage of using a visible light for probing is no possible damage to the sample and no unwanted interaction of the sample and a probe. Scanning probe techniques have definitely better lateral resolution, but lot of limitations that come with it. Magnetic force microscopy would often switch orientation of magnetization vector while scanning it, piezo-force microscopy is only useful for materials that show strong enough piezo effect.

No such limitations exist in confocal microscopy.

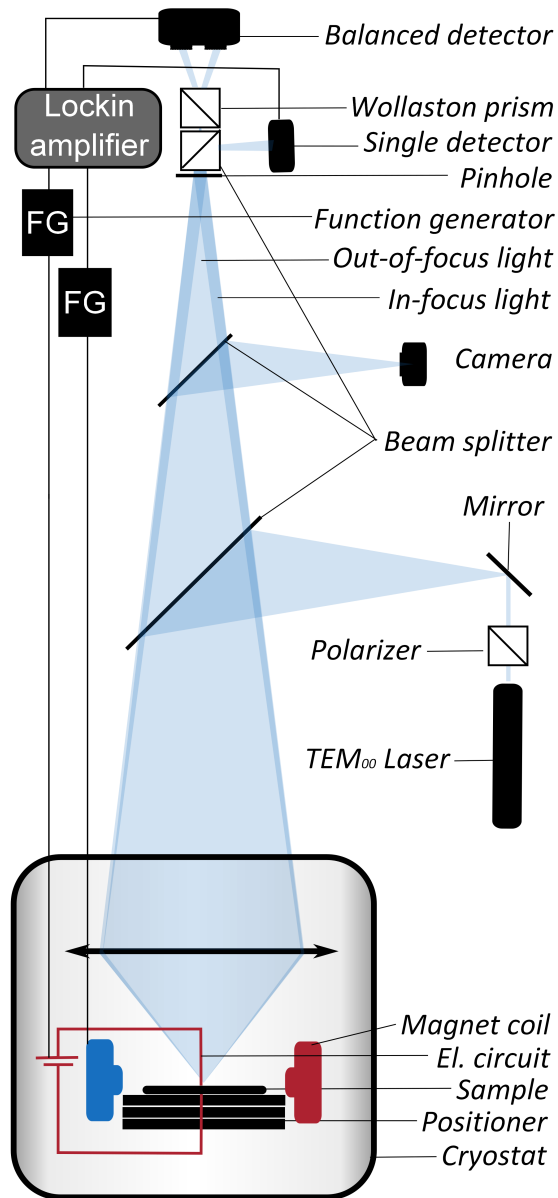


Figure 10: Lock-in operation of PS-CFM for direct magneto-electric coupling measurement.

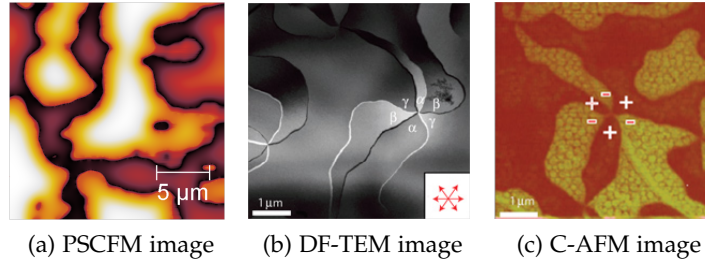


Figure 11: Comparison of optical images of Lutetium Manganite ( $\text{LuMnO}_3$ ) and scanning probe microscopy images (dark-field TEM and conductive AFM) of Yttrium Manganite ( $\text{YMnO}_3$ ) that have a very similar structure. Dark field TEM and conductive AFM images were adapted from Choi et al. [11].

### *Ferromagnetic Domain Imaging*

Ferromagnetic materials interact with polarization of light differently based on the direction of magnetization vector, the magnetic domain orientation. The change in signal induced by applied magnetic field can be therefore attributed to change of magnetization vector orientation. But Kerr effect in magnetic materials is not the only effect that can change polarization state of reflected light (see chapter 2 on page 3).

### *Ferroelectric Domain Imaging*

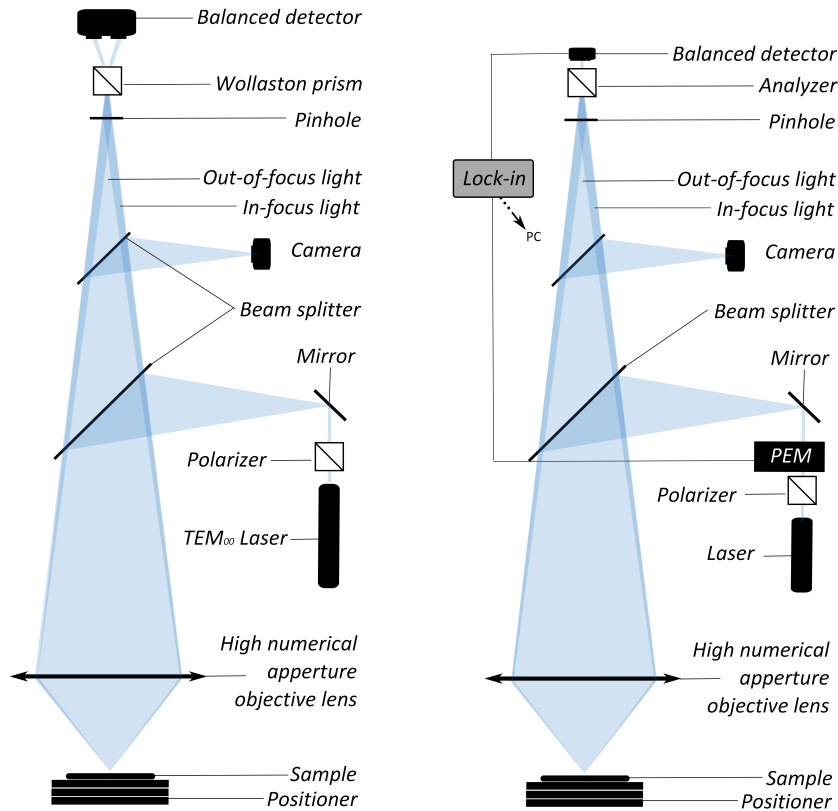
Ferroelectric polarization on the surface interacts with polarization of incident light. The polarization can be spontaneous or induced by applied electric field. To apply electric field an Attocube manufactured sample holder for ferroelectric measurements is used (figure 9). Twelve separate electrodes are disponible, so twelve structures can be connected on the sample at the time.

Domain structures can be visualized either in relaxed or in dynamic state. However, the diffraction limit of the confocal microscope is in many materials bigger than the typical ferroelectric domain. We demonstrated the ferroelectric domain imaging on  $\text{LuMnO}_3$  (Figure 11 )

## 4.5 DYNAMIC MEASUREMENTS

It is useful to see how the ferroic states on the surface evolve with time. This is the purpose of dynamic measurements.

Many times it has been shown that both types of domains nucleate in the same region every time, while the nucleation center is usually at a structural discontinuity. Therefore we can obtain dynamic images of large areas of the surface by recording a hysteresis loop in



(a) PSCFM with balanced detector and Wollaston prism (b) PSCFM with PEM and Lock-in amplifier

Figure 12: Polarization sensitive confocal microscope principle of operation

every point. This approach is however quite time consuming or requires very high speed detector. To overcome this problem a different measurement method was needed.

#### 4.5.1 Pattern Scanning

The polarization sensitive microscope is obviously intended to be a fast and easy method, a device that could quickly decide a suitability of a given sample for further analysis. The perfect output would be a single image taken in matter of minutes that would give us a quantitative information about ferroelectricity, ferromagnetism, magneto-electric coupling and topography in each point of a large area on the sample. To reach this goal a novel method of measurement is proposed here.

For this type of measurement frequency of driving field  $f$  (electric, magnetic or both) is adjusted so that all maxima in odd lines ( $i = 2m + 1$ ) (light stripes in figure 14) of scanning correspond to minima in even lines ( $i = 2m$ ) (dark stripes in figure 14).



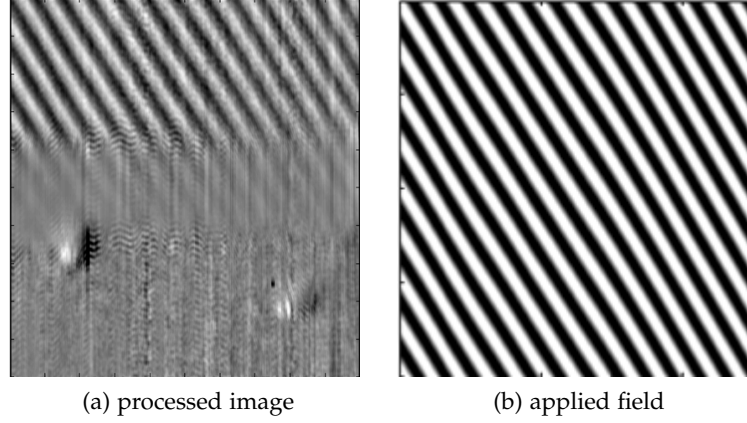


Figure 13: Pattern scanning example

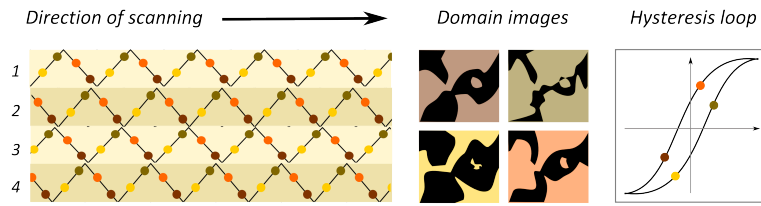


Figure 14: Field pattern scanning

Magnetic and electric field therefore create two different overlapping stripe patterns.

The ferroelectricity can be seen in the acquired image in the same pattern as electric field. Ferromagnetism will give rise to a pattern similar to the pattern of magnetic field. Taking profiles over maxima and minima of both electric and magnetic fields we can quickly evaluate the magneto-electric coupling. Difference in magnetic field frequency variation of signal along maxima and minima line of electric field is direct indication of magneto-electric effect and vice versa.

Because all the maxima in odd lines of scanning correspond to minima in the even lines as mentioned above, the topography suppression is simply done by subtracting odd and even lines of scanned image:

$$C_m = I_{2m} - I_{2m-1}$$

where  $C_m$  is the ferroelectric or ferromagnetic contrast and  $I_m$  is light intensity recorded at  $m$ th line of scanning. This very simple method eliminates the influence of topography efficiently as you can see in the image of a ridge between two platinum electrodes on BTO sample (figure 13). The electrode in the top of the image is connected, the electrode at the bottom of the image is not. It can be readily observed that ferroelectric switching is stronger on the connected elec-



trode than on exposed BTO in the middle while the unconnected electrode shields the signal from BTO underneath.

#### 4.5.2 Dynamics by decomposition

Furthermore the pattern image is decomposed to series of  $N$  images  $H_n$ , where each image contains only points corresponding to given interval  $s$  of increasing or decreasing electric or magnetic field  $V$  with amplitude  $A$ .

$$\begin{aligned} H_n &= I(V \in (ns; (n+1)s)) \\ s &= 2A/N \end{aligned}$$

This sequence of images shows domain dynamics (domain images in figure 14 on the preceding page) while plot of mean values of the signal from each of these images  $\bar{H}_n$  against the corresponding field is overall hysteresis loop from the scanned region (hysteresis loop in figure 14 on the facing page).

To maintain diffraction limited resolution  $R_{dl}$  in the dynamic images the resolution of pattern image  $R_{pi}$  has to be  $N$  times better:

$$R_{pi} = R_{dl}/N$$

Typically to recover dynamic sequence of 20 images the scanning resolution should be set to 20nm (with diffraction limit 400nm). It is also clear that the pixel size of each of the images will be  $N$  times smaller than that of original image. The pixel size is therefore set to 2000x2000 to produce a dynamic sequence of 44 300x300 images from 40x40  $\mu m$  region.

As mentioned before, all this can be done simultaneously with two detectors. So we have, for example, both image of magnetic circular birefringence on balanced detector and magnetic linear birefringence on the single detector. Because of different nature of ferroelectricity and ferromagnetism, the two channels can be configured to have very different sensitivity to each of these effects further facilitating their separate evaluation.

So typically within a couple of minutes we get a map of 40x40 $\mu m$  region with information about ferroelectric and ferromagnetic properties, domain dynamic and hysteresis loop.

All this, of course, becomes even more useful when done at temperatures continuously varying from 4K to 400K once coupled with cryostat.

Example of a pattern scanning is in figure 13a. There is transparent platinum electrode on the top, through which a strong ferroelectric signal is observed, in the middle is a region of exposed BTO, where a weaker signal is visible, on the bottom another platinum electrode shields ferro-electric signal and no pattern is visible anymore. It's important to note that investigating the same effect with a PFM would

not yield a better resolution. The lateral resolution would be determined by the thickness of the top electrode rather than the tip radius.

#### 4.5.3 *Locking-in the Electric and the Magnetic Field*

Holding a pattern image of a sample we might wish to have all this information evaluated at each point. To do this, yet another novel method was developed. To increase signal to noise ratio and precision of the measurement we introduce tandem frequency lock-in amplifier. Tandem frequency operation enables recuperation of signal at two frequencies simultaneously. Or more precisely signal recovered at one frequency is immediately passed to second frequency and amplified again. So using both frequency of magnetic field and frequency of electric field as a reference frequency of lock-in amplifier we can directly recover magneto-electric effect and electro-magnetic effect, while simultaneously measuring ferroelectricity at the frequency of electric field of ferromagnetism at the frequency of magnetic field see figure 10.

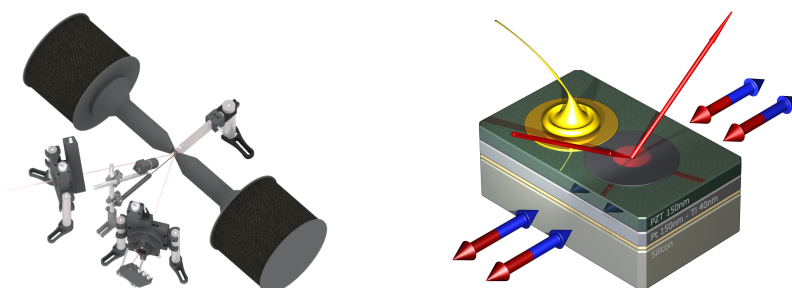
## HIGH FREQUENCY MAGNETO-ELECTRIC COUPLING SETUP

By measuring the optical response in electric field frequency spectrum we can get a fresh view of the magneto-electric coupling. Interestingly we could evaluate the magneto-electric coupling strength without any applied magnetic field which is especially useful for systems that saturate at high magnetic fields.

Additionally, we have achieved an unprecedented methodology that allows disentangling two different contributions to the magneto-electric coupling: surface-mediated and strain-mediated magneto-electric effects. At the same time, we could analyze separately their dynamics, by measuring the frequency dependence of their strength.

The results are described in detail in Chapter 10, 11 and 12. Here we outline the technical characteristics of the setup that was developed in the group of Salia Cherifi at IPCMS in Strasbourg for such kind of experiments.

This setup allows for very wide range of angles of incidence (up to  $70^\circ$ ) in longitudinal configuration (magnetic field in plane of the sample and plane of incidence).



- (a) Magnet core extensions are used to allow for wider angle of incidence options ( $30^\circ$ - $70^\circ$ ). Polarizer-PEM assembly with variable angle(left) allows for automatic selection of any incident polarization state.
- (b) Measurement geometry: Red arrow shows the direction of incident and reflected HeNe laser light. Magnetic field applied in the direction of red/blue arrows. Electric field es applied between top gold electrode and bottom platinum electrode.

Figure 15: Detailed model of the high-frequency magneto-electric coupling setup

It's also suitable for through-the-core polar Kerr effect measurements. However, this setup doesn't have a scanning element, so the measurement is done on a single spot.

The 3D model of the setup is shown in figure 15a, a schematic image in figure 16.

### *Setup Specification*

The setup is designed for frequency of operation in kHz range where the use of PEM is due to its typical frequency of 50 kHz very limited. Because of that a balanced detection technique was used instead. Standard MHz scanning rate balanced detector allows for detection up to 200kHz.

Measured signal is change of linear polarization upon reflection from the sample. It is measured using a continuous wave red He-Ne laser (632.8nm) as the light source. Principle of operation, however, allows introduction of white light with monochromator for spectral measurements. The laser sources are mounted directly on optical table to prevent polarization or intensity losses and fluctuations. The laser light is linearly polarized by a Glan-Thompson calcite polarizer with extinction ration 100000:1 and then reflected onto a balanced photo-detector that is fixed on a nanorotator together with a Wollaston prism. Wollaston prism with same extinction ratio as polarizer and 20° angular deviation is used to distribute the light to the sensors of balanced detector.

Both polarizer and Wollaston prism are mounted on Thorlabs® Nanorotators for automatic nulling: Prior to a measurement, the nanorotator assembly is rotated to a position where both channels of the balanced photo-detector have equal intensity (nulling position). In this configuration, we measure the differential signal in channels A/B of the photodetector, i.e.  $\theta=(I_A-I_B)/2(I_A+I_B)$ , where  $I_A$  is intensity at detector A and  $I_B$  is intensity on detector B. The measured  $\theta$  is related to the optical polarization contrast (i.e., birefringence/dichroism...) induced by the application of magnetic or electric fields. There is a camera included in the setup necessary for precise positioning of the focal spot on the measured structure, because typical dimensions of measured structures and focal spot are around 50µm.

PEM is included in the setup for optional measurements of MCD and Kerr ellipticity measurements. PEM's modulation frequency of 50kHz, however, limits its use in kHz region.

### *Data Acquisition Unit*

This setup was fitted with data acquisition unit (DAQ) that allows multiplexor-free fully-simultaneous measurement of 4 channels at rate of 2.5MSps with 14bit per sample. Because the aim of the setup is recording of the full hysteresis loop at frequencies up to 200kHz, there is a strong need for averaging of multiple consecutive loops. At the same time, the measurement time is required to be as short as

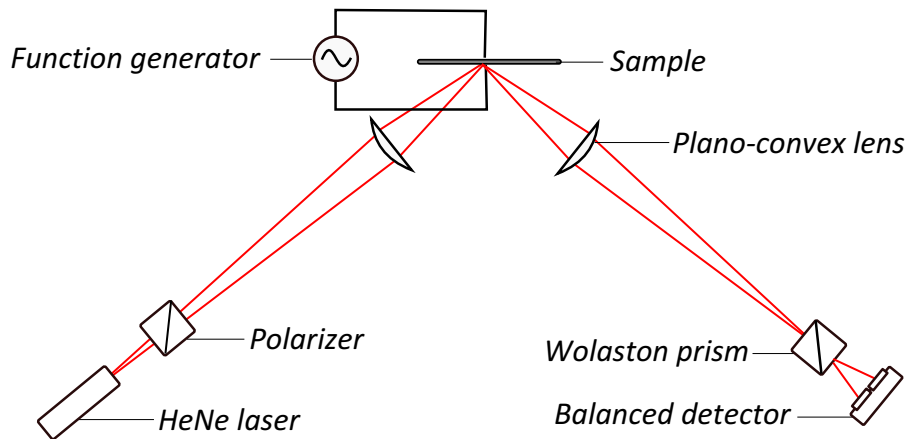


Figure 16: High frequency magneto-electric setup

possible in order to minimize temperature drift influence and sample damage probability. So there is obvious need of recording as many data points as possible in limited time. Multiple channel continuous data acquisition at MHz rates requires stable hard-drive writing speeds at the order of 50 MBps. To avoid limitation by writing speed of the hard-drive, the setup was fitted with solid-state drive with writing speed above 100MBps.

#### *Function Generators*

The frequency generator used produces reliable triangular waveform only up to 35kHz. Above that value, the less preferable sinusoid wave function has to be used. Above 50Hz and when the electric field frequency coincides with any harmonic order of power line frequency, the signal needs to be passed through digital band-stop filter as power line frequency distorts the signal. Alternatively both detector and data acquisition unit would have to be powered from independent battery.

#### 5.1 LIMITATIONS

The frequency and amplitude of the applied magnetic field is limited by inductance of the electromagnet coil, and for typical amplitude of 0.5 T, the maximum magnetic field frequency is limited to about 2Hz.

On the other hand, the maximum amplitude of the applied electric field is 500V, so it's mostly limited only by electric breakdown of the sample. The electric field frequency is limited by the acquisition speed of 2.5MSps (samples per second) as well as the detector scanning rate (1MHz).

## 5.2 DETECTION MODES

### *Standard Magneto-optical Kerr Effect Measurement with Balanced Detector*

This mode is included mainly for reference. Prior to any ferro-electric measurement, it's advantageous to measure standard magnetic hysteresis. Saturation signal of electric field induced polarization change can be then directly compared to saturation signal of magnetic hysteresis to calculate the portion of magnetization vector that has been switched with electric field.

### *Kerr Ellipticity and Kerr Rotation with PEM*

The balanced detector of the setup can be switched for standard single sensor detector for Kerr rotation and Kerr ellipticity measurements using photo-elastic modulator.

### *Electric Field Induced Polarization Changes in kHz Range*

Finally, the main function of the setup. In this mode of operation, full hysteresis loop is recorded at each frequency, allowing for further processing and separation of many contributing effects (magneto-electric coupling, magnetostriction, strain driven birefringence and electro-optic effect).

## Part II

### MAGNETOELECTRIC DOMAIN IMAGING WITH SUB-MICRON LATERAL RESOLUTION

A likely key player in the range of future information technologies is the cross-coupling between ferroelectric polarization and magnetism, allowing eventually an electric-field control of data stored in magnetic bits. In magnetoelectric systems, e.g., ferroelectric/magnetic bilayers, the interplay between both degrees of freedom may emerge either by mechanical constraints or by purely electrostatic effects. The present experimental approaches to the dynamics of magnetoelectric coupling – and its response mapped at small scales – are hampered by the severe difficulty of having simultaneous direct access to the magnetism and ferroelectricity. Here we show how the polarization of light can be used as a probe of both physical magnitudes and spatial distribution of magnetoelectric coupling.

By analyzing linear electro-optic and magneto-optic effects in Pt/ BaTiO<sub>3</sub>/ La<sub>2/3</sub>Sr<sub>1/3</sub>MnO<sub>3</sub> we have uncovered a room-temperature strikingly large magnetoelectric coupling, whereby the ferroelectric-related birefringence is modulated about 50% on average. A largely non-uniform distribution of the local magnetoelectric response was found, that we assign to a mesoscopic texturing of electronic phases at the BaTiO<sub>3</sub>/ La<sub>2/3</sub>Sr<sub>1/3</sub>MnO<sub>3</sub> interface. Such large effects poise strongly correlated electronic systems as a suitable platform for large room-temperature magnetoelectric responses.





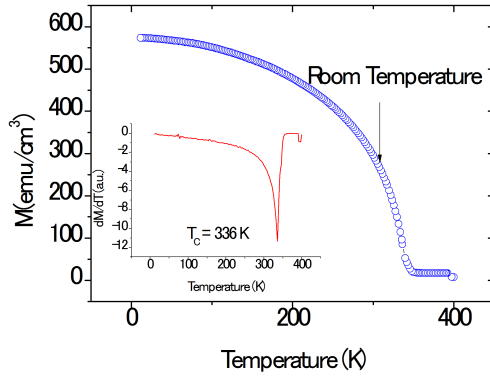


Figure 17: Temperature dependence of the magnetization of the LSMO thin film, measured by SQUID magnetometry under and applied field of  $H = 1000$  Oe. The Curie temperature –defined by the peak of the derivative  $dM/dT$ , see the inset – is  $T_C \approx 336$  K. The optical birefringence experiments were done at room temperature (signalled by an arrow in the M-T curve).

Electron carriers in solids are endowed with both charge and spin. Yet conventional electronics deals solely with charge to transmit and process data, regardless of the spin state. Controlling the spin degree of freedom by electric fields is, however, one of the most coveted goals in spintronics, as it would pave the way to faster data processing and low energy-consumption electronics in which the information is stored magnetically and manipulated electrically [12, 13, 14]. Materials with intrinsically large cross-coupling between magnetism and dielectric properties at room temperature are, however, very scarce. Beyond single-phase materials, an alternative approach is based on extrinsic hybrid multiferroics combining ferroelectric and magnetic systems [15], in which the magnetism is modulated either by mechanical means – via the concerted action of piezoelectricity and magnetostriction effects [16, 17, 18] – or by purely electrostatic effects [19, 20, 21, 22] –i.e., whereby the spin-orbit coupling is modulated via redistribution of electrons in orbitals.

The full development of this magnetoelectric coupling for applications requires a deep understanding of its dynamics and local response. This can be achieved provided that the magnetic and dielectric degrees of freedom are accessed at the same time and that both can be mapped out with high lateral resolution. Recent advances based on atomic force microscopy have allowed a direct visualization of magnetoelectric domains in multiferroic crystals at low temperature [23]. Notwithstanding, large room-temperature magnetoelectric coupling commonly requires structures combining ferroelectric and magnetic layers. In this context, light is an excellent probe as it pro-

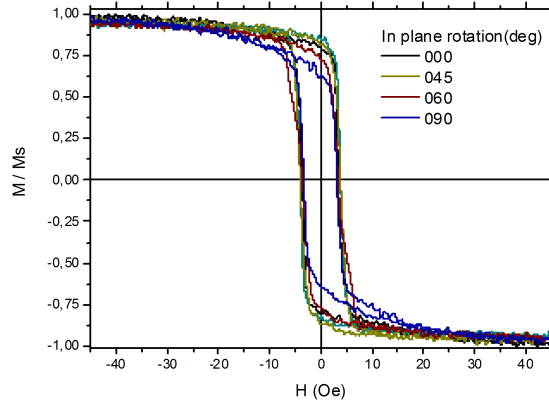


Figure 18: Hysteresis loops measured at room temperature for magnetic fields applied along different in-plane directions.

vides access to magnetoelectric effects emerging at deeply buried interfaces in such composite systems. Additionally, diffraction-limited lateral resolution allows imaging such phenomena at length scales well below the micron in the visible. For instance, optical second harmonic generation has been used for time-resolved imaging of magnetoelectric switching in multiferroic crystals [24, 25].

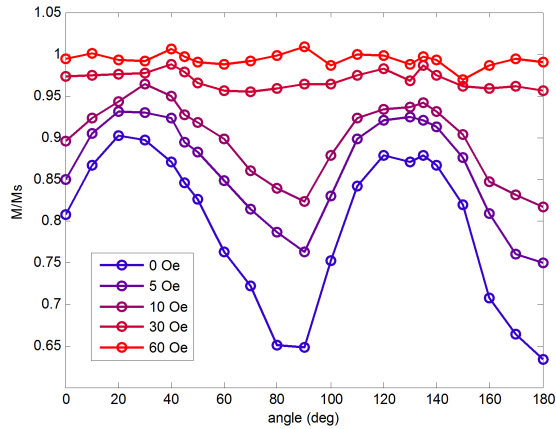


Figure 19: A biaxial magnetic anisotropy is evident from these measurements. Note that at fields above 20 Oe the magnetic anisotropy is suppressed.

While these non-linear optical phenomena are present in noncentrosymmetric crystals as well as at interfaces between centrosymmetric media [26], exploiting light polarization to sense the magnetic and dielectric states may have a broader applicability in some cases. In particular, linear electro-optic and magneto-optic effects induce birefringence/dichroism on polarized light transmitted through or reflected from a ferroelectric or magnetic medium, respectively, resulting in rotation/ellipticity of the light polarization [1, 27, 28]. While

linear electro-optics still requires noncentrosymmetric structures –as found intrinsically in ferroelectrics–, magneto-optic effects are manifested in the presence of any magnetic field, regardless of symmetry [29].

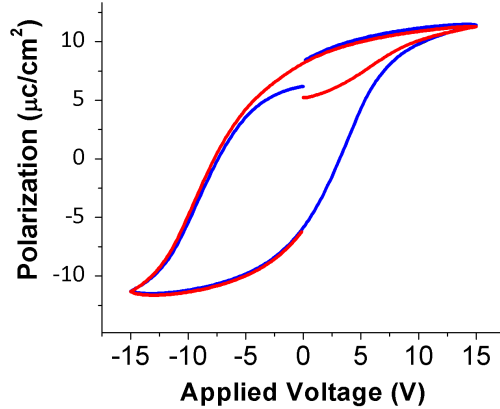


Figure 20: Ferroelectric polarization – electric field loop of the Pt/ BTO/ LSMO sample measured at room temperature

Recently, the potential of light polarization contrast for domain imaging has been demonstrated in ferroelectric/magnetic bilayers, where the effects of ferroelectric imprint on the magnetic domain structure and properties were observed [30, 31, 32]. Here we have taken the outstanding potential of this optical microscopy to a new level. We have measured the electro-optic and magneto-optic effects at room temperature of a Pt(10 nm)/BaTiO<sub>3</sub> (120 nm)/La<sub>2/3</sub>Sr<sub>1/3</sub>MnO<sub>3</sub> (40 nm) trilayer grown on a (001)-oriented lanthanum strontium aluminum tantalum oxide (LSAT) substrate (see Figures 17, 18 and 19 for magnetic characterization). Using La<sub>2/3</sub>Sr<sub>1/3</sub>MnO<sub>3</sub> as a playground for magnetoelectric effects is of particular interest because of the intimate relationship between magnetism and electric transport in its colossal magnetoresistance, which is manifestly large close to the Curie temperature [33, 34]. Thus, by coupling such a manganite thin film with BaTiO<sub>3</sub>, a room-temperature ferroelectric with large spontaneous polarization  $P_S \approx 27 \text{ C/cm}^2$  [35], large electric-field driven magnetotransport charges are anticipated (the ferroelectric polarization versus electric field hysteresis loop is shown in Figure 20). Confirming such expectations, we found a remarkably large magnetoelectric coupling, whereby the ferroelectric-related birefringence was modulated by magnetic fields by up to about 50% on average. Furthermore, using advanced optics we mapped out the spatial distribution of the magnetoelectric coupling strength with diffraction-limited lateral resolution (well below the micron for visible light), finding local variations of up to 20% around the average value. We propose that the origin of such a large effect relies on an electric-field modulation

of electronic phase inhomogeneities at the BaTiO<sub>3</sub>/ La<sub>2/3</sub>Sr<sub>1/3</sub>MnO<sub>3</sub> interface, while the observed non-uniform distribution of the magnetoelectric coupling was correlated to spatial variations of ferroelectricity and strain that were quantified also by optical means.

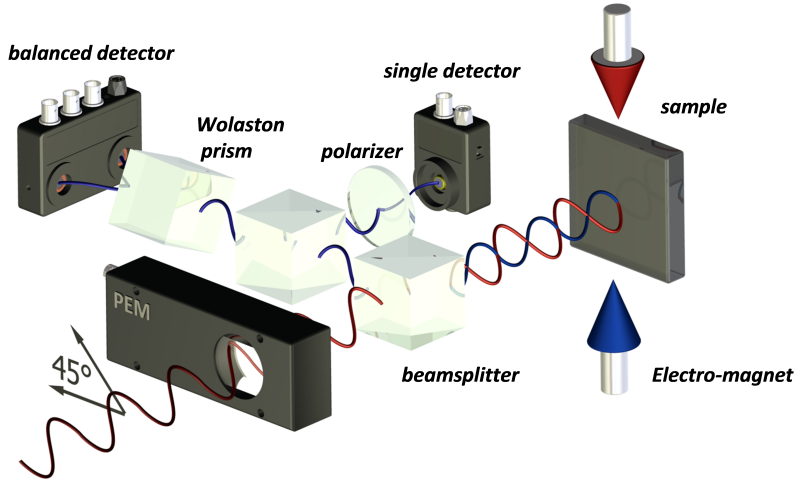


Figure 21: Sketch of the confocal optical arrangement used to map out the birefringence

We adapted a confocal optical arrangement to measure the rotation and ellipticity of the polarization of light in reflection (see Figure 21). For that purpose, light coming from a red He-Ne laser ( $\lambda = 632.8$  nm) with TEM<sub>00</sub> profile was polarized and focused to the specimen surface – or any other internal interface – by means of a high-numerical aperture ( $NA = 0.68$ ) objective lens. After reflection, the light intensity was collected simultaneously by two kinds of detectors. First, a couple of balanced detectors sensed the s- ( $I_S$ ) and p- ( $I_P$ ) polarized components split up by a Wollaston prism (Figure 21). On the other hand, a second single detector was used to measure the changes in the light intensity after going through an analyzer crossed with respect to the polarizer before the sample (Figure 21) Prior to measurements, both kinds of detectors were adjusted to have a null signal. Upon application of electric fields, the induced birefringence unbalances the intensity collected by the detectors by an amount that in the case of the balanced detection equals:

$$\theta = \frac{I_S - I_P}{I_S + I_P} \quad (17)$$

In these experiments, the La<sub>2/3</sub>Sr<sub>1/3</sub>MnO<sub>3</sub> layer acted as a bottom electrode, whereas platinum (Pt) circular contacts with thickness  $t_{Pt} \approx$

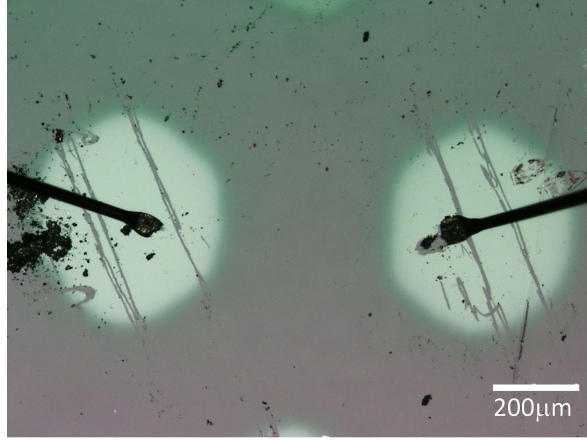


Figure 22: Micrograph showing two Pt electrodes on top of the BaTiO<sub>3</sub>/La<sub>2/3</sub>Sr<sub>1/3</sub>MnO<sub>3</sub> bilayer

10 nm and diameter  $\phi \approx 500 \mu\text{m}$  were deposited on the top (Figure 22 shows an optical micrograph with a view of two Pt top contacts).

The heterostructures were grown by pulsed laser deposition using a single process. The BaTiO<sub>3</sub> and La<sub>2/3</sub>Sr<sub>1/3</sub>MnO<sub>3</sub> layers were grown at 700 °C and 725 °C, respectively, on a LSAT 001-oriented substrate. The growth proceeded at 5 Hz of laser frequency, and the partial pressures at the deposition were 0.2 mbar for La<sub>2/3</sub>Sr<sub>1/3</sub>MnO<sub>3</sub> and 0.02 mbar for BaTiO<sub>3</sub>. Pt metallic contacts for electrical measurements (area  $\approx 0.2 \text{ mm}^2$  and thickness  $\approx 10 \text{ nm}$ ) were deposited ex situ by rf-sputtering. The ferroelectric polarization was measured using an AixAcct Co. TFAlyser 2000. We note here that the BaTiO<sub>3</sub> film grown in the given conditions was c-oriented with the ferroelectric polarization along the out-of-plane direction [36, 37]. For the optical measurements the beam spot was raster-scanned over the surface defining a mesh of  $N_V \times N_H$  points determined from the number of vertical ( $N_V$ ) and horizontal ( $N_H$ ) pixels. Along the scanning direction, the applied electric fields were modulated in intensity according to a triangular wave profile with a periodicity  $1/\nu_e \approx 10 \text{ ms}$  describing a pattern over the scanned area (Figure 23b), whereas the birefringence –see Equation 17– was sampled at a rate  $1/\nu_b = 25 \text{ kHz}$ . From these datasets, the corresponding matrices were defined:

$$\begin{aligned} \mathbb{E}_{ij} &= \begin{bmatrix} E_{11} & E_{12} & \dots \\ E_{21} & E_{22} & \dots \\ \dots & \dots & \dots \end{bmatrix} \\ \bar{\theta} &= \begin{bmatrix} \theta_{11} & \theta_{12} & \dots \\ \theta_{21} & \theta_{22} & \dots \\ \dots & \dots & \dots \end{bmatrix} \end{aligned} \quad (18)$$

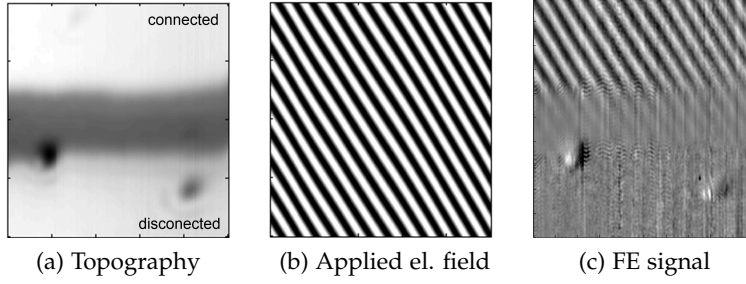
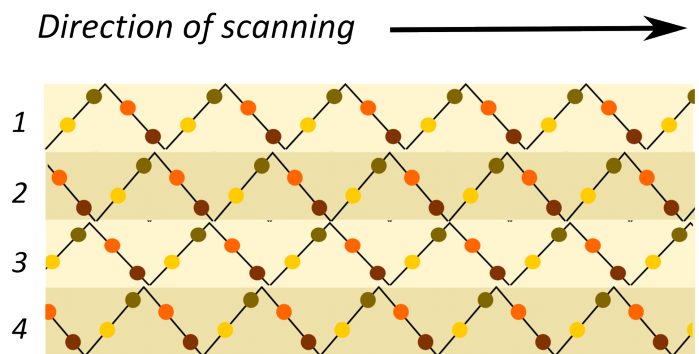


Figure 23: Example of quick evaluation of FE response of a sample using field pattern

where  $(i, j)$  denotes the position in the  $N_V \times N_H$  mesh. By this procedure we obtained a multidimensional array of data, in which the optical birefringence was recorded as a function of space and applied field. For instance, depending on its position in the sequence of applied fields, a particular value of the applied electric field  $E_{ij}$  was located either over the upper or the lower branch over a cycle, so that  $\theta_{ij}-E_{ij}$  hysteresis loop could be obtained over a given area from the matrices defined by Equation 18 (see Figure 24c). Alternatively, the optical birefringence could be mapped out for each specific value of the applied field, thus obtaining the local birefringence response distributed spatially over the area under analysis (Figure 24b).

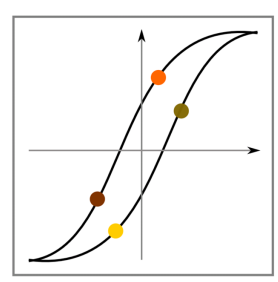
To exemplify this procedure, let us analyze the measurements carried out over a small region on the Pt contact, signaled by the small red square in Figure 22. One side of the surveyed area was connected to the contact wire –and, thus, electric fields could be applied on it–, whereas part of the remaining area was electrically disconnected by a deep scratch. An image of the topography of the same area was obtained by confocal microscopy (Figure 23a), showing the presence of a deep trench between the electrically connected and disconnected regions of the Pt electrode. As expected in the electrically connected area, a pattern of optical contrast in the birefringence  $\theta_{ij}$  was measured with a spatial modulation (Figure 23c) in agreement with the frequency of the applied fields (Figure 23b). On the contrary, the optical contrast became significantly weaker in the area of the trench and was smeared out over the electrically disconnected area (Figure 23c), proving that the observed contrast resulted from the field-driven electrical polarization of the ferroelectric.



(a) Each dot corresponds to one measurement point



(b) Domain images corresponding to each set of points



(c) Average of each set of points corresponds to a point in a hysteresis loop

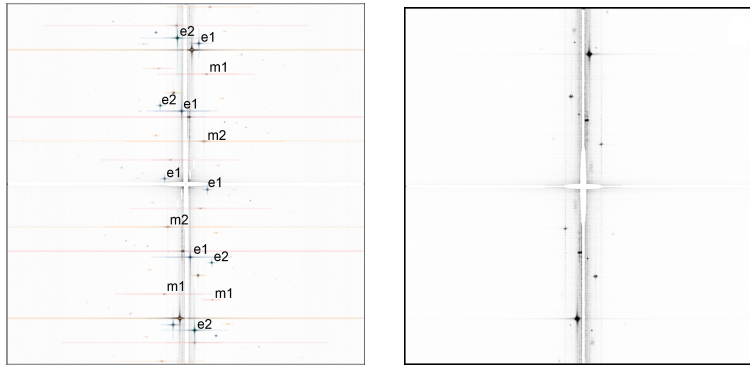
Figure 24: Schematics of scanning pattern



## VISUALIZATION OF DOMAIN WALLS

Aiming to visualize the domain structure, triangular-wave electric and magnetic fields of intensity 50 Oe and 10 V, respectively, were applied simultaneously with modulation frequencies  $\nu_e = 133.86$  Hz and  $\nu_m = 93.9$  Hz, respectively, defining a pattern over the analyzed area, while the birefringence  $\theta_{ij}$  was measured at a sampling rate  $\nu_b = 40$   $\mu$ s. In order to extract the location of domain walls, the  $\theta_{ij}$  data and field reference data were first transformed into the Fourier space  $\Theta_{hk}$  by

$$\Theta_{h,k} = \frac{1}{N_V N_H} \sum_{p=0}^{N_H-1} \sum_{q=0}^{N_V-1} e^{-i2\pi\left(\frac{ph}{N_H} + \frac{qk}{N_V}\right)} \quad (19)$$



(a) Fourier transform of the signal from the single detector (b) Fourier transform of the signal from the balanced detector

Figure 25: Signal (black) is overlaid with Fourier transforms of the first and second harmonic of the applied electric (blue e1, e2) and magnetic (red m1, m2) fields. For higher contrast, the topography signal was suppressed (white cross in the center). White dots close to the center correspond to the suppression in the filter of the power line frequency.

Note that the periodicities  $\nu_e$ ,  $\nu_m$  and  $\nu_b$  were adjusted so that maxima of magnetic field and maxima of electric field form a cross pattern with below diffraction limit mesh size in  $N_H \times N_V$  plane. Reciprocal data space of the signal captured in the single and balanced detectors are shown in Figures 25a and 25b, respectively. In these Figures, a finite number of peaks appear in correspondence to the Fourier transforms of different harmonics of the modulation frequencies (the first and second harmonics are labeled by color in figure 25a). Note that the intensity of the reciprocal peaks fades away rapidly for

harmonics with increasing frequency in this Fourier transform of a triangular wave with period of  $2L$ :

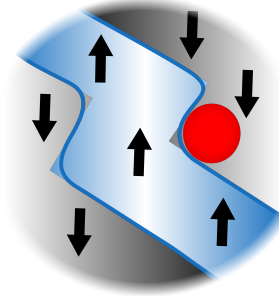
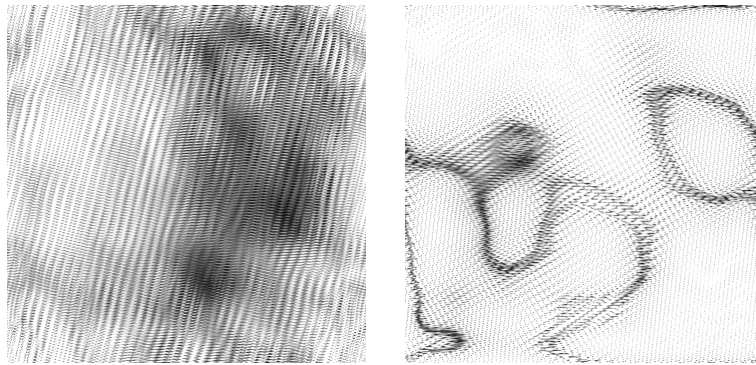


Figure 26: The diffraction limited measurement spot (red) is inevitably convoluted in the measured shape of domain walls (blue line). Even if actual domain walls have sharp edges the optically measured domain walls will have the curvature determined by diffraction limit.

$$F(x) = 8/\pi^2 \sum_{n=1}^{\infty} \frac{-1^{n-1/2}}{n^2} \sin\left(\frac{n\pi x}{L}\right)$$

Bearing this in mind, the reciprocal space  $\Theta_{h,k}$  was then transformed into  $\Theta_{h,k}^f = \Theta_{h,k} w_{h,k}$  by using a circular filter around each reciprocal peak  $(h, k)$ . The circular filter was defined to have a radius equal to the full width at half maximum  $r_{\text{FWHM}}$ , i.e.,  $w_{h,k}(r) = 1$  for  $r \leq r_{\text{FWHM}}$  and  $w_{h,k}(r) = 0$  elsewhere, being  $r = 0$  at the center of each reciprocal peak of the corresponding field. After that,  $\Theta_{h,k}^f$  was converted back to the real space data  $\theta_{h,k}^f$  by inverting the Fourier transformation of Equation 19, obtaining the spatial distributions of the signal filtered with electric field (Figure 27a) and with the magnetic field (Figure 27b).

This mathematical procedure enabled the visualization of those domain walls that, after repeated cycling, always stayed pinned at the same location, e.g. by defects. At low fields, when the system is in a multidomain state (Figure 26), as the light spot is scanned over the sample surface, it occasionally spans across a given domain wall. When that occurs, the birefringence measured at that location has contributions of opposite sign associated to neighboring domains. Thus, at locations where the domain walls are repeatedly pinned, the Fourier filter yields values of the local birefringence  $\Theta_{h,k}^f$  that are lower than the surroundings, thus allowing visualization of domain walls. Note that due to the expected small size of ferroelectric domains in thin films [38], their corresponding domain walls can not be resolved within the diffraction limit after the inverse Fourier transformation (Figure 27a). Contrarily, ferromagnetic domains are significantly larger and can be visualized, as shown in Figure 27b.



(a) The signal filtered with electric field (b) The signal filtered with magnetic field

Figure 27: Because the typical ferroelectric domain size is smaller than the diffraction limit its domain structure cannot be resolved while the bigger magnetic domains are visible

Note, however, that although in some cases the domains can not be resolved, the local ferroelectric and magnetic responses can always be studied from the optical birefringence and mapped out within diffraction-limited lateral resolution. This topic is developed in the following.



## MAPPING FERROELECTRICITY, MAGNETISM AND STRAIN

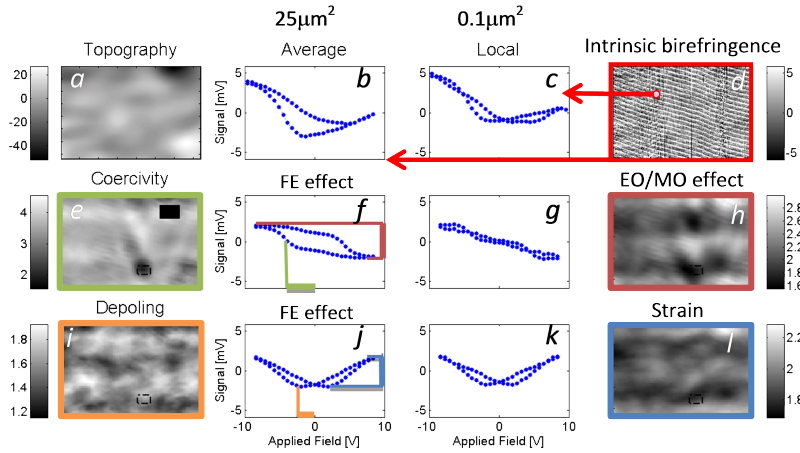


Figure 28: Mapping out the electro-(magneto-) optic signal and strain from birefringence. Hysteresis loop averaging allows screening out the topography (a) from the detected signal. The spatial distribution of the intrinsic birefringence is shown in (d). The electro-optic (EO)/magneto-optic (MO) and strain contributions are mapped out in (h) and (l), respectively. From EO/MO one can extract the distribution of coercive fields (e) and, conversely, from strain one can map out the depoling fields (i). The central figures in each of the three rows plot the hysteretic loops of the intrinsic birefringence, EO/MO effect and strain, either averaged over the whole area, or the corresponding local response – small square box in (e) and (i) –.

Figure 28 shows data obtained from optical measurements done over a different region on the Pt top electrode. The separation of topography-related effects from the measured birefringence was done by centering each extracted loop, i.e., after averaging the signals at remanence over the upper and lower branches of the hysteretic loop. We used this mathematical protocol to thwart any cross-talk effect from topology, e.g. due to even tiny fluctuations of the Pt electrode thickness that could interfere with the as-measured birefringence. Indeed, after this procedure, such kind of spurious effects, not related to any intrinsic birefringence response, could be imaged, as shown in Figure 28 a.

Subsequently, the  $\theta_{i,j}^f$  data could be processed to obtain the intrinsic birefringence mapped out over the whole scanned area (Figure 28 d), see also the hysteresis loops averaged over the region (Figure 28 b). Note that these loops were significantly different from that obtained

by measuring the displacement currents in a standard polarization – electric field characterization (see Figure 20 on page 41 ). The reason is that two different phenomena contribute to the birefringence. On the one hand, we have that fraction that comes from the linear electro-optic or magneto-optic effects, i.e., related to the ferroelectricity (FE) or magnetism (MG), that exhibits odd parity with respect to the electric field  $E$ , i.e.

$$\theta_{i,j}^{FE/MG} (E_{inc}) = -\theta_{i,j}^{FE/MG} (-E_{dec})$$

where  $E_{inc(dec)}$  are values of the applied electric field over the hysteresis branches corresponding do increasing and decreasing field. Note that due to the magnetoelectric coupling, both FE and MG effects may come up after application of an electric field (more details are given below). Conversely, a strain-driven birefringence, arising from the converse piezoelectric effect or magnetostriction (PE/MS), shows even parity with the electric field, that is:

$$\theta_{i,j}^{PE/MS} (E_{inc}) = \theta_{i,j}^{PE/MS} (-E_{dec})$$

It turns out that from any as-measured loop  $\theta_{i,j}^f$  (Figure 28 b), the FE/MG and the PE/MS components can be obtained by mathematical (anti)-symmetrization, i.e.

$$\begin{aligned} \theta_{i,j}^{FE/MG} (E_{inc(dec)}) &= \frac{\theta_{h,k}^f (E_{inc(dec)}) - \theta_{h,k}^f (-E_{inc(dec)})}{2} \\ \theta_{i,j}^{PE/MS} (E_{inc(dec)}) &= \frac{\theta_{h,k}^f (E_{inc(dec)}) + \theta_{h,k}^f (-E_{inc(dec)})}{2} \end{aligned}$$

see Figures 28 f and j, respectively. The saturated values of the electro-optic/magneto-optic  $\theta^{FE/MG} (E)$  loops are signaled by the red frame in Figure 28 f, whereas the corresponding coercive fields are visualized by the orange frame. Conversely, the piezoelectric-driven birefringence  $\theta^{PE/MS}$  loops are proportional to the electrically induced strain (blue frame in Figure 28 j), whereas depoling fields are extracted from the respective turning points in the loops (as indicated in the purple frame in Figure 28 j).

Using the same mathematical protocol, the birefringence  $\theta_{h,k}^f$  loops were extracted for smaller regions (signaled by the square small box in Figure 28 i), obtaining the local response to the applied electric fields (Figure 28 c). We note that the size of these regions was shrunk down to the theoretical diffraction-limited lateral resolution given by  $\Delta r \approx 0.44\lambda/2NA$  [10], which, for  $\lambda = 632.8$  nm was  $\Delta r \approx 400$  nm. Likewise, the local electro-optic/magneto-optic and piezoelectric loops were obtained, see Figure 28 g and k, respectively. It is evident from these figures that depending on the position, significant variations with respect to the average loops can be observed in the ferroelectric/magnetic and piezoelectric/magnetostriction responses. This information was then used to map out over the whole scanned area the

spatial distribution of the saturated  $\theta^{FE/MG}$  values (Figure 28 h) and coercive field (Figure 28 e), as well as the strain at maximum applied field (Figure 28 l) and the depoling fields (Figure 28 i).

The mappings displayed in Figures 28 e, h, i, l unveil very relevant information. First, a visual inspection of Figures 28 h, l clearly points towards a close correlation between the saturation value of the electro-optic/magneto-optic  $\theta^{FE/MG}$  and the piezoelectric/magnetostriction loops. More specifically, larger values of strain –brighter tones in Figure 28 l– are correlated to larger values –brighter tones– of  $\theta^{FE/MG}$  saturation (Figure 28 h). Viceversa, the smaller the strain, the lower is the saturated –darker regions in both Figures–. Similarly, the coercivity ( $\theta^{FE/MG}$ ) and depoling field ( $\theta^{PE/MS}$ ) mappings (Figures 28 e, i) also show a relationship with the spatial distribution of the saturated  $\theta^{FE/MG}$  and strain  $\theta^{PE/MS}$ . This is not surprising, as a larger piezoelectric strain response is expected for larger values of  $\theta^{FE/MG}$ , provided that the latter is dominated by the electro-optic (i.e., ferroelectric) contribution. Note, however, that whereas the variations of strain are relatively moderate –with fluctuations less than approximately 20% over the whole scanned area, see Figure 28 l–, the electro-optic/magneto-optic loops suffer dramatic changes. This is clearly seen when comparing the loops displayed in Figures 28 f, g, j, k: while the local (Figure 28 k) and averaged (Figure 28 j) strain loops look very similar, the corresponding saturated  $\theta^{FE/MG}$  loops –Figures 28 g, f, respectively– are noticeably different. This manifests that in addition to the dominant electro-optic (ferroelectric) contribution to  $\theta^{FE/MG}$ , a supplementary magneto-optic component –in the absence of any applied magnetic field– arises upon application of an electric field.

Such an outstanding magnetoelectric effect can be better visualized by displaying the  $\theta^{FE/MG}$  and  $\theta^{PE/MS}$  spatial distributions for different values of the electric field  $E$ . More specifically, Figure 29 shows the mappings of the electro-optic/magneto-optic  $\theta^{FE/MG}$  and piezoelectric strain/magnetostriction  $\theta^{PE/MS}$  birefringence referenced to their values averaged over the whole scanned area. Thus, yellow-colored regions in Figure 29 correspond to the zones where the measured birefringence is above the averaged value, whereas blue-colored areas are related to values below the average. Again, for large applied fields, the regions with the largest positive (Figure 29 a) or negative (Figure 29 i) saturated  $\theta^{FE/MG}$  are correlated to the areas showing a larger piezoelectric strain (Figures 29 d, l). However, for electric fields close to the depoling field there are regions –see e. g. the patch enclosed within the box in Figure 29 e– with a large  $\theta^{FE/MG}$  response that is uncorrelated to the strain (Figure 29 h). These are precisely the same regions where the  $\theta^{FE/MG}$  loops are most dramatically divergent from the average; see Figures 28 f and g. All these factors

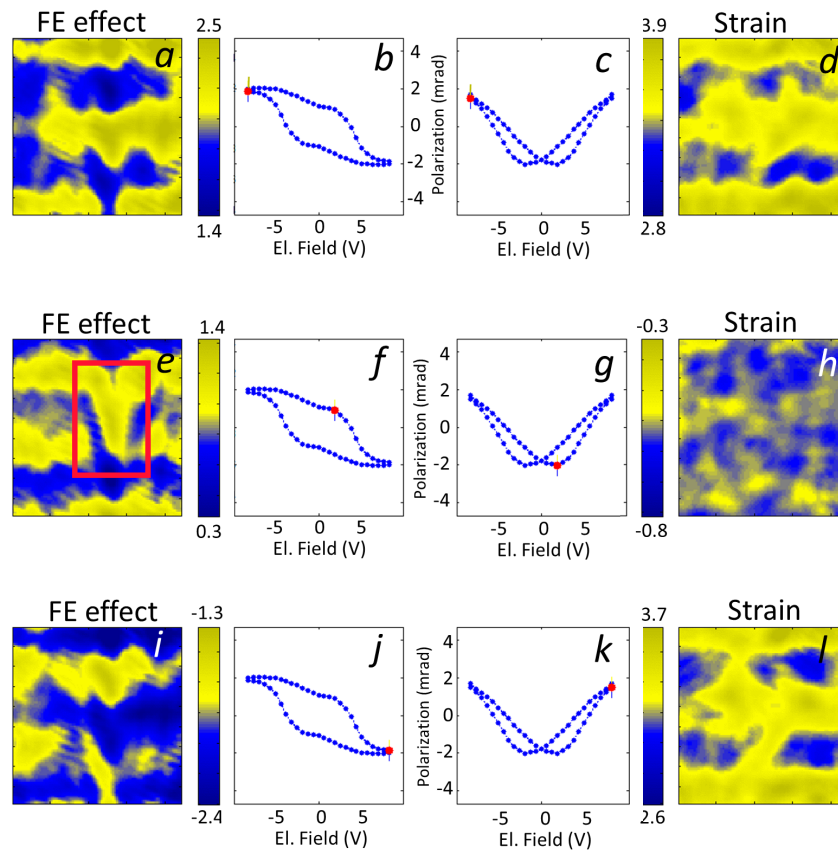


Figure 29: Magnetolectric response from optical birefringence maps. The spatial distribution of the electro-optic/magneto-optic and the piezoelectric strain responses are displayed at different values of the electric field. (a), (i) and (d), (l) show the mappings corresponding the largest positive and negative applied fields, respectively. At intermediate fields, some features in the EO/MO and strain mappings (see the area enclosed within the orange box) arise due to a magnetolectric coupling. Panels (b), (f), (j) and (c), (g), (k) indicate the loci of the electric fields in the averaged EO.MO and strain loops.

then point to large magnetolectric effects coming into play, which is discussed next.



## MAPPING THE MAGNETOELECTRIC COUPLING STRENGTH

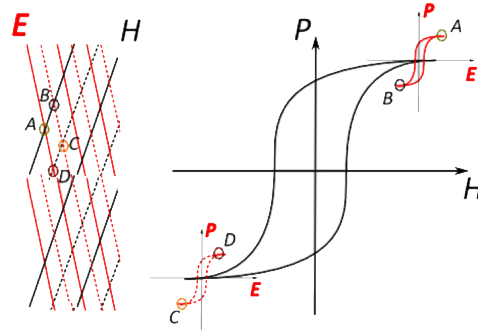


Figure 30: The magnetolectric response is obtained after applying simultaneously electric and magnetic fields, according to the pattern sketched on the left. The optical birefringence loop –schematically shown on the right – is affected by both fields. From the locations of points A, B, C and D in the crossed patterns (left), we define the magnetolectric coupling strength as  $\Delta_{MEC} = \Delta_{AB} - \Delta_{CD}$ , i.e., we quantify the degree of asymmetry in the magnitude of the birefringence loops due to the application of electric fields.

For a quantitative analysis of the magnetolectric coupling, both electric and magnetic fields were applied simultaneously with a modulation frequency of  $\nu_e = 133.86$  Hz and  $\nu_m = 93.9$  Hz, respectively. The light spot scanning over the surface was synchronized with the electric and magnetic fields in such a way as to obtain the field patterns schematically outlined in Figure 30. The positions where the largest positive electric field was applied are depicted by solid red lines, whereas the largest negative values are drawn as dotted red lines. Conversely, black solid (dotted) lines denote the locations where the largest positive (negative) magnetic field was applied. Note that within the mesh of  $N_V \times N_H$  data pixels we can identify a set of locations  $(i, j)$ , of type A, B, C and D (Figure 30). In A- and B-type positions, for a given value of the positive applied magnetic field, the electric field attained two opposite values, positive (A) and negative (B). Alternatively, in C and D locations the electric field had opposite negative (C) or positive (D) values under the application of a magnetic field with sign opposite to that of points (A) and (B). Thus, by cleverly using the multiple combinations of the electric and magnetic fields, the magnetolectric coupling strength could be extracted. Defining  $\theta_A$ ,  $\theta_B$ ,  $\theta_C$  and  $\theta_D$  as the birefringence measured at A, B, C and D locations all around the complete loops, respectively, we can

define the quantities  $\Delta_{AB} = \theta_A - \theta_B$ ,  $\Delta_{CD} = \theta_C - \theta_D$ , from which the magnetoelectric coupling strength can be quantified as

$$\Delta_{MEC} = \frac{\Delta_{AB} - \Delta_{CD}}{\Delta_{AB} + \Delta_{CD}} \quad (20)$$

Put in other words, we measured the degree of asymmetry in the magnitude of the birefringence loops due to the application of magnetic fields (Figure 30). Thus,  $\Delta_{MEC} \neq 0$  indicates an extra contribution to the birefringence –different from that applying just an electric field– that depends on the orientation of an in-plane applied magnetic field. As discussed below,  $\Delta_{MEC}$  is indeed remarkably large in  $\text{BaTiO}_3/\text{La}_{2/3}\text{Sr}_{1/3}\text{MnO}_3$  (roughly 50%). This is a rather unexpected outcome, as it implies that for magnetic fields of same intensity but applied along opposite directions the observed magnetoelectric coupling strength is different. While the origin of this phenomenon remains uncertain, we have independently observed the same behavior in other magnetoelectric bilayers, such as Co/ PZT samples (chapter 10), in which surface- and strain-mediated magnetoelectric responses also appear to depend on the direction of the in-plane magnetic field and the magnetoelectric coupling as defined by Equation 20 is similar in magnitude [39].

#### 9.1 NON-UNIFORM MAGNETOELECTRIC COUPLING STRENGTH

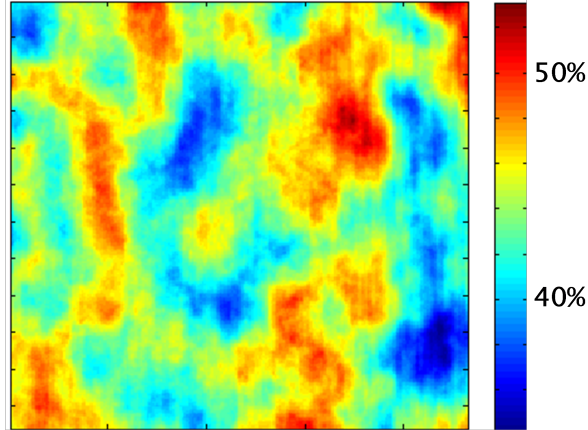


Figure 31: The magnetoelectric coupling strength as  $\Delta_{MEC}$  is mapped out with diffraction-limited resolution all over the analyzed area. The data are quantified as relative variations in the  $\Delta_{MEC}$  intensity given by percentages, showing maximum values above 50%. The scanned area is  $5 \times 5 \mu\text{m}$ .

Figure 31 displays the spatial distribution of the magnetoelectric coupling strength as defined by  $\Delta_{MEC}$  –Equation 20– over the scanned region. The first observation is that an outstandingly large coupling is observed, whereby the electric field-driven birefringence signal is

modulated by magnetic fields by about 50% on average. Yet, the intensity of this coupling is far from being homogeneous. Indeed, over the analyzed region, the magnitude of the magnetoelectric effect is fluctuating within a range  $\Delta_{MEC} \approx 30 - 55 \%$ . The overall picture is that of a non-uniform distribution with an inhomogeneous magnetoelectric response on the micron-scale.

The observation of such a large magnetoelectric response asymmetric with respect to the direction of the magnetic field is far from obvious. One possible scenario relies on the emergence of a complex magnetic configuration at the  $\text{BaTiO}_3/\text{La}_{2/3}\text{Sr}_{1/3}\text{MnO}_3$  interface, in which antiferromagnetic and ferromagnetic regions coexist. The observed magnetoelectric effect would be explained by the modulation of such complex phases by either magnetic or electric fields. For instance, at zero magnetic fields, switching the ferroelectric state would entail a modulation of the manganite interface electronic properties, similarly to the recently observed magnetoelectric effect in  $\text{Pb}(\text{Zr}_{0.2}\text{Ti}_{0.8})\text{O}_3/\text{La}_{0.8}\text{Sr}_{0.2}\text{MnO}_3$  [40]. Additionally, to explain the effect of magnetic field directionality, it is necessary to assume that the interface hosts a pinned complex magnetic configuration that has an initial imprint or bias that, although relatively soft, would give a different response depending on the direction of the in-plane magnetic field. Note that the modulation of the interface magnetism might, in turn, tune the work function of the manganite  $\text{La}_{2/3}\text{Sr}_{1/3}\text{MnO}_3$  layer at the interface, thus changing the effective Schottky barrier and therefore the dielectric properties of the ferroelectric [41, 42] contributing also to the observed magnetoelectric effect. This scenario is also consistent with many experimental evidences about phase coexistence of magnetic/metallic and antiferromagnetic/insulating phases in manganites [43, 44, 45] and with the modulation of magnetism and transport in  $\text{La}_{2/3}\text{Sr}_{1/3}\text{MnO}_3$  using electric fields [46, 47, 48, 49, 50, 51].

According to this picture, the large fluctuations of the magnetoelectric effect  $\Delta_{MEC}$  are closely related to the appearance of multiple-scale electronic phase textures, with inhomogeneities scaling from the nano- to the micrometer scale [52, 53, 54, 55]. The origin of such intricate texturing has been ascribed to the delicate balance between different competing driving forces, including electronic correlations, strain and chemical disorder [56]. In any case, from these considerations, the remarkably large magnetoelectric effect here observed should be ascribed to electrostatic/magnetic modulation of the interface electronic states in the manganite layer and that the observed non-uniform spatial distribution of the magnetoelectric coupling strength is compatible with the direct observation of mesoscale inhomogeneities in manganites [57, 58]. Our results show that the large responsivity of strongly correlated electron systems to external stimuli makes of such systems an ideal platform to achieve large magnetoelectric responses at room temperature.



## Part III

### MAGNETO-ELECTRIC COUPLING DYNAMICS

Magneto-electric coupling under electric field modulated at frequencies around under 1Mhz is an area of investigation with high potential for applications in industry. To record magneto-optical signal at such rate without using stroboscopic methods requires combination of multiple signal recovery techniques. Development of this setup was a study of one of the possible future developments of magneto-optical confocal microscopy ([MOCFM](#)) setup. High-frequency magneto-electric coupling was successfully recorded in several samples.



## HIGH FREQUENCY MAGNETO-ELECTRIC COUPLING

### INTRODUCTION

The cross-coupling of magnetic and ferroelectric properties in multiferroic systems is being intensively investigated for its relevance in emerging electronic applications [59, 60, 16, 61, 62, 63, 64]. An especially outstanding achievement is the electric field control of the magnetic states [65, 21, 66, 67, 17, 68, 36, 69], offering advantages in terms of fast and dissipation-less operation in non-volatile memories.

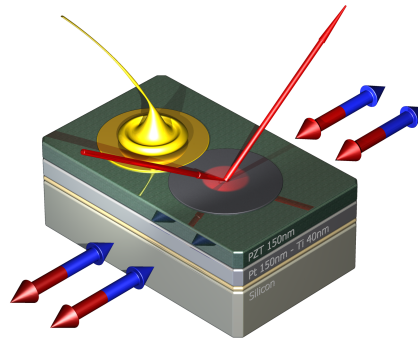


Figure 33: Schematic description of the sample layout and experiment geometry

Therefore, a good understanding on the dynamics of the magneto-electric coupling in multiferroic systems is a requirement for development of applications [70, 68]. In this line, early reports have investigated the dynamics of a variety of single-phase multiferroics ( $\text{BiFeO}_3$ ,  $\text{YMnO}_3$ ,  $\text{RMnO}_3$ ,  $\text{TMn}_2\text{O}_5$  etc.) where the magneto-electric coupling is revealed through the excitation of electromagnons in the GHz-THz region [71, 72, 73, 74, 75, 76].

Nevertheless, the intrinsic magneto-electric coupling in single-phase materials is rather weak [77, 78] and other alternatives are being con-

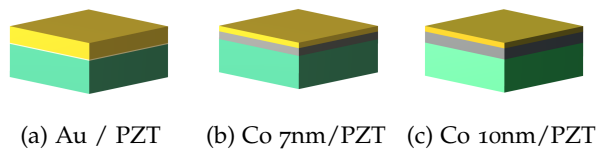


Figure 32: Schematics of used Co/PZT samples

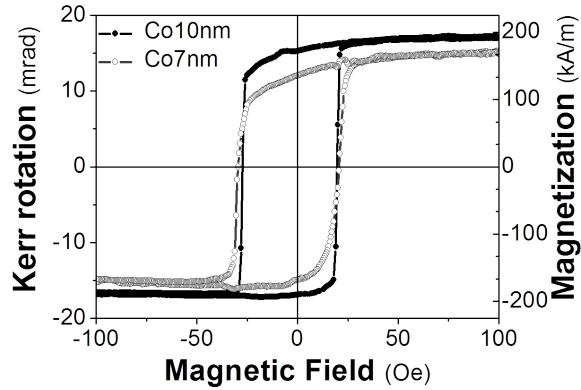


Figure 34: Longitudinal Kerr signal measured in 10nm and 7nm-thick Co deposited on PZT, and the corresponding magnetization value (right-hand side label)

sidered. One of the most promising routes is to couple magnetic and ferroelectric materials in composite systems known as artificial multiferroics. [79, 80, 81, 82, 83, 84, 85, 15]

In artificial multiferroics such as ferroelectric/ferromagnetic bilayers, the interfacial coupling between the ferroic subsystems is induced by two main mechanisms. The one is strain-mediated and it involves the magnetization variation induced by the converse piezoelectric effect through the magneto-elastic interaction [86, 87, 88]; the other is known as interface magnetoelectric coupling and it is electronically driven. [89, 20, 90] It arises from the spin-dependent electrostatic charge screening at the interface between the ferromagnet and the ferroelectric film when the external electric field is swept. The electric field-induced variation of the atomic bonds between the cations in the ferroelectric insulator at the interface with the ferromagnet is also found to play an important role in the interface magnetoelectric coupling (MEC). [90]

While strain is more often found to be at the origin of the magnetoelectric coupling in artificial multiferroics, surface magnetoelectric coupling has been revealed in several bilayers. [91, 40, 22] For example, it has been demonstrated in PZT/LSMO that the electric field-driven depletion/accumulation of spin-polarized electrons at the interface is at the origin of the surface magnetoelectric coupling [85]. The induced magnetization in Ti atoms at the interface of Fe/BTO [92, 64] demonstrates the interface atomic bond proximity effect as predicted by theory [93, 89]. It is however very likely that both strain-mediated and interface MEC coexist in the same system but the two mechanisms could hardly be disentangled.



## SEPARATING MAGNETO-ELECTRIC COUPLING EFFECTS

---

In this study performed at the team of Salia Cherifi at [IPCMS](#), Strasbourg, the room temperature converse [MEC](#) dynamics has been investigated in the kHz regime in Co/Pb(Zr,Ti)O<sub>3</sub> bilayers by measuring the optical response with the electric field sweep frequency. The magneto-optical signal induced by the E-control of the magnetization is disentangled from the overall optical signal using a systematic decomposition and modeling of the optical response in the whole frequency range. This decomposition has allowed furthermore for the separate investigation of the dynamics of strain-mediated and surface magnetoelectric coupling. It results that strain-mediated and surface [MEC](#) components exhibit a dissimilar M-E dynamics, depending on the frequency range and on the magnetic film thickness. While the strain-mediated coupling keeps up with surface magneto-electric coupling up to 1 kHz, above that frequency the surface magneto-electric coupling dominates.

The optical response has been measured using a continuous HeNe laser as the light source. Before impinging on the sample surface, the light is p-polarized by a Glan-Thompson polarizer, and after reflection the light goes to a balanced photo-detector that is fixed on a nanorotator together with a Wollaston prism. This atypical configuration was chosen to avoid using half-wave plate and thus keep depolarizations on optical components to the minimum.

Prior to any measurement, the nanorotator assembly is rotated to a position where both channels of the balanced photo-detector have equal intensity (nulling position). In this configuration, we measure a differential signal in channels A and B of the photodetector. The polarization rotation angle  $\theta$  after reflection is given by the difference over the sum of the intensities measured in channels A and B.

$$\theta = \frac{I_A - I_B}{2(I_A + I_B)} \quad (21)$$

The measured  $\theta$  rotation angle is related to the optical polarization contrast, i.e., to the electric or magnetic field driven magneto-optical Kerr effect rotation or to the electric field-induced electro-optical effect and birefringence, as it will be explained later. A magnetic field can be applied in the film plane allowing standard longitudinal Kerr effect measurements. A function generator was used to produce a voltage of 10 V with a triangular or sinusoidal waveform up to 200 kHz. To ensure continuous data acquisition, i.e., real-time measurements of four measurement channels (magnetic field, electric field,

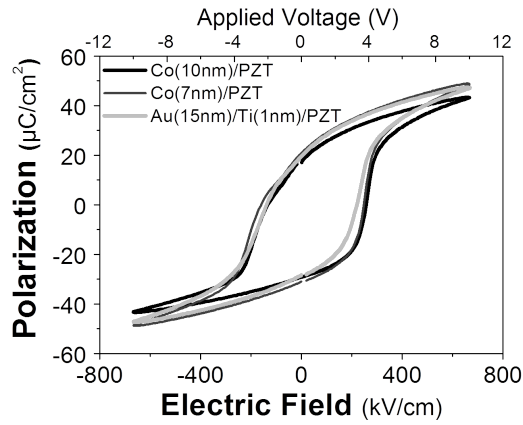


Figure 35: Dynamic P-E loops measured at 2 kHz in Co7nm/PZT, Co10nm/PZT and in a non-magnetic reference Au15nm-Ti1nm/PZT sample

balanced detector differential signal and phase-locked signal) at 2.5 MHz scanning rate constant streaming speeds of about 25 MB/s are required. For this purpose, a high speed solid state drive was implemented in the setup to avoid limited acquisition time due to memory overflow. To minimize the effect of leakage currents in the ferroelectric film, the magnetic top electrode size was restricted to about  $100 \times 100 \mu m^2$ . For this reason the setup was fitted with a digital microscope for precise positioning of the laser focal spot on the micro-patterned electrodes. The measurement time for each frequency was kept under 1s to avoid any sample damaging and temperature drifts.

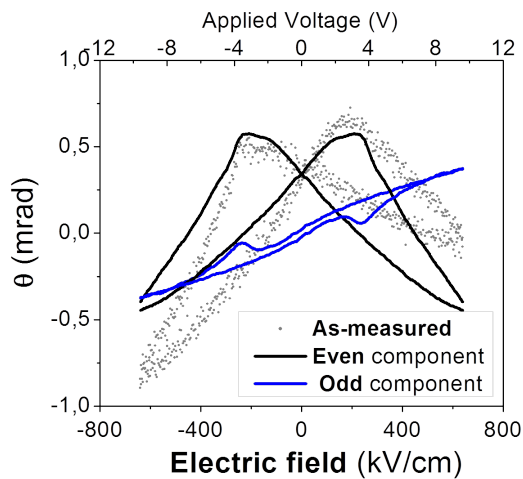


Figure 36: As-measured  $\theta$  rotation angle variation with the electric field  $E$  swept at 3 kHz, measured in Co(7nm)/PZT (scattered dots). The experimental curve has been numerically split into even (black line) and odd (blue line) components of the as-measured signal.

7 nm and 10 nm thick Co films (fig. 32) have been deposited at room temperature by means of molecular beam epitaxy on a 150 nm thick amorphous  $Pb(Zr_{0.2}Ti_{0.8})O_3$  (PZT) layer grown on a thick platinum

base electrode (fig. 33). A gold layer (5 nm) has been deposited as a capping layer to prevent the magnetic films from contamination and to ensure a good electrical contact between the electrodes (Au-Co and Pt). A nonmagnetic top electrode (Au(15nm)/Ti(1nm)) has also been deposited on the same PZT layer. This Au-Ti/PZT system is used as a reference sample to better discriminate between the contributions that have a magneto-optical origin (MEC) from the electro-optical or converse piezoelectric signals coming from the purely ferroelectric properties of PZT.

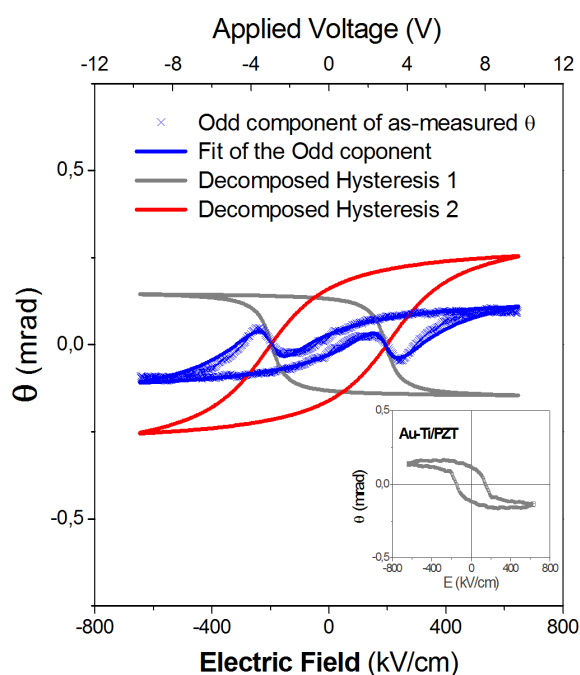


Figure 37: The electric field-dependence of the odd part (blue scattered points) of the Co(7nm)/PZT optical response is further analyzed. A fit based on the analytical model detailed in the text (continuous blue line) and the corresponding split into two components: Hysteresis 1 (Gray) and Hysteresis 2 (Red) are represented. The inset in the lower right corner shows the odd component of the as-measured optical response in the non-magnetic reference samples (gold top electrode).

The magnetic hysteresis loops measured by means of longitudinal Kerr effect (i.e.,  $\theta(H)$  loops) are shown in figure 34. The scale represented on the right-hand side corresponds to the magnetization value as measured by SQUID magnetometer. By measuring zero polar versus significant longitudinal Kerr effect signals, we found that the easy magnetic axis lies in the film plane and the coercive fields are around 25 Oe. The ferroelectric properties of the two magnetic/ferroelectric bilayers as well as the reference sample have been measured using a standard ferroelectric tester (aixACCT) at 2 kHz (fig. 35). A polarization of  $50 \mu\text{C}/\text{cm}^2$  has been measured in all samples. The coexistence

of M-H and P-E hysteretic response in Co/PZT bi-layers demonstrates the multiferroicity of the system at room temperature.

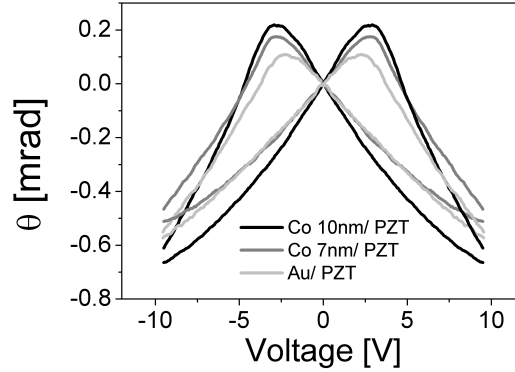


Figure 38: Even-parity birefringence in Co 10nm/ PZT, Co 7nm/ PZT and in the reference sample Au-Ti/ PZT measured in the absence of magnetic fields at electric field sweep frequency of 3 KHz.

The MEC in Co/PZT bi-layers have been first studied under electric field (E) applied perpendicular to the film plane, in the absence of any applied magnetic field. Figure 36 displays the as-measured  $\theta(E)$  rotation angle in Co(7nm)/PZT with E swept at 3 kHz. The measured hysteresis shows a distorted butterfly-like shape in both 7 nm and 10 nm thick Co/PZT (not shown), meaning that the application of E on the Co/PZT bilayers induces a variation of the laser beam polarization in the plane of incidence. Butterfly-like curves are usually ascribed to strain-driven birefringence due to the converse piezoelectric effect on the ferroelectric layers. However, in such cases an even response with the electric field should be expected as the strain response to an applied electric field has an even parity as observed, e.g., in the S-E strain curves. This is in disagreement with the experimental loop displayed in Fig. 36, which shows that the as-measured  $\theta(E)$  is not symmetric. This clearly indicates that contributions other than strain-induced birefringence are present in the system.

In order to obtain a better understanding of the observed optical response, we have implemented a numerical symmetric splitting of the as-measured signal. Thus, the experimental data have been symmetrically split into even (Black curve in Fig. 36) and odd (Blue curve in Fig. 36) contributions. We ascribe the even component (butterfly loop) to the strain-mediated effects mainly attributed to the converse magnetoelectric coupling, while the odd component is related to the surface magnetoelectric coupling. Nevertheless, both, the even and odd components may contain further optical contributions arising from electro-optical and converse piezoelectric responses. Therefore, in the following the odd and even components will be further analyzed to disentangle magneto-optical effects from electro-optical and ferroelastic effects.

The odd contribution of the  $\theta(E)$  signal is decomposed into two hysteresis loops labeled Hysteresis 1 and 2 in Figure 37. These two components were fitted to a combination of  $\tan^{-1}E$  based functions using a first-order approximation to a model originally derived for magnetic hysteresis loops [94]. The implemented model involves four variables: the coercive field  $c$ , the maximum applied field  $m$ , the saturation signal  $s$  and a shape parameter  $q$ . The electric field-dependent hysteresis loop can then be modeled with the following function :

$$f_{i,d}(E, c, s, q) = 2s/\pi \arctan [q \ln ((E + c) b + 1) a + (E + c) q] \quad (22)$$

Where the  $i, d$  index denotes the branch with increasing field and the branch with decreasing field, respectively. The  $a$  and  $b$  factors are written as a function of the coercive field  $c$  and the maximum applied field  $m$  as follows:

$$\begin{aligned} a &= \frac{-2c}{\ln [(1 - b(m - c))(1 + b(m + c))]} \\ b &= \frac{3c + m}{2(m + c)(m - c)} \end{aligned} \quad (23)$$

The model satisfies the central symmetry  $f_d(E) = -f_i(-E)$  and the natural conditions  $f_d(m) = -f_d(-m)$  and  $f_d(c) = 0$ .

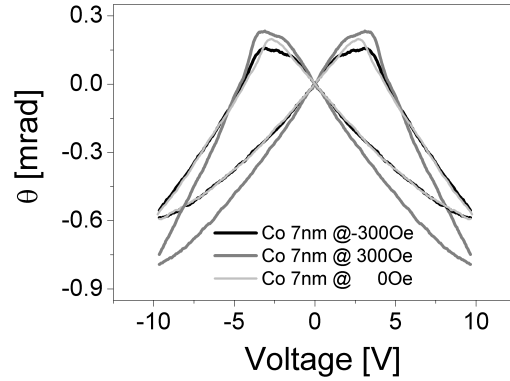
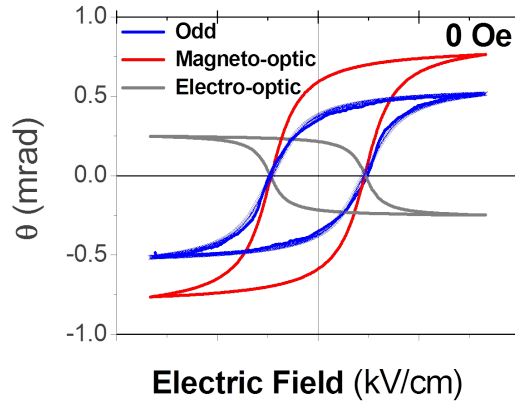
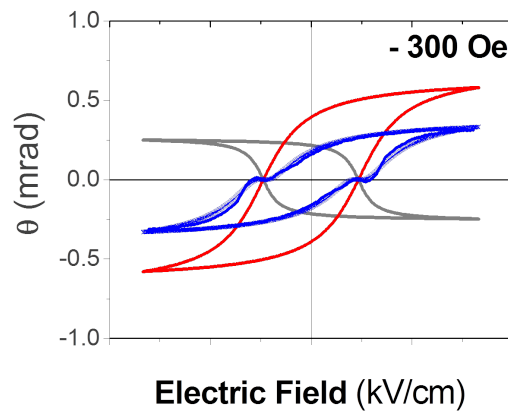


Figure 39: Even-parity birefringence of samples Co 10nm/ PZT and Co 7nm/ PZT measured under magnetic fields  $H = + 300$  Oe and  $H = - 300$  Oe at electric field sweep frequency of 3 KHz.

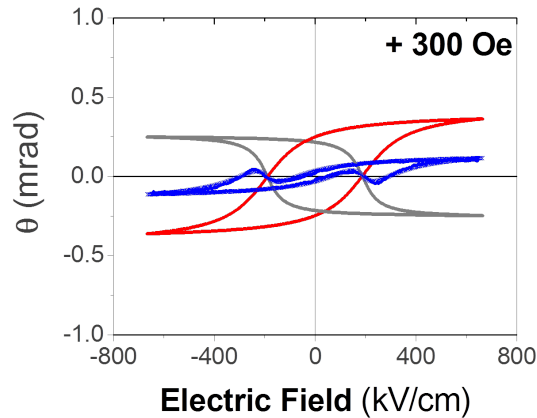
To model a single component hysteresis loop,  $q$  would be the only fitting parameter as  $m$ ,  $s$  and  $c$  factors can be directly extracted from the experimental data. However, in order to separate two superimposed hysteresis loops (e.g., Figure 40), the only directly determined parameter is the sum of signals at saturation. It is therefore important to properly determine the initial fitting parameters by making use of, e.g., of different experimental data input values such as purely ferroelectric contributions (from P-E loops) and purely magnetic contribution (from M-H loops).



(a)  $H = 0$  Oe



(b)  $H = -300$  Oe



(c)  $H = 300$  Oe

Figure 40: Electric-field induced optical response of Co(7nm)/PZT sample at an electric field sweep frequency of 3 kHz, under magnetic fields

This model has been applied to the odd component of the optical signal. One of the two decomposed loops (Hysteresis 1 in Fig. 37) is ascribed to the linear electro-optical effect (Pockels effect [1]) that

is induced by the rotation of the refractive indicatrix accompanying the electric field switching in the **PZT** layer. In order to confirm the consistency of this interpretation, we have measured the optical response of the nonmagnetic reference sample (Au-Ti/**PZT**), in which the odd-in-field component (Figure 37 inset) can only arise from the ferroelectric polarization-driven birefringence. In Figure 37 the inset shows that saturation signal of the odd component in the reference sample ( $\approx 0.25$  mrad) is virtually the same as that obtained through the hysteresis symmetrization model described above (Hysteresis 1). We therefore attribute the odd components referred to as Hysteresis 1 and 2 to respectively, the linear electro-optical E-driven birefringence in **PZT**, and to the magneto-optical response owing to the interface magnetoelectric coupling. More evidence of the magnetoelectric coupling between Co and **PZT** layers will be presented in the following based on the analysis of the  $\theta(E)$  optical response under applied magnetic fields.

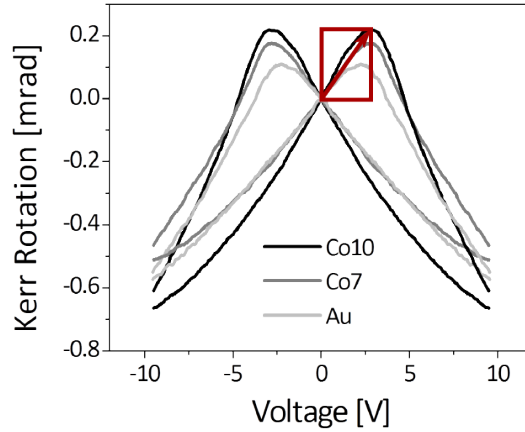


Figure 41: Red arrow demonstrates the magneto-electric factor  $\alpha_{ME} \approx \Delta M/2E_c$  in decomposed strain MEC loop.

For instance, Figure 40 shows the odd components of the optical response  $\theta(E)$  of Co(7nm)/**PZT** measured under different magnetic fields (0 and  $\pm 300$  Oe) applied in the film-plane during the electric field sweep at 3 kHz. We observe that the as-measured loops (Blue curves in Figure 40) change drastically their shapes depending on the magnetic field strength. Assuming that the ferroelectric contribution to the birefringence is unchanged, the strong variation of the hysteretic loops with the magnetic field should be of magneto-optical origin and related to the magnetoelectric coupling. By subtracting the ferroelectric-driven loops (gray curves in Figure 40) from the as measured curves (blue curves in Figure 40), we obtain the magnetoelectric coupling loops plotted as red curves in Figure 40. We clearly see that the saturated values of the magneto-optical loops vary strongly with

the applied magnetic fields. For instance, we see that the saturated value in the absence of H is  $\approx 0.88$  mrad (Figure 40 a), whereas we measured  $\approx 0.75$  mrad for H = - 300 Oe (Figure 40 b) and  $\approx 0.65$  mrad for H = + 300 Oe (Figure 40 c). This observation gives very strong support of our interpretation, so that we can reliably decompose the odd-part of the measured  $\theta(E)$  optical signal into a ferroelectric and a magnetoelectric contribution. Thus, our experiments detect a clear magnetoelectric coupling in Co/PZT bilayers in the absence of applied magnetic field.

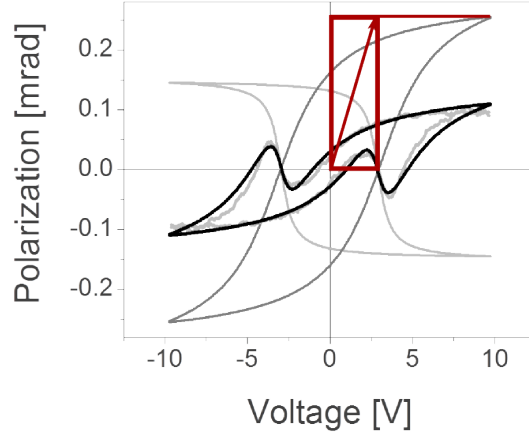


Figure 42: Red arrow demonstrates the magneto-electric factor  $\alpha_{ME} \approx \Delta M/2E_c$  in decomposed surface MEC loop.

Further evidence of the influence of the magnetic field on the E-dependent optical response is given by the analysis of the strain-driven even-parity response as a function of H. Figure 38 displays the even-parity of the as-measured  $\theta(E)$  corresponding to Co(7nm and 10nm)/PZT and to the non-magnetic Au-Ti/PZT reference sample. If there was only a contribution from the converse piezoelectric effect to the loops, roughly identical curves should be measured for all samples. This conclusion is further supported by the observation of a variation with the magnetic field of the even-parity response in Co(7nm and 10nm)/PZT samples to which the signal of the reference sample has been subtracted (Figure 39). We thus ascribe the difference of the odd components in Co/PZT and the reference sample to the additional strain-mediated magnetoelectric contribution originating from the magneto-elastic interaction.



## MAGNETO-ELECTRIC COUPLING STRENGTH IN FREQUENCY SPECTRA

The above detailed results demonstrate the possibility to disentangle the magneto-optical signal related to the MEC from the overall as-measured optical response  $\theta(E)$ . At this point, we are in position to analyze the dependence of the magnitude of the magnetoelectric coupling on the frequency modulation of the electric field. Figures 41, 42, 43 and 44 show the dynamic response of the magneto-optical response related to the magnetoelectric coupling components arising from strain and surface effects as previously discussed. The presented results are measured at room temperature, in the absence of magnetic fields. We reveal a strong decrease of both strain and surface-mediated magneto-optical signal above about 5 kHz until it vanishes at 100 kHz.

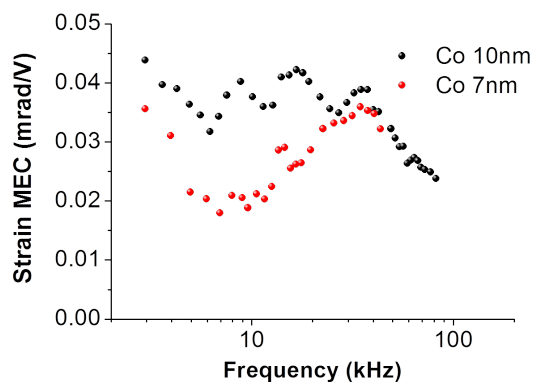


Figure 43: Strain MEC factor  $\alpha_{ME} \approx \Delta M/2E_c$  as a function of frequency of applied electric field.

The magneto-electric (ME) effect can be quantified by the  $\alpha_{ME}$  ME coefficient that is defined by a magnetic induction in response to an applied alternating voltage. In this study, the ME factor is defined by  $\alpha_{ME} \approx \Delta M/2E_c$  expressed in Oe.cm/kV; where  $\Delta M = M_E - M_{E=0}$  and  $E_c$  is the coercive field value. Knowing the correspondence between the magnetization (from SQUID measurements) and the magneto-optical Kerr rotation, the ME coefficient value can be deduced at any frequency value. However, knowing the interface origin of the surface ME coupling, the volume magnetization extracted from SQUID measurements should be converted to a surface magnetization. We thus express the surface mediated ME coupling coefficient in Oe.cm<sup>2</sup>/kV. The strain-mediated MEC and the surface MEC are presented in figures 44 and 43. A stronger strain-induced MEC is found

in the thickest Co/PZT sample and a strong decrease of the MEC with increasing E-frequency is observed in both samples.

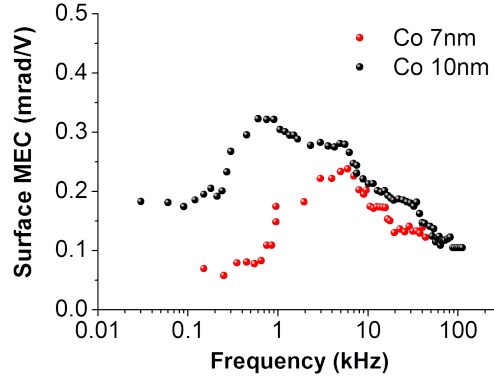


Figure 44: Surface MEC factor  $\alpha_{ME} \approx \Delta M/2E_c$  as a function of frequency of applied electric field.

In conclusion, we report on the MEC in Co/PZT bilayers in the sub-MHz regime by exploring the electric field dependent optical response. We found several contributions to the optical response: strain-driven birefringence from the converse piezoelectric effect in PZT; strain-driven contrast due to magnetostriction in Co, ferroelectric-driven linear electro-optical Pockels effect in PZT and the magneto-optical effect originating from the surface MEC .

Recording interaction of a multiferroic system in spectrum of below MHz frequencies is fast and feasible. Taking advantage of different frequency dependence of the effects interacting with polarization of light we were able to disentangle them and quantify. We separated magneto electric coupling arising from the interface between ferromagnetic cobalt and ferroelectric PZT and the one arising from piezo-strain of PZT.

The shape of the surface magneto-electric coupling in frequency spectrum can be interpreted as a competition of two effects. The linear increase in lower frequencies can be attributed to current leakage in the sample and related dissipation of energy. Faster the switching, less energy dissipates and the coupling strength increases. The exponential decay with higher frequencies can be understood by comparing ferroelectric and ferromagnetic domain wall. Ferroelectric domain walls are known to be much thinner and easier to move around than the thick magnetic domain walls. The ferroelectric domain wall in alternating electric field is an oscillator that is elastically bound to ferromagnetic domain oscillator. The amount of energy transferred from weak oscillator to the stronger one depends clearly on both the strength of the elastic bond between the oscillators and the frequency of oscillations.

The position of the peak in graph [44 on the facing page](#) is therefore mostly determined by the amount of leakage current in the system, the slope on the right side of the spectrum is a function of magneto-electric coupling strength. We can see that there is more leakage through thinner cobalt layer as expected.



## Part IV

### MAGNETO-OPTIC SPECTROSCOPY OF MNP-BASED SYSTEMS

Important adjustments to magneto-optical spectroscopy setup were done in course of this work which extend both its precision and functionality. Automation of spectroscopic measurement reduced measurement time and improved measurement stability. Digital data filtering and integration further improved signal to noise ratio (chapter 3). Thus improved setup could then be used to characterize plasmon enhanced magneto photonic crystals.

Functionality of the setup was also extended to Faraday effect measurement of nanoparticle colloidal dispersions and sensitivity to volume fraction changes of less than  $10^{-6}$  was demonstrated.



## PLASMONIC MAGNETO-PHOTONIC CRYSTALS

The interest of magneto-optical materials for applications in data storage and optical communications has spurred the research on new materials exhibiting large magneto-optical responses at the operating wavelengths. Many strategies of enhancement of much coveted magneto-optical response of various systems have been pursued.

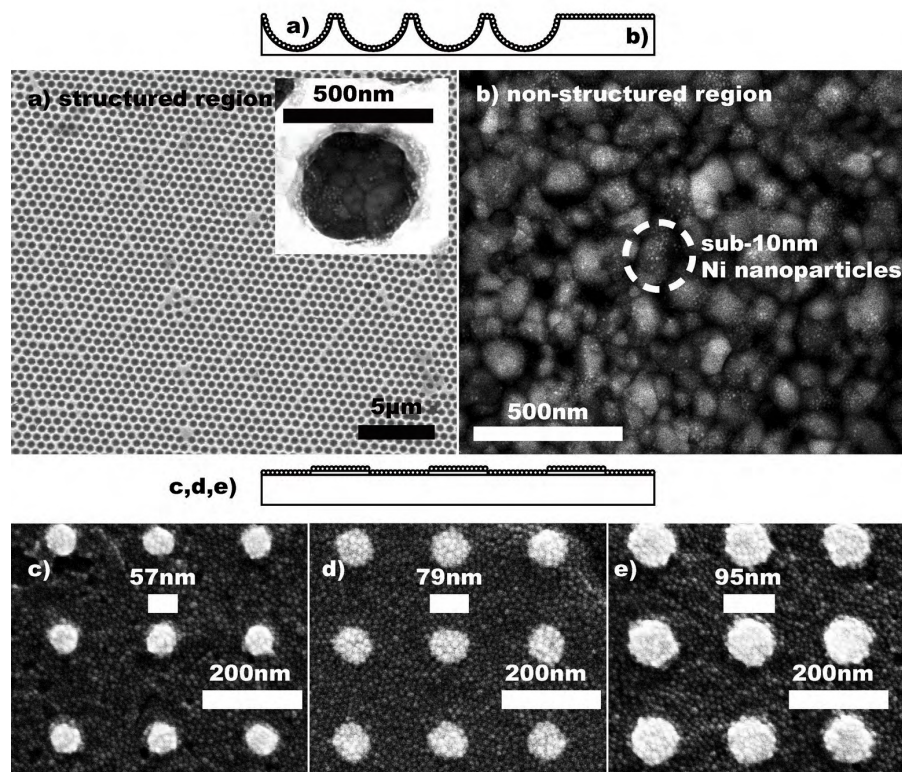


Figure 45: SEM images of the studied structures

- (a) array of gold nanocavities, Inset: detail of one of the cavities, where nickel nanoparticles are observed
- (b) non-structured area (the white circle emphasizes a group of nanoparticles)
- (c-e) SEM images of the nanodisk arrays with diameters  $d \approx 57$ , 79, and 95 nm

Coupling magnetic materials to plasmonic structures is one of them. It dramatically increases the magneto-optical response of the resulting composite architecture. Such optical enhancement has been demonstrated in various systems (Au/Co/Au [95, 96, 97], periodically patterned ferromagnetic films [98, 99, 100, 101, 102], noble metal/ferromagnet structures [103], magnetic nanowires [96] or nanodisk arrays [104, 105]). However, some of its inner workings are not yet well un-

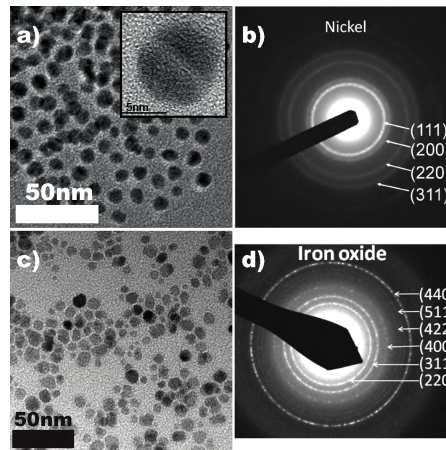


Figure 46: TEM micrographs of used nanoparticles

- (a) nickel nanoparticles, Inset: detail of one nickel nanoparticle
- (b) SAED pattern with the indication of the Miller indices
- (c) iron oxide nanoparticles
- (d) SAED pattern with the indication of the Miller indices

derstood and more detailed knowledge about the fundamental mechanism leading to such improved optical performance is crucial to design better magneto-optical devices. Specifically, contributions of different plasmon triggered effects like reflectance modulation or field intensification were not previously compared and quantified.

To address this issue, we have measured magneto-optical Kerr spectra on corrugated gold/dielectric interfaces with magnetic (nickel and iron oxide) nanoparticles. Enhancement of magneto-optical activity at plasmon frequencies was found to be about an order of magnitude.

Although in previous work evidence has been obtained that the degree of magneto-optical enhancement correlates with the electric field intensification [106], a direct quantitative measurement of both contributions is missing. We decided to fill in the gap using two structures:

- an hexagonal array of spherical truncated gold nanocavities containing a small amount of nickel nanoparticles
- three gold nanodisk arrays with different diameters on an amorphous strontium titanate (STO)/Si(100) substrate, covered with iron oxide nanoparticles

As expected, such materials exhibit a large magneto-optical response at wavelengths where plasmons are excited, by up to an order of magnitude larger than the reference magneto-optical signal. Interestingly, we demonstrate that whereas nanocavities sustain mainly propagating surface plasmons, the nanodisk arrays only localized plasmons are excited. This has allowed us to ascertain whether the different nature of these excitations has an impact on the character of the



observed magneto-optical enhancement. Our results clearly demonstrate that for both kinds of magneto-plasmonic systems the intrinsic polarization conversion efficiency is spectacularly increased, being at least one order of magnitude larger than that from reflectance modulations.

A clarification of used terms is in place:

*Surface Plasmon* is a coherent electron oscillation at metal-dielectric interfaces [107]. The electro-magnetic energy of surface plasmons is strongly confined to the interface. Interface related response may be therefore enormously enhanced, as it is the case of the surface enhanced Raman spectroscopy (SERS) [108, 109].

*Photonic Crystals* are periodically arranged structures engineered at scales comparable to the wavelength of light. For a particular range of wavelengths, these systems exhibit a bandgap for which the electro-magnetic waves cannot propagate in the crystal and also exhibit optical nonlinear effects at photonic band edges [110, 111, 112, 113, 114, 115, 116, 117, 118, 119, 120, 121, 122]. Magnetophotonic crystals have been intensively investigated, in which non-reciprocal optical effects and large magneto-optical responses at stop-band edge frequencies have been reported.

*Photonic/plasmonic Devices* coupled to magnetic materials are taking advantage of combination of all these effects. In large variety of systems, remarkable magneto-optical enhancements have been observed at wavelengths where surface plasmons are excited [107].

### 13.1 SAMPLE PREPARATION

*Gold nanocavity array* was produced via a template self-assembly of polystyrene latex spheres on a gold film on glass, followed by an electrochemical deposition of gold and a final chemical etching of the latex sphere template [123, 124] in the laboratory of A. Fainstein at Centro Atomico Bariloche in Rio Negro, Argentina.

In this process, a solution of polymer spheres fills a thin fluid cell, which is made of a gold-coated glass slide, a clean glass slide, and sidewalls made from a 300  $\mu\text{m}$  thick spacer of Parafilm. The gold slide is coated with cysteamine to reduce the contact angle of the aqueous liquid placed on the surface. This forms a sweeping meniscus tail as the fluid dries, which pulls spheres to the evaporation line where they form a closepacked monolayer domain. After template formation the sample is placed in an electrochemical plating bath. The degree of truncation can be finely controlled by the deposition time. Therefore, very clean, reproducible, and well-defined nanostructured surfaces are obtained over areas on the order of 1  $\text{cm}^2$  [108]. The sample analyzed here was retracted from the solution during the metal deposition in order to achieve a degree of truncation of  $d/2R \approx 0.4$ , where  $d \approx 240$  nm is the Au film thickness while  $2R \approx 600$  nm is the

diameter of the spheres. The resulting structure exhibits a period of  $\approx 650$  nm, being the structural order of the Au nanovoids preserved on large scales up to hundreds of micrometers. Due to the truncated sphere geometry, a top view image of the structure after the chemical deposition (as seen in Figure 45) gives a void diameter of  $\approx 400$  nm, that is, significantly smaller than the sphere diameter in the template.

Nickel nanoparticles with diameters below 10 nm, synthesized by a ligand stabilized solution-phase synthesis (see ref [125] and the description below), were deposited on the Au void surface by vertical immersion on a colloidal dispersion in hexane. The fabrication process also yields a non-structured Au surface outside the area where the spherical void array is defined (Figure 45 b). Optical and magneto-optical characterizations of nanoparticles deposited on this Au flat area were used as reference to analyze the effect of plasmons on the magneto-optical properties of the nanovoid arrays.

*Gold nanodisk arrays* with variable diameter were fabricated by electron-beam lithography on an amorphous STO dielectric layer with thickness  $\approx 60$  nm deposited by pulsed laser deposition at room temperature on p-type doped Si(100) substrates. Three different nanodisk arrays were defined, with diameters  $d \approx 57, 79$  and  $95$  nm, respectively and period  $\approx 200$  nm (see Figure 45 c–e). Iron oxide magnetic nanoparticles with diameters below 10 nm were deposited on the prepared substrates by immersing the nanodisk array templates in a colloidal solution containing the nanoparticles dispersed in hexane. Details on nanoparticle characterization and chemical composition are given below. The fabrication process defines large areas of exposed flat amorphous STO surfaces; on these non-structured regions, free of any Au nanodisk, iron oxide nanoparticles were deposited and their optical and magneto-optical characterizations were used as a reference to analyze the effect of plasmons on the magneto-optical properties of the nanodisk arrays.

### 13.2 NANOPARTICLE SYNTHESIS AND CHARACTERIZATION

Nickel nano-particles were synthesized by high-temperature organometallic decomposition route. The reaction mixture containing 2 mmol (0.514 g) of Ni(acac)<sub>2</sub> precursor, 2 mmol (0.63 mL) oleic acid, 4 mmol (1.8 mL) trioctylphosphine and 14 mL oleylamine solvent was slowly heated up to 130 °C under a flow of high purity argon and magnetic stirring. The mixture was kept at 130 °C for 20 min followed by further heating up to the reflux point (250 °C) and maintained at this temperature for 30 additional minutes [126].

The color of the solution changed from green to dark green and finally to black. After cooling to room temperature, the nanoparticles were precipitated by adding ethanol, followed by centrifugation. The precipitate was dried in an oven (at 70 °C) overnight and weighted.

Finally, the as-synthesized nickel nanoparticles were kept in a hexane dispersion of known concentration. TEM of the Ni nanoparticles shows that they are spherical with an average size of  $8 \pm 1$  nm (Figure 46).

Lattice spacings from the selected area electron diffraction (SAED) patterns (Figure 46) are in good agreement with those of metallic fcc-Ni. For the synthesis of iron oxide nanoparticles, a microwave-assisted sol-gel route was used. Briefly, in a typical reaction, 0.35 mmol of Fe(acac)<sub>3</sub> and 1.05 mmol of oleic acid were dissolved in 1.5 mL anhydrous benzyl alcohol at 60 °C for 5 minutes under magnetic stirring for complete dissolution of the precursors. The mixture had a transparent dark-red color. The precursor solution was further heated in the same microwave reactor to 160 °C, and this temperature was kept stable for 5 min. Then, the solution was automatically cooled down to 50°C by compressed N<sub>2</sub> in approximately 3 minutes. The final suspension was black. The nanoparticles were separated by adding ethanol (40 ml), followed by double centrifugation at 4000 rpm during 20 min.

Finally, the black precipitate was redispersed in 2 ml hexane containing 10 µl oleic acid and used for further characterizations and deposition onto the Au dots. By this procedure, roughly spherical iron oxide nanoparticles with a mean size of  $8.3 \pm 2.5$  nm (see TEM micrographs in Figure 46) were produced. Titration analyses revealed the presence of only 5% of Fe<sub>2+</sub> relative to the total Fe in comparison with an expected 33% for pure magnetite. We thus conclude that the material consists of a mixture of the two phases (magnetite and maghemite) and hereafter will be referred as iron oxide nanoparticles.

### 13.3 METHODS

#### 13.3.0.1 *Optical Reflectivity Spectroscopy*

Optical reflectivity spectroscopy was used for the reflectance measurements. A self-made optical setup consisting of a halogen lamp, a 50× microscope objective, an optical Fourier transform doublet, and a motorized charge-coupled device (CCD) spectrometer allowed us to perform measurements with incident angles from about  $-40^\circ$  to  $40^\circ$  and wavelengths from  $\approx 400$  to 800 nm (see Figure 47).

The light spot can be focused to  $\approx 100$  µm in this setup. The measurements were done with s- and p-polarized incident light, and all of them were referred to the reflectance of a silver mirror to obtain the reflectivity of the samples. The final output generates contour plots that permit the analysis of the dispersion relationship (i.e., frequency versus wavevector or, equivalently, wavelength versus angle of incidence) of light propagating in media.

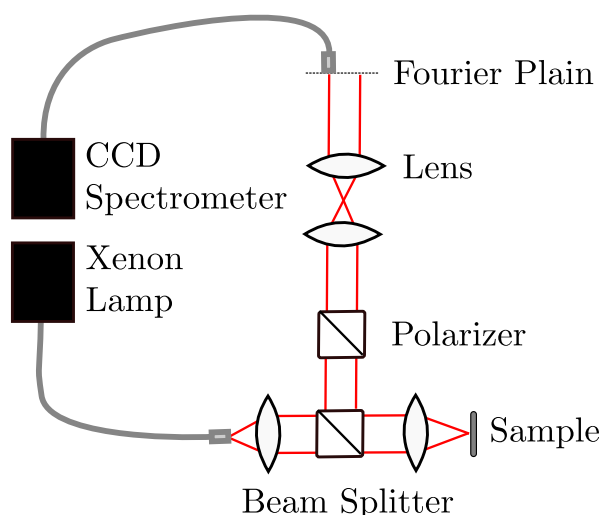


Figure 47: Optical reflectivity spectrometer

### 13.3.0.2 Magneto-Optical Spectroscopy

Kerr rotation ( $\theta$ ) and ellipticity ( $\varepsilon$ ) were obtained at room temperature from the analysis of the polarization of light reflected on samples using equipment introduced in chapter 3.

## 13.4 MORPHOLOGY

After vertical immersion of the Au void and nanodisk arrays in colloidal dispersions of magnetic nanoparticles in hexane, we carried out scanning electron microscopy (SEM) to characterize the surface morphology. Since the individual nanoparticles were detectable by direct visual inspection of the SEM images (see Figure 45), we exploited the latter to assess the degree of nanoparticle coating on these structures.

For instance, Figure 45 a and b revealed the presence of individual Ni nanoparticles on the Au void array, as appreciated in the inset of Figure 45 a (displaying a zoom of a single Au cavity) as well as in Figure 45 b, where one group of nanoparticles is emphasized by a dashed circle. The direct visual inspection of these images allowed us to estimate that inside the void cavities the surface nanoparticle density was around  $10^{-3}$  nanoparticles/nm<sup>2</sup>, equivalent to a surface coverage of  $\approx 6\%$ .

The distribution of the nanoparticles was found to be quite uniform (less than 20% variation from cavity to cavity). Outside the cavities of the Au void array, on the non-structured area (see Figure 45 b), the nanoparticle surface density appeared to be slightly higher, around  $2 \times 10^{-3}$  nanoparticles/nm<sup>2</sup>, equivalent to a surface coverage  $\approx 12\%$ .

SEM images of the Au nanodisk arrays also allowed identifying the presence of the individual nanoparticles (Figure 45 c–e). An inspection of these figures immediately reveals a significantly larger and

uniform nanoparticle surface density. Indeed, with independence of the nanodisk size, the iron oxide nanoparticle surface density was estimated to be around  $8 \times 10^{-3}$  nanoparticles/nm<sup>2</sup> and surface coverage  $\approx 50\%$ , significantly larger than the values found in the Au voids.

### 13.5 REFLECTOMETRY

Figures 48 and 50 display the contour plots of the reflectance spectra of the Au void and nanodisk arrays, respectively, measured in the range of wavelengths  $\lambda \approx 400\text{--}800$  nm for both s- and p- linearly polarized light. From these experiments, we obtained the absolute values of the diagonal Fresnel reflections coefficients  $|r_{ss}|$  and  $|r_{pp}|$  that give the relative intensities of s- and p-polarized lights between incident and reflected waves.

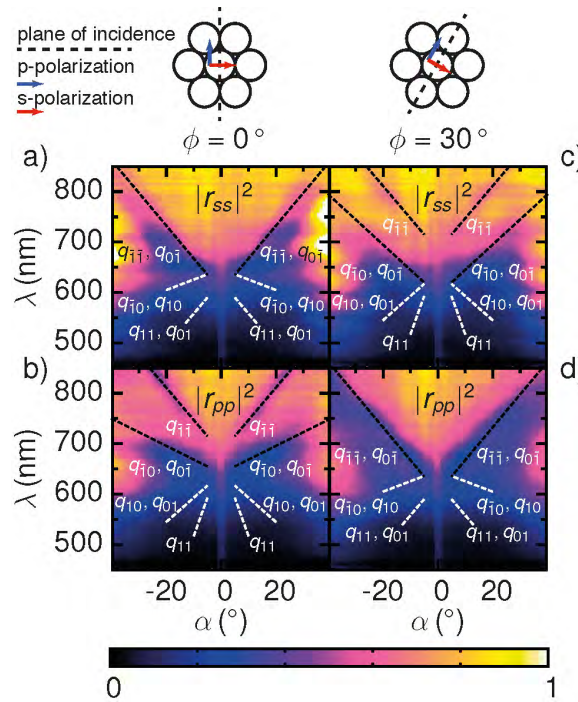


Figure 48: Reflectometry of nanocavities

#### 13.5.1 Au Void Array

The reflectance spectra of the Au void surface coated with nickel nanoparticles reveal the presence of several dispersive absorption lines that are dependent on both the light polarization and the relative orientation of the plane of incidence with respect to the void geometry (see Figure 48 and the sketch therein). Along these dispersive bands, the absorption peak is located at wavelengths that depend strongly on the angle of incidence  $\alpha$  (and wavevector), indicating the excitation of delocalized Bragg surface plasmon modes [127, 128, 129].

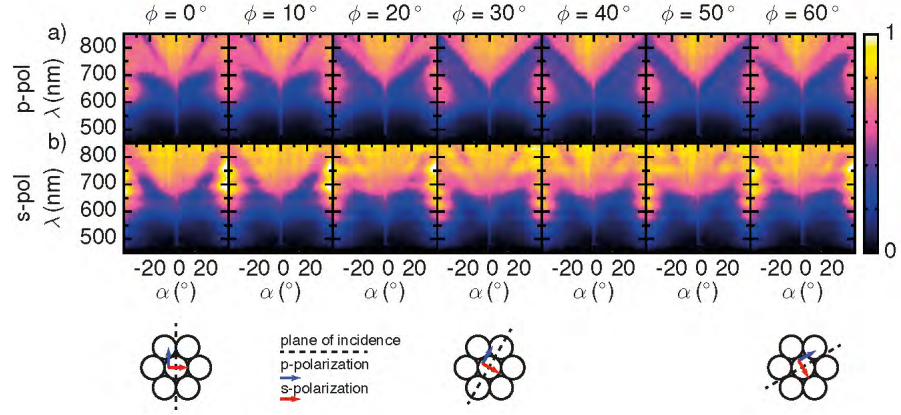


Figure 49: Angular optical reflection spectrometry

We note that although for  $d/2R \approx 0.4$ , a Mie mode ( $^1P^+$ ) is expected to be excited at wavelength  $\lambda \approx 650$  nm, its resonance is significantly weaker than that of Bragg modes [129], and this may be the reason for which its excitation is not apparent in the spectra (Figure 48). Another possible explanation is that a random distribution of nanoparticles inside the Au voids can induce fluctuations of the Mie resonances from cavity to cavity, smearing out the localized resonance when probed with a large light spot ( $\approx 100$   $\mu\text{m}$ ). Our measurements on the Au void surface indicate that Bragg modes are observed for both s- and p-polarized incident light, in agreement with other reports [127].

Interestingly, the delocalized character of these collective excitations is further confirmed by inspection of the reflectance contour maps recorded at different azimuth angles. In particular, the dispersion relation is slightly modified as the plane of incidence of light is rotated around an axis normal to the sample surface, being the spectra periodic with azimuth period  $\Delta\phi = 60^\circ$ , as expected from the void hexagonal packing (Figure 49).

We note also that a global inspection of all the spectra measured at different azimuth angles shows that similar absorption bands are excited either by incident s- or p-polarized light, although for each particular angle the spectra may differ significantly. Thus, the contour plots measured with p-polarized light at azimuth angles  $\phi = 20^\circ - 40^\circ$  are similar to those obtained for s-polarized light with azimuth angles  $\phi = 0^\circ$  or  $\phi = 60^\circ$ , and vice versa plots measured with s-polarized light at azimuth angles  $\phi = 20^\circ - 40^\circ$  are somewhat similar to those obtained for p-polarized at angles  $\phi = 0^\circ$  or  $\phi = 60^\circ$ .

This feature can be understood in terms of the orientation of light polarization with respect to the void geometry, making the coupling to plasmons of s-(p-)polarized vector fields for one particular direction of the plane of incidence similar to the coupling to plasmons of p-(s-)polarized vector fields with a plane of incidence rotated  $\Delta\phi = 30^\circ$  (see the sketch in Figure 49 and Figure 48).



Bragg plasmons propagating in a close-packed two-dimensional structure of Au void arrays have been modeled in previous experimental and theoretical studies [127]. Assuming that light is scattered by planes spaced by  $[3/4(m\vec{a} + n\vec{b})]^{1/2}$ , where  $(m, n)$  are integers and  $(\vec{a}, \vec{b})$  are the two lattice vectors, the Bragg plasmon energies can be obtained as a function of the incident angle.

We used these data to identify the dispersive absorption bands of Figure 48 with the different Bragg mode wavevectors  $q_{mn}$  [127]. Figure 48 a and b shows the spectra recorded with the plane of incidence oriented along the direction with azimuth  $\phi = 0^\circ$  (see the sketch in this figure), for s- and p-polarized light, respectively. For p-polarized light, we associate the lower energy dispersive band (longer wavelengths) to the  $q_{11}$  mode, while we relate the highest observed band to the  $q_{10}$  and  $q_{01}$  modes (Figure 48 b). Propagating  $q_{10}$ ,  $q_{01}$  and  $q_{11}$  modes may still be present, albeit their presence can be damped due to the strong absorption for wavelengths below  $\lambda \approx 500$  nm that is related to interband transitions of d-electrons in gold [130, 131].

For s-polarized light, the strong absorption band is assigned to the  $q_{11}$ ,  $q_{01}$  modes, while other modes ( $q_{10}$ ,  $q_{10}$  and  $q_{11}$ ,  $q_{01}$ ) may be also damped at shorter wavelengths (Figure 48 a). The spectra recorded with the plane of incidence oriented along  $\phi = 30^\circ$  exhibit similar plasmonic excitations, although the assigned modes for s- and p-polarization are now interchanged with respect to  $\phi = 0^\circ$ , in agreement with the cross-correlation of s- and p-spectra with periodicity  $\Delta\phi = 30^\circ$  discussed above.

### 13.5.2 Au Nanodisk Arrays

The reflectance contour plots recorded for s-polarized light on the Au nanodisk arrays are shown in Figure 50. We see that non-dispersive reflection maxima are located at wavelengths  $\lambda \approx 660$  nm (Figure 50 a, d  $\approx 57$  nm) and  $\lambda \approx 710$ – $720$  nm (Figure 50 b, c, d  $\approx 79, 95$  nm), which correspond to resonantly enhanced scattering cross section for wavelengths at which localized plasmons are excited [107].

Note that the observed wavelength resonances are red-shifted with increasing diameter, as expected [107]. The localized nature of plasmons excited in the nanodisks is emphasized by the fact that, contrary to the behavior observed in the Au void template, the displayed reflection maxima are nondispersive (Figure 48) and the reflection spectra are essentially insensitive to light polarization, either s or p (not shown). We note also that the distance between nanodisk centers, being  $\approx 200$  nm, is probably too large for the interaction of the localized plasmons, in agreement with the expected separation needed for plasmon hybridization which should be in the order of a few tens of nanometers [132, 133, 129].

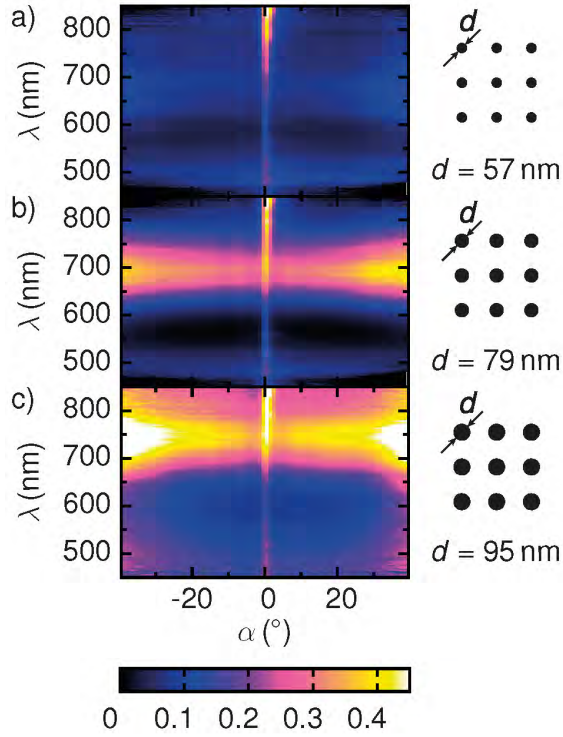


Figure 50: Nanodots reflectometry

### 13.6 MAGNETO-OPTICAL SPECTROSCOPY

The effects of an arbitrary optical system on the polarization of light reflected from its surface are governed by the diagonal Fresnel reflection coefficients  $r_{ss}$  and  $r_{pp}$  that describe the changes of amplitude and phase for s- and p-polarized light, respectively, as well as the off-diagonal  $r_{sp}$  and  $r_{ps}$  coefficients that reflect the conversion between s- and p-polarizations. After reflection on a magnetic surface, an orthogonal polarization appears as a consequence of the magneto-optical activity. For instance, for incident p-polarized light, the reflected wave acquires an additional small s-polarization and, conversely, a small p-polarization comes up from reflection of an incident s-polarized light. Thus, the relative intensity and phase of the polarizations of the incident and reflected waves gives way to a magneto-optical activity described in terms of rotation and ellipticity

The understanding of the microscopic mechanisms that govern these magneto-optical effects are based on the knowledge of the electronic structure and electron wave functions in solids, and the transitions of electrons between the different bands induced by electromagnetic waves [134, 114].

For the particular case of the polar Kerr magneto-optical configuration used in our experiments, the complex Kerr effect is shown to be



related to the diagonal ( $\epsilon_{xx}$ ) and off-diagonal ( $\epsilon_{xy}$ ) permittivity tensor components through  $\chi = \theta + i\epsilon \approx \sqrt{\epsilon_{xx}} \frac{-\epsilon_{xy}}{\epsilon_{xx}-1}$ .

Thus, we see that the appearance of off-diagonal permittivity components is an essential ingredient for the emergence of magneto-optical activity. An electric field intensification and the ensuing increase of density of optical modes [135] occurring in the vicinity of surfaces where plasmons are excited might provide a natural mechanism to amplify the magneto-optical activity.

One way to do this is to place the magneto-optical material at small regions where plasmons are excited, as is the case of the patterned metal surfaces discussed here, where the electromagnetic fields are strongly confined around the metal/dielectric interfaces and increasing hugely the electromagnetic density of states [107].

Alternatively, the intensification of the magneto-optical activity may be also originated by a decrease of the diagonal coefficients  $r_{ss}$  and  $r_{pp}$ , providing an independent pathway toward magneto-optical enhancement [96, 136].

As described in the following, the combination of optical and magneto-optical spectroscopy has allowed us to quantify the contribution of both factors. We find that the enhancement of the magneto-optical activity in the plasmonic structures here presented is essentially due to an intrinsic increase of the off-diagonal coefficients terms  $r_{sp}$  and  $r_{ps}$ . Before proceeding, we note that the Au void and nanodisk arrays did not exhibit magneto-optical activity before the impregnation with the magnetic nanoparticles.

### 13.6.1 *Magneto-Optical Spectra of the Au Void Surface Infiltrated with Nickel Nanoparticles.*

The rotation ( $\theta$ ) and ellipticity ( $\epsilon$ ) hysteresis loops were recorded as a function of the light wavelength within  $\lambda \approx 390\text{--}850$  nm with a step resolution of  $\Delta\lambda = 1$  nm for magnetic fields  $|H| \leq 15$  kOe. The data were measured in polar Kerr configuration with light incident at  $\alpha \approx 9.5^\circ$  from the normal to the sample surface and the plane of incidence of the light was along the azimuth angle  $\phi = 30^\circ$ .

Figure 51 a and d shows the ellipticity and rotation loops measured with incident s-polarized light at the selected wavelengths indicated in the figure, whereas Figure 51 g and j displays the magneto-optical data for p-polarization. All these figures show the curves recorded with the beam light focused inside the structured area (Au voids, dashed lines) as well as outside (non-structured Au surface, full lines). The S-like shape of the loops and the negligible coercive field are typical of superparamagnetic behavior, representative of aggregates of magnetic nanoparticles, with saturation field  $H \approx 10$  kOe. Remarkably, at the selected wavelengths, the magnitude of the magneto-optical hysteresis loops recorded inside the voids are of

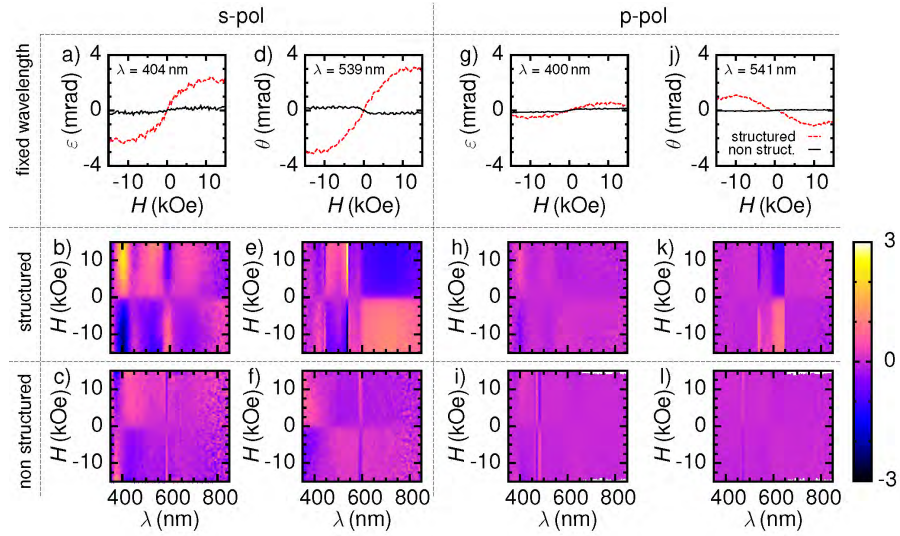


Figure 51: Comparison of magneto-optical enhancement on nanodisks

the order of a few mrad, in contrast to the values measured in the non-structured area ( $\sim 0.1$  mrad); see Figure 51 a, d, g, and j.

This large magneto-optical enhancement, of more than 1 order of magnitude for some wavelengths, comes up in spite of the nanoparticle coverage of the non-structured area being roughly two times larger than that of the Au voids. This clearly indicates that the magneto-optical response of nanoparticles deposited on the structured Au surface is strongly modified with respect to the response of the same nanoparticles on the non-structured area. This conclusion is further confirmed by inspecting the magneto-optical contour plots obtained by mapping the rotation and ellipticity as a function of wavelength and magnetic field ( $|H| \leq 15$  kOe). The contour plots were measured with light incident inside the Au void array for s-polarized light (ellipticity and rotation in Figure 51 b and e, respectively) and for p-polarized light (ellipticity and rotation in Figure 51 h and k, respectively).

Similar plots were also obtained for the non-structured surface (Figure 51 c, f, i, l). We observe that while the plots corresponding to the non-structured areas appear relatively featureless on the plotted scale, with rotation/ellipticity values below  $\approx 0.5$  mrad, the plots corresponding to the voids display relatively narrow spectral regions where the magneto-optical response is remarkably intensified, with values up to  $\approx 3$  mrad. For instance, for s-polarized incident light the ellipticity is strongly peaked at around  $\lambda \approx 400, 550,$  and  $590$  nm (Figure 51 b), whereas the rotation is especially intensive at  $\lambda \approx 540$  nm. On the other hand, for p-polarized light, the ellipticity is faintly intensified around  $\lambda \approx 400$  nm, whereas the rotation is significantly enhanced at  $\lambda \approx 540$  and  $625$  nm.

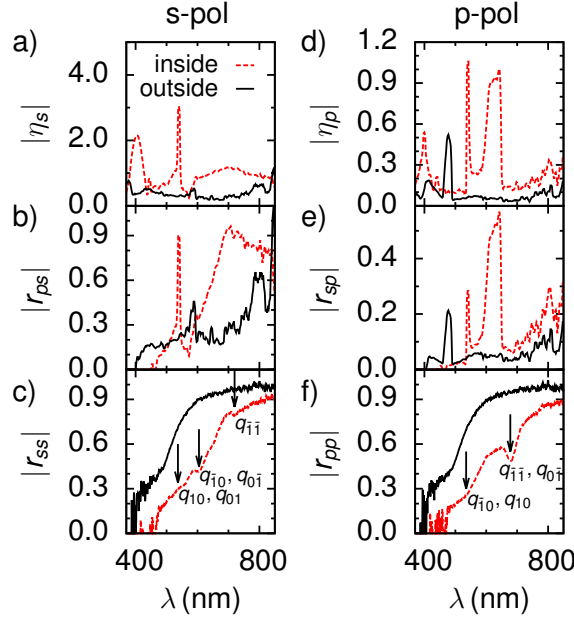


Figure 52: Magneto-optical enhancement in Fresnel coefficients

The magneto-optical responses are then enhanced around spectral regions that are close to the wavelengths where plasmons are excited for light incident at  $\alpha \approx 9.5^\circ$  (Figure 48). To further investigate the connection between magneto-optics and plasmonics, we extracted from the measurements of the rotation and ellipticity the absolute value of the Kerr effect

$$|\eta_{s,p}| = \sqrt{\theta_{s,p}^2 + \epsilon_{s,p}^2}$$

for s- and p-polarized light, shown in Figure 52 a and d, respectively. Since the values of the diagonal reflection coefficients  $|r_{ss}|$  and  $|r_{pp}|$  are directly drawn from the reflectance spectra of Figure 48, we were in position to obtain the off-diagonal coefficients  $|r_{sp}|$  and  $|r_{ps}|$ , as  $|r_{sp,ps}| = |\eta_{s,p}| \times |r_{ss,pp}|$ . The values of  $|\eta_s|$ ,  $|r_{sp}|$ , and  $|r_{ss}|$  for s-polarized light are shown in Figure 52 a–c, whereas  $|\eta_p|$ ,  $|r_{ps}|$ , and  $|r_{pp}|$  for p-polarized light are displayed in Figure 52 d–f. All data in Figure 52 are plotted for light focused both inside and outside the structured area.

The different Bragg mode wavelengths are inferred by the appearance of dips in the reflectance spectra, and are indicated by arrows in the curves of  $|r_{ss}|$  (Figure 52 c) and  $|r_{pp}|$  (Figure 52 f), which are obtained from cuts made at an angle of incidence of  $\alpha = 9.5^\circ$  of the reflectance spectra of Figure 48 c and d, respectively. We observe that the Kerr angles  $|\eta_s|$ ,  $|\eta_p|$  and the off-diagonal coefficients  $|r_{sp}|$ ,  $|r_{ps}|$  are particularly enhanced in the void areas with respect to the non-structured regions for a certain range of wavelengths.

Thus, for s-polarized light, two main regions are identified for which the patterned area exhibits  $|\eta_s|$  and  $|r_{sp}|$  that are up to an order of magnitude larger than in the non patterned surface. One is located around a narrow region around  $\lambda \approx 540$  nm, for which the Bragg modes  $q_{10}$ ,  $q_{01}$  are excited. These modes, although predicted by the theory [127], are hardly identified in the reflectance spectra (Figures 48 c and 52 c), but Figure 52 a and b demonstrates that they have a conspicuous effect on the magneto-optical properties. A second region is found within a broad region  $\lambda \approx 600\text{--}800$  nm, centered at  $\lambda \approx 700$  nm, which is relatively close to the wavelengths at which the  $q_{11}$  Bragg modes are excited. We note that  $q_{10}, q_{01}$  modes seem to have a less relevant influence on the magneto-optical activity. Similarly, for p-polarized light,  $|\eta_p|$  and  $|r_{sp}|$  inside the void surface are magnified by around of order of magnitude with respect to the non-structured region for wavelengths centered on a narrow region  $\lambda \approx 540$  nm.

A second broader region is identified around 630 nm. Although it might be associated to Bragg modes  $q_{11}$ ,  $q_{01}$  and  $q_{10}$ ,  $q_{10}$ , one cannot exclude that localized Mie-like resonances play a role on the magneto-optical enhancement around these broader spectral regions. We note that these localized resonances might be smeared out when observed using a large light spot, but they may be present at each individual cavity, with resonance frequencies fluctuating because of random distributions of nanoparticles inside the voids.

### 13.6.2 *Magneto-Optical Spectra of the Au Nanodisk Arrays Infiltrated with Iron Oxide Nanoparticles*

An analogous magneto-optical spectral study was carried out on the Au nanodisk arrays infiltrated with iron oxide nanoparticles. Figure 54 a and f shows the ellipticity and rotation hysteresis loops, respectively, measured for s-polarized light focused on the three different nanodisk patterns ( $d \approx 57, 79, 95$  nm) as well as on nanoparticles deposited on the non-structured surface. We observe that, as before, the shape of the hysteresis loops indicates a superparamagnetic behavior of the infiltrated nanoparticles. The downturn in the magnitude of the hysteresis loops for fields  $|H| \geq 4$  kOe is related to a diamagnetic magneto-optical contribution coming from the STO substrate underneath the nanoparticles, that at high enough fields, above the magnetization saturation, can overcome the signal from nanoparticles. This is the expected behavior from the diamagnetic response of STO. This contribution can be removed to obtain the contributions of nanoparticles alone. Interestingly, the magneto-optical activity of the nanoparticles deposited on the patterned areas reaches values of up to  $\sim 6$  mrad, whereas nanoparticles on the non-patterned area exhibit much lower ellipticity/rotation, in the order of  $\sim 0.8$  mrad. As before,

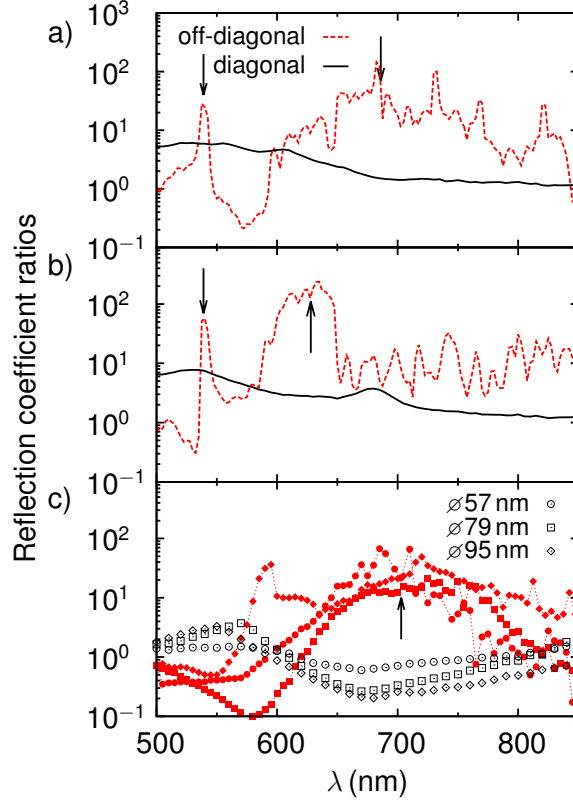


Figure 53: Diagonal and off-diagonal contributions to magneto-optical enhancement

this is a clear indication that the magneto-optical spectra are substantially modified when nanoparticles are deposited on the nanostructured metallic surfaces. Contour plots for the ellipticity (Figure 54 b–e) and rotation (Figure 54 g–j) were obtained by mapping the magneto-optical activity as a function of wavelength ( $\lambda \approx 390\text{--}850$  nm) and magnetic field ( $|H| \leq 7$  kOe). Again, this allowed us to get an overall picture of the effect on the magneto-optical spectra of nanostructuring the metal/dielectric surface. In particular, we again observed that the magneto-optical activity was significantly enhanced around relatively narrow spectral regions centered at wavelengths in the vicinity of the localized plasmon resonances.

In contrast, for light incident on the non-structured area, the spectra were quite featureless when plotted on the same scale. For instance, for nanodisks with diameter  $d \approx 57$  nm, the ellipticity was especially intensified around  $\lambda \approx 670$  nm (Figure 54 b), while the rotation was peaked at different wavelengths around  $\lambda \approx 400, 470, 610,$  and  $725$  nm (Figure 54 g), with values that reach up to  $\approx 6$  mrad. For  $d \approx 79$  nm, the ellipticity appears particularly intensified around  $\lambda \approx 675$  and  $725$  nm (Figure 54 c), whereas the rotation is faintly magnified around  $\lambda \approx 725$  nm (Figure 54 h). Finally, for  $d \approx 95$  nm, the ellipticity appears to be increased at  $\lambda \approx 520, 650,$  and  $725$  nm (Figure 54 d), with the

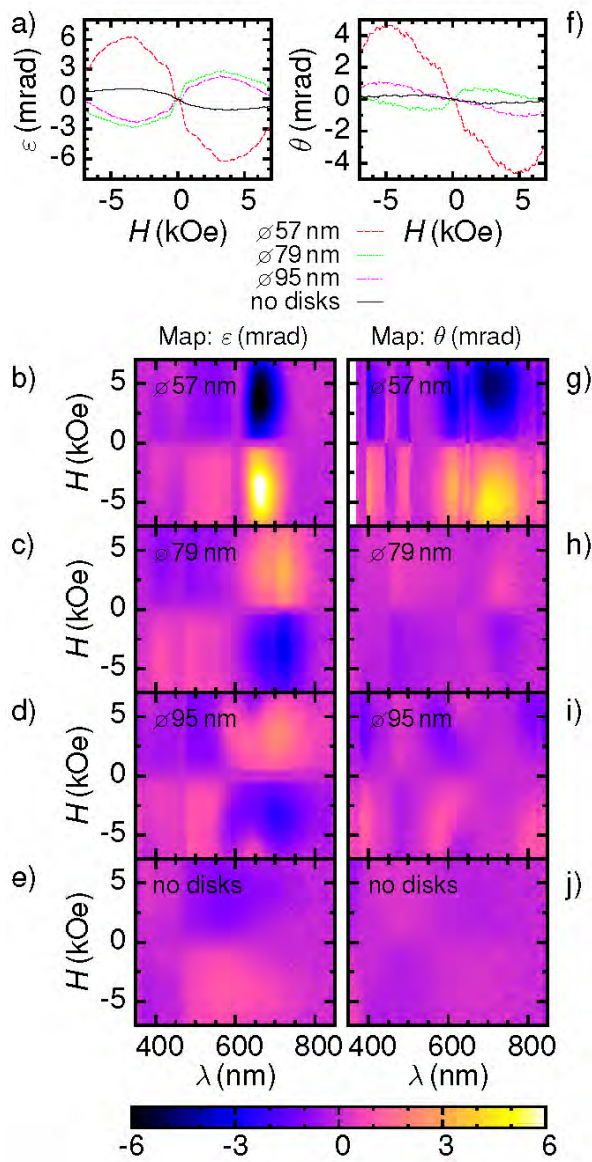


Figure 54: Magneto-optical spectra of nanodisk arrays



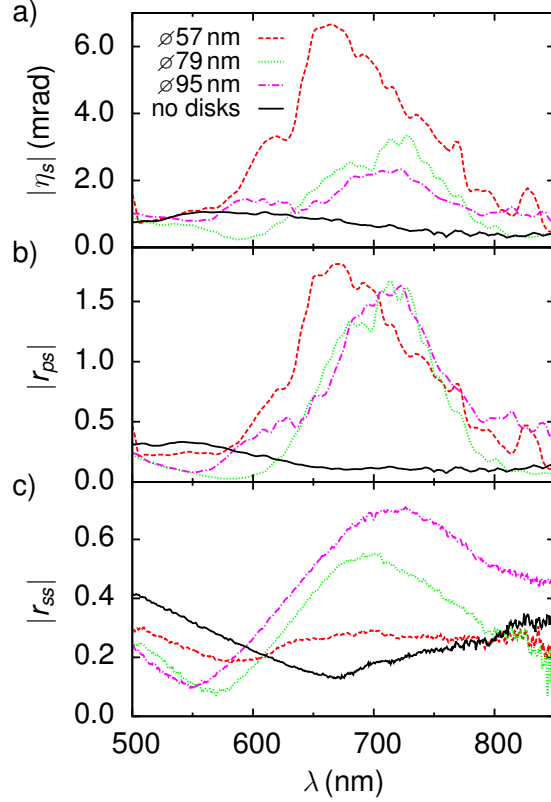


Figure 55: Fresnell coefficients spectra

rotation slightly enhanced at  $\lambda \approx 390$  and  $590$  nm (Figure 54 i). As discussed previously for the Au void array, the relationship between the magneto-optical spectra and plasmonics can be better appreciated by plotting  $|\eta_{s,p}| = \sqrt{\theta_{s,p}^2 + \epsilon_{s,p}^2} |r_{sp}|$  and  $|r_{ss}|$  (see Figure 55).

We observe that the Kerr angle is strongly peaked at wavelengths  $\lambda \approx 720$  nm for disks  $d \approx 79$  and  $95$  nm, and  $\lambda \approx 670$  nm for  $d \approx 57$  nm, with maximum values that reach up to  $|\eta_s| \approx 6.7$  mrad (Figure 55 a). Note that in the non-structured region  $|\eta_s|$  displays significantly lower values all over the spectrum, and it does not exhibit any peak within  $\lambda \approx 600$ – $800$  nm, with values  $|\eta_s| \leq 0.8$  mrad over that spectral region. The behavior of  $|r_{sp}|$  is quite similar that of to  $|\eta_s|$ , with peak values within  $\lambda \approx 600$ – $800$  nm for the nanodisk area, and being quite flat over that region for the non-structured surface (Figure 55 b). When compared to the reflectance  $|r_{ss}|$  spectra, we observe that the maxima of  $|\eta_s|$  and  $|r_{sp}|$  appear to be in the vicinity of maxima for  $|r_{ss}|$  (Figure 55 c), in agreement with the resonantly enhanced light scattering cross section for localized plasmons. Thus, we demonstrate that the coupling of the magneto-optical activity of magnetic nanoparticles with localized plasmon excitations of the Au nanodisk arrays gives way to a significant modification of

the magneto-optical spectral response and to an enhancement of the magneto-optical activity.

### 13.7 ORIGIN OF MAGNETO-OPTICAL ENHANCEMENTS

Absolute values of the Kerr effect are given by  $|\eta_s| = r_{sp}/r_{ss}$ ,  $|\eta_p| = r_{ps}/r_{pp}$ , for s- and p-polarized light, respectively. Thus, with the correlation between magneto-optical properties and plasmon excitations being established, a question arises to which degree the observed magneto-optical enhancements of  $|\eta_s|$  and  $|\eta_p|$  are due to an intensification of the off-diagonal reflectance  $r_{sp}$ ,  $r_{ps}$  coefficients, associated to the plasmon-assisted electric field enhancement, or to a modification of the spectral response of the diagonal  $|r_{ss}|$  and  $|r_{pp}|$  terms.

To answer this question, we have calculated from the experimental values the ratios

$$\frac{|\eta_s|_{\text{pattern}}}{|\eta_s|_{\text{flat}}} = \frac{|r_{sp}|_{\text{pattern}}}{|r_{sp}|_{\text{flat}}} \frac{|r_{ss}|_{\text{flat}}}{|r_{ss}|_{\text{pattern}}}$$

$$\frac{|\eta_p|_{\text{pattern}}}{|\eta_p|_{\text{flat}}} = \frac{|r_{ps}|_{\text{pattern}}}{|r_{ps}|_{\text{flat}}} \frac{|r_{pp}|_{\text{flat}}}{|r_{pp}|_{\text{pattern}}}$$

where the subindices pattern and flat correspond to the spectra recorded in structured (void or nanodisk arrays) and flat non-structured surfaces, respectively.

Thus, we are in a position to find out the separate contributions of the diagonal  $\frac{|r_{pp}|_{\text{flat}}}{|r_{pp}|_{\text{pattern}}}$  and off-diagonal  $\frac{|r_{ps}|_{\text{pattern}}}{|r_{ps}|_{\text{flat}}}$  terms to the magneto-optical enhancements observed in Figure 52 a,d and 55 a.

In Figure 10, we have plotted the ratios of the off-diagonal and diagonal coefficients for the Au void array, measured for s- (Figure 53 a) and p- (Figure 53 b) polarizations, and for the three nanodisk arrays (Figure 53 c). The regions with enhanced magneto-optical activity are identified in these figures by arrows. An inspection of these data reveals immediately that the magneto-optical enhancement is determined almost entirely by an extraordinary increase of the off-diagonal reflectance coefficients, whereas the diagonal terms play a minor role.

For instance, for the Au voids, the coefficients  $|r_{sp}|$  and  $|r_{ps}|$  are enhanced by up to a factor  $\approx 50$  in the structured regions, whereas the diagonal coefficients  $|r_{ss}|$  and  $|r_{pp}|$  are increased by a factor  $\approx 1-5$  in the relevant spectral regions; see Figure 53 a and b. The increase of  $|r_{sp}|$  is still more spectacular in the nanodisk arrays, where for the relevant region enhancement factors of about 3 orders of magnitude are found, whereas the ratio of  $|r_{ss}|$  remains close to the unity or is even suppressed in the region where plasmons are excited. We can



conclude, then, that the magneto-optical enhancement of nanoparticles deposited on nanostructured metal/dielectric surfaces is almost entirely due to an outstanding increase of the conversion rate between orthogonal polarizations, rather than by a modification of the reflectance.

### 13.8 CONCLUSIONS

We found that the magneto-optical spectra of magnetic nanoparticles inside nanostructured metal/dielectric surfaces are dramatically modified compared to the spectra of nanoparticles randomly distributed on non-structured flat surfaces. In particular, the magneto-optical activity is substantially increased for wavelengths at which surface plasmons, either localized resonances or extended Bragg modes, are excited on the nanostructured metal/dielectric interfaces. We have achieved a quantitative evaluation of the contributions of both intrinsic polarization conversion efficiency and reflectance modulations to the observed magneto-optical enhancement.

Interestingly, we have demonstrated that plasmon-induced field enhancement is responsible for the spectacular increase of the intrinsic polarization conversion efficiency, which is at least 1 order of magnitude larger than that from reflectance modulations, thus shedding light on the fundamental principles for the observed optical response. Our results prove the potential of surface plasmons to generate large magneto-optical signal enhancements at specific wavelengths and to design promising strategies to modify the spectral optical responses of magneto-optical materials. Hybrid systems composed of magnetic nanoparticles with corrugated metal/dielectric surfaces offer a promising strategy for new applications, where very small changes of polarization of light associated to magneto-optical effects can be exploited for sensing applications. This approach offers a high potential for sensing, especially for wavelengths that match the plasmon resonances with targeted patterned surfaces, giving high sensitivity even for low coverage of nanoparticles.



## FARADAY SPECTROSCOPY OF DILUTED MAGNETIC LIQUIDS

---

The interaction of polarized light with metal clusters and nanoparticles embedded in dielectric hosts has been a recurrent topic during the last three decades. [137, 138, 139, 140, 141, 142, 143, 144, 145, 146, 147, 148, 149, 150, 151]

One of the most investigated aspects in this field has been the enhanced magneto-optic response mediated by the excitation of localized surface plasmon resonance (LSPR)s. [139, 138, 144, 146, 150, 152] By and large, the research in such composite metal/dielectric composites has been essentially focused on the magnification of the optical properties of the metal nanostructures, leaving the properties of the dielectric host in a second plane. Large magneto-optic activity has been predicted and confirmed experimentally for (ferro)magnetic metal nanostructures coupled to plasmon resonances. [137, 139, 138, 144, 150, 152, 142] These effects are so strong that the enhanced polarizability of small metal clusters has been demonstrated to induce sizable magneto-optic signals even in nonmagnetic metals. [153]

Remarkably, the increased polarizability due to plasmons in ferromagnetic metal nanoparticles has been demonstrated to enable the manipulation of the light phase, adding a new handle to tune the magneto-optic properties, beyond pure enhancement effects. [148, 154]

However, shifting the attention from metal clusters to the optical properties of the dielectric host may bring about novel interesting features. In particular, magneto-optic materials with linear responses in the magnetic field –free of saturation– are coveted in applications for sensing, integrated optical communications or magneto-optic current transformers. [155]

In the quest of such prospects, transparent materials with large Verdet constants placed in external magnetic fields may offer an advantageous alternative to traditional Faraday rotators such as terbium gallium garnet (TGG) or yttrium iron garnet (YIG). Indeed, recent works have shown that polymers and glasses hosting nanoparticles exhibit large Faraday rotations up to around 300 rad/T-m, making them competitive compared to TGG or YIG. [156, 157]

In this context, the development of a comprehensive theoretical frame able to predict with high accuracy the magneto-optic response of composite dielectric/magnetic metal structures is a major step into a materials-design strategy towards advanced applications in biomedical/chemical sensing or optical communications. Yet, the lack of a theoretical model able to anticipate not only the optical response in-

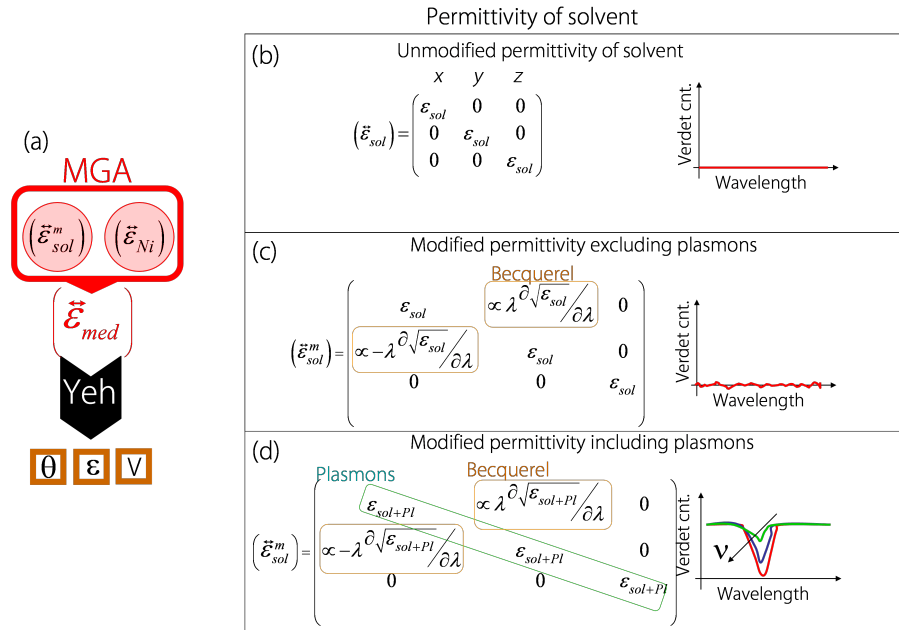


Figure 56: Sketch of the theoretical frame of our MEMT model. (a) The rotation ( $\theta$ ), ellipticity ( $\epsilon$ ) and Verdet constant ( $\mathcal{V}$ ) are obtained through the Yeh's formalism after the MGA model including the modified permittivity of solvent  $\bar{\epsilon}_{sol}^m$  and that of Ni,  $\bar{\epsilon}_{Ni}$ . (b) Permittivity tensor  $\bar{\epsilon}_{sol}$  of the solvent, as found in tables. (c) Permittivity tensor  $\bar{\epsilon}_{sol}^m$  modified to generate non-diagonal coefficients through Becquerel's formula, 26. (d) Permittivity tensor with diagonal components modified to include the plasmon LSPR polarizability and with non-diagonal coefficients generated through Becquerel's formula. Only the simultaneous inclusion of plasmon polarizability and Becquerel's law can reproduce the experimental large enhancement of the Verdet constant at the LSPR frequency.

trinsic to magnetic metal nanoclusters, but also the Verdet constant of the host material over a wide range of frequencies is a serious hindrance towards these objectives. Using nickel nanoparticles colloids as an illustrative example, we have accomplished such an achievement by formulating a theoretical frame that predicts with excellent accuracy the electromagnetic response of extremely diluted magnetic metal nanoparticles in liquids, finding very good accordance between theory and experiments. In particular, our model quantitatively describes the experimentally observed enhancement of the Verdet constant of the metal colloids, at frequencies close to their [LSPR](#). The key to such an excellent agreement between experiment and theory is based on the simultaneous incorporation of the magnetic induced optical response in the dielectric host in conjunction with the metal clusters polarizability. The scope of our theoretical model is far beyond the specific case of metal colloids, being readily extended to other complex structures including, e.g., polymers or glasses as dielectric hosts. This theory-experiment tandem allows us also envisioning plasmon-based sensing for ultrasensitive detection, whereby plasmonic shifts are interrogated by light polarization rather than by reflectance, permitting extreme sensitivity to tiny modifications of the plasmon resonator environments.

We have approached the problem of obtaining the magneto-optic response of extremely diluted magnetic nanoparticles ([MNP](#)) colloids –with concentrations in the ppm (parts per million) range– by outlining a [MEMT](#), see the sketch in figure [56 a](#). In the conditions of our experiments, the average [MNP](#) – [MNP](#) distance (around 200 – 500 nm in the range of approx. 6 – 48 ppm) was comparable to the wavelength at visible frequencies ( $\lambda = 400 - 850$  nm) and, therefore, we have used a [MGA](#) [[158](#), [159](#)] to model the full permittivity tensor  $\bar{\epsilon}_{med}$  in the diluted magnetic liquids (Figure [56 a](#)). Having obtained the effective  $\bar{\epsilon}_{med}$ , we have calculated the Faraday rotation and ellipticity using the Yeh’s formalism [[160](#), [161](#), [162](#), [163](#)] (see details in [14.2](#)). The main difficulty in this approach was the calculation of the effective permittivity tensor  $\bar{\epsilon}_{med}$  of the composite system, which is discussed in the following.

We anticipate that the [MGA](#) calculation of  $\bar{\epsilon}_{med}$  by simply taking the bulk permittivity of the host solvent  $\bar{\epsilon}_{sol}$  (hexane and toluene in our analysis) [[164](#)] and metal nanoparticles  $\bar{\epsilon}_{Ni}$  (nickel) [[165](#), [166](#)] completely fails at predicting any nonzero Verdet constant (figure [56 b](#)), in contradiction with the experimental data. However, we have found that the permittivity tensor  $\bar{\epsilon}_{sol}$  of the solvent has to be modified to  $\bar{\epsilon}_{med}^m$  according to two key ingredients that must be incorporated simultaneously into the model, affecting, respectively, the (i) diagonal and (ii) non-diagonal coefficients of the permittivity:

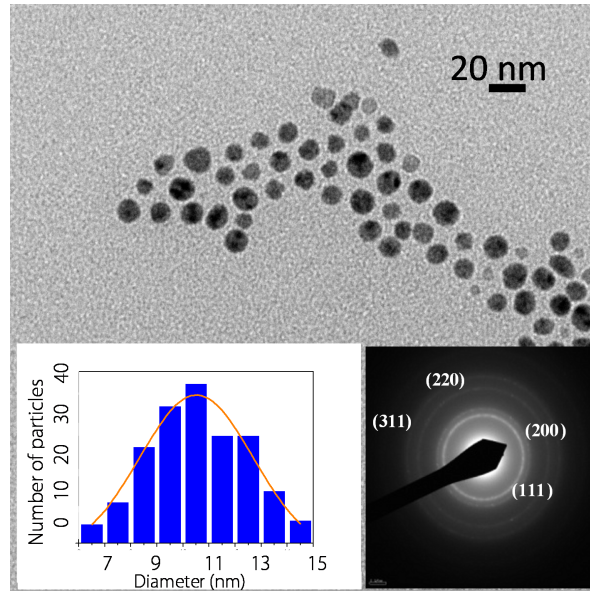


Figure 57: Transmission electron microscopy image of the Ni nanoparticles (diameter  $\phi = 10$  nm). Insets: Histogram of the particle size distribution fitted to a Gaussian function, showing a 20% polydispersity and SAED of metallic Ni.

(i) First, the diagonal terms  $\bar{\epsilon}_{solm,xx}$  must include an additional contribution from the resonant polarizability of the metal clusters, quantified as [107]

$$\alpha_{pl} = 3vV \frac{\epsilon_{sol} - \epsilon_{Ni}}{\epsilon_{sol} + 2\epsilon_{Ni}} = 1.8125 \times 10^{-29} m^3 \quad (24)$$

@ 589.8nm,  $v = 10^{-5}$

where  $\epsilon_{sol}$  is the solvent permittivity found in tables [164],  $V$  is the volume of the MNP and  $v$  is the volume fraction of the MNP. Note that the overall plasmonic polarizability  $\alpha_{pl}$  is dependent on the number of particles per unit volume - given by  $v$  - in the colloidal dispersions. The polarizability of the solvent can be obtained (figure 24) through the Lorentz-Lorenz relation

$$\alpha_{sol} = \frac{3M}{\rho N_A} \frac{\epsilon_{sol} - 1}{\epsilon_{sol} + 2} = 1.5259 \times 10^{-29} m^3 \quad (25)$$

@ 589.8nm

where  $M$  is the molar mass of the solvent,  $\rho$  its density and  $N_A$  is the Avogadro's number. Note that the two contributions are already comparable at 589.8nm with volume fraction of  $10^{-5}$ .

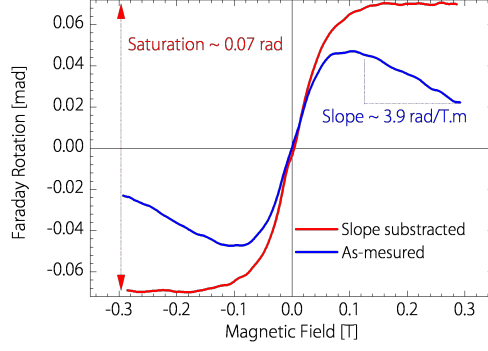


Figure 58: Faraday rotation loop measured at a wavelength  $\lambda = 800$  nm for Ni MNPs in hexane with concentration  $\nu \approx 36.6$  ppm. The figure illustrates how we obtained the saturated magneto-optic signals (displayed in figure 61) as well as the Faraday slopes (shown in figure 63).

Overall plasmonic polarizability is added to the polarizability of the solvent. Resulting polarizability leads to modified permittivity of the plasmonic solvent  $\bar{\epsilon}_{sol,xx}^m$  through equation 25:

$$\epsilon_{sol,xx} = \frac{\epsilon_{sol} + 2AC\nu V_p \frac{\rho}{M}}{1 - AC\nu V_p \frac{\rho}{M}}$$

$$A = \frac{(\epsilon_{Ni} - \epsilon_{sol})(2 + \epsilon_{sol})}{(\epsilon_{Ni} + 2\epsilon_{sol})}$$

where  $C = 4/3\pi N_A = 2.5225 \cdot 10^{24} \text{ mol}^{-1}$  is a constant and  $\frac{\rho}{M}$  is material dependent constant (for hexane ( $M_h = 86.18 \text{ g} \cdot \text{mol}^{-1}$ ,  $\rho_h = 654.8 \text{ kg} \cdot \text{m}^{-3}$ )  $\frac{\rho_h}{M_h} = 7598.1 \text{ mol} \cdot \text{m}^{-3}$ , toluene ( $M_t = 92.14 \text{ g} \cdot \text{mol}^{-1}$ ,  $\rho_t = 866.9 \text{ kg} \cdot \text{m}^{-3}$ )  $\frac{\rho_t}{M_t} = 9408.5 \text{ mol} \cdot \text{m}^{-3}$  and water ( $M_w = 18.02 \text{ g} \cdot \text{mol}^{-1}$ ,  $\rho_w = 1000 \text{ kg} \cdot \text{m}^{-3}$ )  $\frac{\rho_w}{M_w} = 55508 \text{ mol} \cdot \text{m}^{-3}$ ).

(ii) Secondly, the permittivity under an applied magnetic field acquires non-diagonal terms  $\bar{\epsilon}_{sol,xy}^m$  that are responsible for its Faraday rotation and Verdet constant. Defining  $z$  along the direction of light propagation and applied magnetic fields, only the non-diagonal permittivity components are nonzero (figure 56 c and d). They are calculated through the Becquerel's formula that gives the complex Verdet constant  $\mathcal{V}$  from the dispersion of the refractive index of the solvent [167]:

$$\mathcal{V} = \gamma \frac{e}{2mc} \lambda \frac{\partial n}{\partial \lambda} \quad (26)$$

Thus, the non-diagonal components of the modified solvent's permittivity are obtained as

$$\epsilon_{xy}^m = \frac{H_s \mathcal{V} \lambda n}{\pi} \quad (27)$$

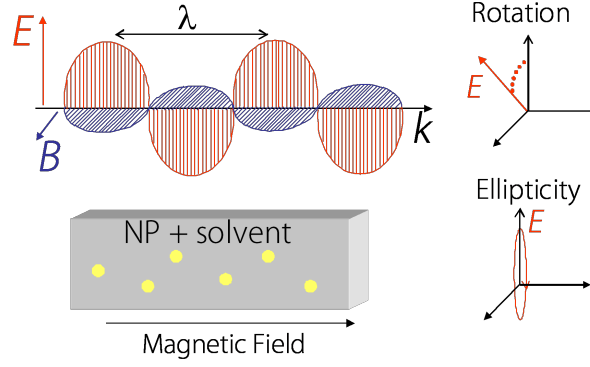


Figure 59: Schematics of the action of the magnetic colloidal system on the light polarization, whereby rotation and ellipticity are induced by the medium.

where  $H_s$  is the saturating field ( $\sim 1\text{kOe}$ ),  $\lambda$  the wavelength,  $e$  the electron charge,  $c$  the speed of light,  $m$  the electron mass, and  $\gamma$  is a magneto-optic anomaly correction taken here as  $\gamma = 0.63$  for hexane and  $\gamma = 0.525$  for toluene. [168, 169] The refractive index is  $n = \sqrt{\epsilon_{sol+pl}}$  or  $n = \sqrt{\epsilon_{sol}}$ , depending on whether plasmons are included or not in the calculations. The introduction of Becquerel's formula in the MEMT model has a dramatic effect: neglecting eq. 26 leads to the failure of the theory to describe any finite Verdet constant (figure 56 b). At the same time, even considering Becquerel's formula, the exclusion of plasmons in the model fails equally to describe the experimental data (figure 56 c). It is only the combined inclusion of Becquerel's formula and plasmon polarizability that describes correctly the largely enhanced Verdet constant at the LSPR frequencies (figure 56 on page 98).

At the final step, the global modified effective permittivity tensor of the hybrid medium, solvent + MNPs system, is given by the MGA expression: [158, 159]

$$\bar{\epsilon}_{med} = \bar{\epsilon}_{sol}^m + 3v\epsilon_{sol,xx}^m \left( \frac{\bar{\epsilon}_{NP} - \bar{\epsilon}_{sol}}{\bar{\epsilon}_{sol}^m + 2\bar{\epsilon}_{NP}} \right) \quad (28)$$

Hence, figure 28 condensates the essential of this MEMT model, from which we derive the tensor  $\bar{\epsilon}_{med}$  used in the Yeh's formalism to obtain the Faraday rotation and ellipticity of linearly polarized light transmitted through the nanoparticle colloids.

To test the accuracy of our MEMT model, we have confronted its predicted Faraday rotation and ellipticity to those measured for a several nickel MNP colloidal dispersions. Ni MNPs were prepared by a ligand stabilized solution-phase synthesis (see Refs. [121, 125] and the Experimental Section), obtaining MNPs with a mean diameter of 10 nm and a polydispersity of 20%, according to Gaussian profile of the size distribution (see figure 57 for a transmission electron microscopy image of the nanoparticles and insets with the particle



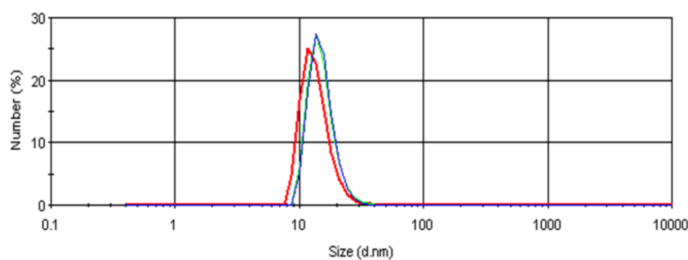


Figure 60: DLS hydrodynamic size (metal core with surfactants shell and a layer of solvent close to the particle) of the colloidal Ni MNPs suspended in hexane as investigated with a Zetasizer Nano ZS from Malvern Instruments equipped with a He/Ne 633 nm laser. Each measurement has 15 scans. As expected, the mean hydrodynamic diameter is bigger (15.2 nm) than the mean value for the diameter obtained by TEM.

size histogram and an indexed electron diffraction pattern of metallic nickel). After the synthesis and separation step, stable colloidal Ni dispersions in either hexane or toluene –with concentrations ranging from  $\nu = 6$  ppm (parts per million) to  $\nu = 48$  ppm– were prepared (figure 60 contains the hydrodynamic diameter distribution obtained by dynamic light scattering measurements). The magneto-optic response was measured in transmission (Faraday geometry, see figure 59) through the colloids contained in a sealed quartz vessel having an optical path of 0.5 cm. We used photoelastic modulation of the light polarization, where the detected signal was demodulated by a lock-in amplifier, being the first harmonic proportional to the ellipticity and the second harmonic to the rotation (see the Experimental Section and Refs [125, 120] for more technical details).

A typical Faraday rotation loop is depicted in figure 58. The plotted signal corresponds to Ni NPs of concentration  $\nu = 36.6$  ppm in hexane, and the loop was measured at a wavelength  $\lambda = 800$  nm. The loop shape is typical of a superparamagnet, as expected for the small size MNPs and in agreement with hysteretic loop and zero-field cooled/field cooled curves of similar Ni MNPs measured by SQUID magnetometry (see figure 62 and 64 ).

At high enough field, above  $B \approx 0.07$  T, a linear negative slope develops, that can be subtracted from the as-measured loop to obtain the saturated rotation/ellipticity (figure 58). The linear slope at high fields is mostly related to the Verdet constant of the solvent, whereas the saturated magneto-optic signal is mainly linked to the saturated magnetism of the Ni MNPs. Nevertheless, as shown in the following, the optical properties of the colloids are a complex cross-coupled interplay of the MNPs and solvent properties that can only be described in the frame of our MEMT picture.

Both Faraday rotation and ellipticity loops were measured in the visible range ( $\lambda = 400 - 850$  nm) from which we extracted the satu-

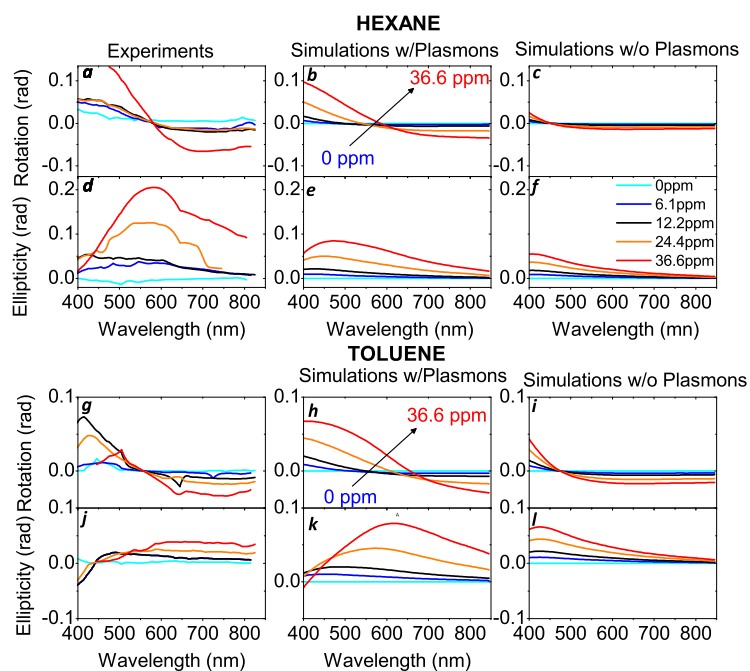


Figure 61: The saturated values extracted from the experimental magneto-optic loops are plotted as a function of the wavelength for Ni colloids for several concentrations in hexane –(a), (d)– and in toluene –(g), (j)–. The Faraday rotation and ellipticity spectra calculated from the MEMT model are shown in the rest of panels. In (b) and (e) –for hexane– and (h) and (k) –toluene–, the plasmonic polarizability of the metal nanoparticles was included in the MEMT simulations. In contrast, (c) and (f) –hexane– and (i) and (l) –toluene– display the spectra calculated by the MEMT model without including plasmons.

rated values of the Faraday rotation and ellipticity –in rad units, see figure 61– and their slopes –i.e., the complex Verdet constants given in units of rad/Tm, figure 63–. Focusing first on the saturated magneto-optic signals, we observed that the rotation spectra relatively weakly depended on the solvent host (hexane, figure 61 a or toluene, figure 61 g), whereas the saturated ellipticity spectra exhibited a more noticeable dependence on the solvent (figure 61 d and j, respectively). The moderate variations with the solvent of the saturated magneto-optic signals prove that the colloid optical properties were not only dependent on the MNPs, but were the consequence of the cross-coupled interactions of the solvent and MNPs properties.

Having measured the effect of the magnetic colloids on light polarization, we analyzed the effect of plasmon resonance on the observed magneto-optic spectra. The role of plasmons was quantitatively determined in our MEMT by comparing the predicted rotation and ellipticity spectra either with  $\alpha_{pl}=0$  –i.e., in the absence of LSPRs (figure 61 c, f, i and j) or including the plasmon polarizability given by 24 (figure 61 b, e, h and k). An inspection of the simulated spectra in figure 61 clearly reveals that the experimental data can be reproduced only when the plasmon polarizability is included in the MEMT model. Note, in particular, the excellent quantitative agreement between the simulated curves – figure 61 b, e, h and k– and the experimental spectra – figure 61 a, d, g and j –. Outstandingly, the excellent accordance between our MEMT model and the experimental data comes entirely from the input of bulk permittivity values obtained from the literature [164, 165, 166] and in the absence of any parameter fitting.

The wavelength-dependent Verdet constants were extracted from the measured rotation and ellipticity loop slopes at high fields. In figure 63 a and d we plotted the Faraday rotation and ellipticity slopes for hexane Ni MNPs colloids, after subtracting the spectrum corresponding to the pure hexane. By this way, we highlighted the effect on the Verdet constants after adding MNPs in the hexane. For both Faraday rotation and ellipticity slopes, the values corresponding to longer wavelengths were relatively small, below around 1 rad/Tm. For shorter wavelengths, however, the slopes got the maximum values,  $\sim 30$  rad/Tm in rotation, and  $\sim 4$  rad/Tm in ellipticity, respectively. The LSPR frequency, calculated at  $\lambda \approx 360$  nm, i.e., close to the rotation/ellipticity maxima (inset of figure 63e), had a dramatic effect on the emergence of these Verdet constants. In the absence of plasmons ( $\alpha_{pl} = 0$ ), the predicted rotation/ellipticity slopes were up to two orders of magnitude smaller than the experimental values (see figure 63 c and f). Conversely, by including the LSPRs in our MEMT model yielded the simulated curves plotted in figure 63 b and e, in very good agreement with the experimental spectra (figure 63 a and d). Note that –as mentioned above– a key term of our MEMT frame was the inclusion of the Becquerel’s formula [167] 26 to

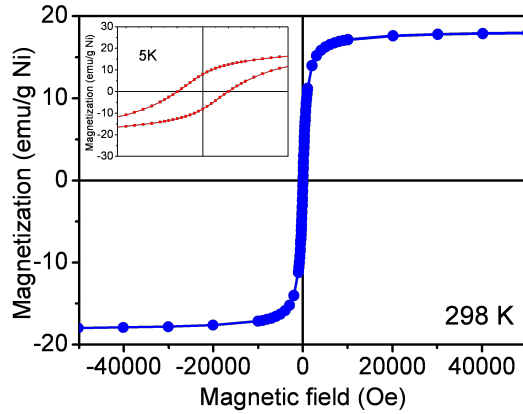


Figure 62: Magnetization versus magnetic field at 298K. Absence of remanence and coercivity signals the superparamagnetic character of the nanoparticles. Inset contained the  $M(H)$  at 5K and low fields where the ferromagnetic behaviour is evident. Magnetic characterization was performed with SQUID magnetometer (Quantum Design MPMS5XL) for a very similar system to the one studied with Ni nanoparticles of 8 nm mean diameter. The sample was prepared using a gelatine capsule filled with compacted cotton impregnated with 500  $\mu\text{l}$  Ni solution of known concentration. Magnetization data is presented in units of emu/g Ni.

generate the effective medium permittivity  $\bar{\epsilon}_{med}$ . A disregard of this basic fact leads automatically to the failure at predicting any nonzero Verdet constants, even considering the action of the plasmon polarizability. Therefore, a correct prediction of the optical response of dielectric/metal systems under magnetic fields definitely requires the inclusion of the off-diagonal components of the permittivity tensor of the nonmagnetic dielectric host.

Being established the prime role of LSPRs, further work should analyze whether a judicious choice of the metal/dielectric materials with specific shape, size and concentration of the metal clusters could be harnessed for optimum optical responses. The ultimate purpose may envision ultrasensitive plasmon-based sensing, relying on the use of light polarization rather than the conventional operation based on reflectance changes. [170, 171, 172] In particular, noble metal nanoparticles, such as Au, are more valuable candidates for LSPR-enhanced Verdet constants, as they exhibit resonances with significantly higher quality factors than 3d transition metals like Ni. Alternatively, a sizable magneto-optic activity has been measured in Au nanostructures at low magnetic fields, [153] making Au nanoparticles a good playground to test the effect of plasmons on the magneto-optic activity of diluted nonmagnetic metal colloids.

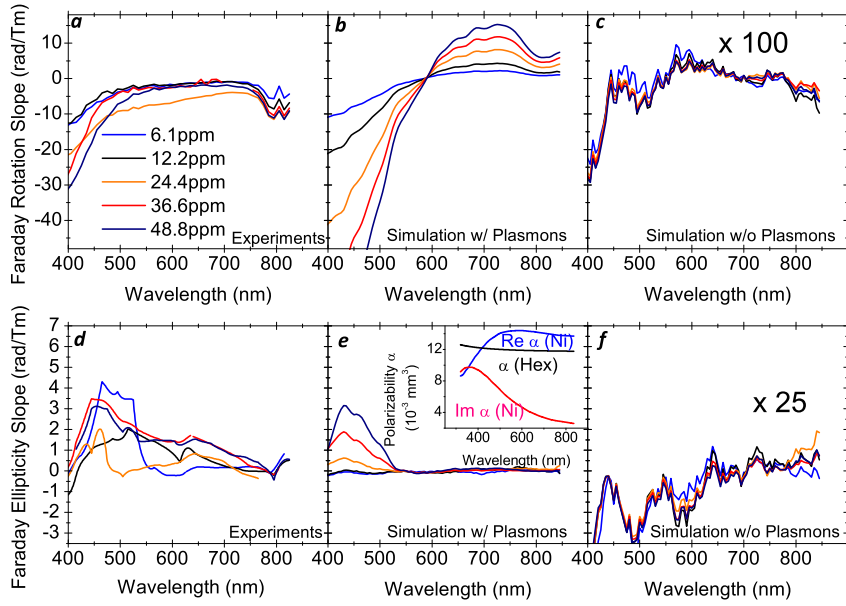


Figure 63: Faraday rotation and ellipticity slopes from which the Verdet constants were extracted as a function of the wavelength and concentration of Ni MNPs colloids in hexane. Panels (a) and (d) show the experimental data, whereas (b) and (d) display the calculated slopes from the MEMT model including the plasmon polarizability, and (c) and (d) the slopes calculated by MEMT without plasmons (note that in the latter the data was largely magnified in order to make it visible on the same scale). The inset in panel (e) shows the real and imaginary part of the polarizability of Ni MNPs in hexane,  $Re \alpha_{Ni}$  and  $Im \alpha_{Ni}$ , respectively, as well as the polarizability of hexane,  $\alpha_{hex}$ . The arrow in this inset signals the LSPR wavelength.

## 14.1 CONCLUSIONS

In summary, based on an effective medium approximation we have developed a theoretical framework that describes with high accuracy the experimental magnetic-optic response of diluted Ni metal colloids over the entire visible spectrum. A remarkable virtue of our theoretical model is its ability to predict not only the optical properties mostly related to the metal nanoparticles, but also the observed large enhancement of the Verdet constant at frequencies close to the localized surface plasmon resonance. The predictive character of our modified theory is based on the correct incorporation of the magnetic induced response of the dielectric host in conjunction with the metal cluster polarizability. In the absence of these two vital ingredients, any effective medium theory fails at foreseeing a sizable enhancement of the Verdet constant in these systems. Based on the exceptional accordance between theory and experiment, we envision our MEMT-based approach as a greatly versatile tool for materials design with targeted exceptional optical properties in applications of biochemical sensing and optical communications.

## 14.2 EXPERIMENTAL

In the following we describe briefly the details of modeling and experimental characterization that have been used to obtain the results analyzed in this chapter.

### 14.2.1 Simulation

The permittivity tensor obtained from our MEMT model was then used to model magneto-optical activity using Yeh's matrix formalism. [155, 156] The electro-magnetic response was obtained by solving  $4 \times 4$  Yeh's matrix  $\mathbb{M}$  as

$$\mathbf{E}^{(i)} = \mathbb{M}\mathbf{E}^{(o)} \quad (29)$$

where  $\mathbf{E}^{(i)}$  and  $\mathbf{E}^{(o)}$  are vectors of the complex amplitudes of the incident and the out-coming wave :

$$\mathbf{E} = (E_{R+}, E_{L-}, E_{L+}, E_{R-})^T \quad (30)$$

where  $E_{R+}$  is the complex amplitude of RCP light in the positive direction and  $E_{L-}$  is complex amplitude of LCP light in the negative direction and so on. The positive direction of the wave-vector is along the light propagation direction. The polarization states of the incident and transmitted waves are then defined by following complex ratios

$$\eta_i = \frac{E_{R+}^{(i)}}{E_{L+}^{(i)}}, \eta_t = \frac{E_{R+}^{(o)}}{E_{L+}^{(o)}} = \frac{-M_{13}}{M_{11}}\eta_i = \frac{M_{31}}{M_{33}}\eta_i \quad (31)$$

where  $M_{xx}$  are elements of Yeh's matrix  $\mathbb{M}$  from Eq. 29. The Faraday rotation and ellipticity are defined as

$$\theta_F = \text{Re}(\eta_t), \epsilon_F = \text{Im}(\eta_t). \quad (32)$$

#### 14.2.2 Magneto-optic characterization

We used a 150 W Xe arc lamp (ZolixTechnology) together with a monochromator (Zolix I-150). After collimation, the light was linearly polarized by a Glan-Thompson prism rotated  $45^\circ$  with respect to the modulator axis of a PEM. Light transmitted through the colloids impinged on a detector through a polarizing analyzer. The signal collected from the detector was brought to a lock-in amplifier synchronized to the frequency of the PEM (50 kHz). The Faraday rotation was obtained from

$$\theta_F = \frac{1}{4cJ_2(\varphi_0)} \frac{I_{2\omega}}{I_0}$$

and the Faraday ellipticity from

$$\epsilon_F = \frac{1}{4cJ_1(\varphi_0)} \frac{I_\omega}{I_0}$$

where  $J_N(\varphi_0)$  are the Bessel functions of the first kind and  $N$ th order, the PEM retardation angle was set to  $\varphi_0 = 137.8^\circ$ ,  $I_0$  is the dc-component of the detected light intensity, and  $I_\omega$ ,  $I_{2\omega}$  are the first and second harmonics of the detected light intensity as measured by the lock-in amplifier at the reference frequency of the PEM. The calibration constant  $c$  was determined experimentally.

#### 14.2.3 Synthesis and characterization of the Ni nanoparticles

Nickel nanoparticles were synthesized by high-temperature solution-phase method as reported in Reference [125]. For the studied particles, 2 mmol of Ni(acac)<sub>2</sub> (95%, Aldrich) were added to 14 ml oleylamine (70%, Aldrich), 2 mmol (0.63 ml) of oleic acid (99% Sigma-Aldrich) and 4 mmol trioctylphosphine (90%, Aldrich). The magnetically stirred mixture was heated to 130 °C and kept 20 min under a flow of high purity argon gas, followed by a further heating to 250 °C and maintaining at this temperature for 30 minutes. After cooling to room temperature, the nanoparticles were precipitated by adding excessive ethanol (as contra solvent) and separated by centrifugation. The as-prepared precipitate was dried at 60 °C overnight and then

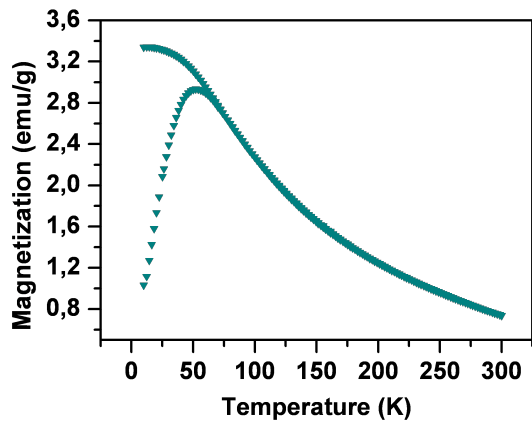


Figure 64: Field cooled-zero field cooled magnetization curves versus temperature measured with a 50 Oe applied field. The superparamagnetic character of the Ni nanoparticles is clearly demonstrated by those curves.

weighted. The resulting black precipitate could be redispersed in organic non-polar solvents such hexane or toluene. The concentration of a hexane batch was precisely determined by inductively coupled plasma mass spectrometry (ICP-MS) (9.8 mg/ml) and the measured samples were prepared by dilution to attain Ni concentrations of 6.1, 12.2, 24.4, 36.6 and 48.8 ppm.

TEM with SAED were used for morphological and structural characterization of the nanoparticles. TEM images were obtained using a JEOL 1210 electron microscope operating at 120 kV. A representative TEM image is shown in figure 57 where can be seen that the most particles are roughly spherical. Figure 57 also includes two insets with the particle size histogram and the indexed diffraction pattern for metallic Ni. Mean diameter and polydispersity of the system was determined by adjusting to a Gaussian distribution the particle size histogram of over 300 counts measured from several TEM images and using the imageJ software.

#### 14.2.4 Measurement Precision Factors

There is number of external factors that can influence the precision of measured data. Here is a numerical evaluation of several of them:

##### 14.2.4.1 Concentration

For very low volume fractions the effective permittivity of solvent with dispersed nanoparticles can be calculated as [159]:

$$\epsilon_e = \epsilon_{sol} \frac{\epsilon_{Ni}(1 + 2\nu) - \epsilon_{sol}(2\nu - 2)}{\epsilon_{sol}(2 + \nu) + \epsilon_{Ni}(1 - \nu)} \quad (33)$$



where  $\varepsilon_e$  is the effective permittivity of the system.  
For highly diluted colloidal dispersions  $\nu \ll 1$

$$\frac{\partial \varepsilon_e}{\partial \nu} = k_{Ni,sol}(\lambda) \quad (34)$$

where  $k_{Ni,sol} = 3\varepsilon_{sol} \frac{\varepsilon_{Ni} - \varepsilon_{sol}}{\varepsilon_{Ni} + 2\varepsilon_{sol}}$ .

#### 14.2.4.2 Evaporation

Rate of evaporation of solvent can influence measurement in case of uncovered liquid sample due to increasing volume fraction. Evaporated mass can be according to [173] approximated as

$$\Delta m = ktvMAPT^{-1} \quad (35)$$

where  $\Delta m$  [kg] is mass change,  $t$  [s] is time,  $k = 2.4 \times 10^{-4}$  is a general coefficient proposed by Stiver and Mackay,  $v$  [m/s] is air velocity,  $P$  [Pa] is vapour pressure of the solvent,  $M$  [kg/mol] is molecular weight,  $A$  [m<sup>2</sup>] is surface area and  $T$  [K] is ambient temperature.

The relative change of volume fraction is a proportional to relative change of volume as

$$\frac{\Delta \delta}{\delta} = \frac{\frac{\Delta V}{V}}{\frac{\Delta V}{V} - 1} \quad (36)$$

and the relative change of volume can be expressed as

$$\frac{\Delta V}{V} = \frac{ktvMP}{Th\rho} \quad (37)$$

Molecular weight of hexane is  $M = 0.086$  kg/mol its vapour pressure  $P = 20.5$ Pa and density  $\rho = 655$ kg/m<sup>3</sup>. If we assume air velocity  $v = 1$ m/s, normal room temperature  $T=298.15$ K and height of liquid column  $h = 1$ cm we can predict that the entire volume of hexane will evaporate in about 1h 17min and a change of volume fraction from 8ppm to 9ppm will take as little as 8.5 minutes. Use of sealed measurement container with minimum amount of air above the liquid is therefore required.



## CONCLUSIONS

---

### METHODS

The main achievement of this work was successful development of several measurement techniques for the characterization of ferroic systems. In particular, we have developed a confocal microscope with sensitivity to light polarization, able to map out with high accuracy and high resolution (well below the micron) the magneto-electric coupling emerging at interfaces buried well underneath the surface.

On the other hand, relevant improvements in the data processing and filtering in measurements exploiting magneto-optic Kerr spectroscopy in the visible, have allowed measuring the properties of extremely diluted magnetic colloid dispersions and of plasmon-sustaining surfaces covered with low concentrations of magnetic nanoparticles.

*A new magneto-optic laboratory –based on microscopy with light polarization– is now available at [ICMAB](#).*

### ANALYSIS OF MAGNETO-ELECTRIC COUPLING DYNAMICS

We have developed beyond-the-state-of-the-art optical tools to investigate the magneto-electric coupling in ferroelectric/ferromagnetic structures. In this line, the electric field frequency spectrum [MOKE](#) setup (high-frequency magneto-electric coupling ([HFMEC](#))) allowed for efficient separation of magneto-electric effects by their origin and measurement of magneto-electric coupling in magnetically non-saturated samples. Magneto-electric coupling was recorded in Cobalt on [PZT](#) substrates using [HFMEC](#) setup. Frequency spectrum analysis revealed that the surface mediated [MEC](#) was about 10 times stronger than the strain mediated [MEC](#).

*We have developed an unprecedented methodology allowing the disentanglement of different contributions to the magneto-electric coupling. More specifically, we were able to analyze separately the dynamics of the surface- and the strain- mediated magneto-electric coupling for frequencies up to around 200 kHz.*

### MAPPING OUT THE MAGNETO-ELECTRIC COUPLING

We found that this technique can also be used for quick in-situ evaluation of quality of ferromagnetic-ferroelectric interfaces. But probably the most important achievement was direct mapping of magneto-electric domains with submicronic resolution using the developed

polarization sensitive confocal microscope. A majority of the multiferroic systems researched at ICMA B are multiphase and the desired magneto-electric coupling happens at the interface between the two ferroic materials, usually tens of nanometers below the surface, while standard methods for studying the domain structure as magnetic force microscopy (MFM) and PFM are completely surface limited and therefore not applicable in this case.

*The magneto-electric coupling at an BTO/ LSMO interface buried about 150 nm below the surface was completely mapped out with a resolution of a few hundreds of nanometers. Magnetic domain imaging with PSCFM was demonstrated also on various samples. Imaging of ferro-electric domains is limited to materials that show ferroelectric domain bigger than the diffraction limit (400nm) and was demonstrated in LuMnO<sub>3</sub>.*

#### ANALYSIS OF THE INTERACTION OF PLASMONS WITH MAGNETO-OPTICS

Improvements of a magneto-optical spectroscope paved the way to an extensive study of the origin of magneto-optical enhancement in magnetic-plasmonic crystals. By this way, we analyzed how both propagating and localized surface plasmons were interacting with the magneto-optic properties of magnetic nanoparticles, and we identified the mechanisms whereby the magneto-optical activity was dramatically increased at the plasmon resonance frequency. We have also developed an effective medium theory that allows predicting with unprecedented accuracy the magneto-optical activity of hybrid metal/dielectric nanocomposites. A key aspect of this theory was the correct incorporation of the host dielectric optical properties into the model.

*An innovative theoretical frame, based on effective medium theory, was developed to anticipate the magneto-optic response of hybrid metal/dielectric nanocomposites in the visible range.*

## FURTHER DEVELOPMENT

---

There are many ways the functionality of measurement devices developed throughout this work can be extended and further developed. Keeping the door open for as many extensions as possible was one of the goals of the work. Where possible both hardware and software side was kept modular and the entire polarization sensitive confocal microscope has been kept fully cryostat ready.

In the next part I analyze the advantages and disadvantages of all projected scenarios for further development.

### CRYOGENIC MAGNETOELECTRIC COUPLING

As mentioned earlier, the polarization sensitive confocal microscope is entirely cryostat ready. The obvious next step would therefore be an inclusion of cryostat.

Temperature is an important dimension in the space of ferroic characterization, because both ferroelectric and ferromagnetic properties of most materials are strongly temperature dependent. Here achieved capability of quick direct magnetoelectric domain imaging even at buried interfaces wide opens a door to variety of possible experiments. We could witness disappearance of magneto-electric order upon crossing of Curie temperature, the critical temperature above which there is no ferroic order. Our previous experiments suggest that the loss of the order is not abrupt at all. Now we have a tool to observe this transition in real time.

Current setup does not allow for real time scanning but there are several approaches available to achieve this goal:

### SCANNING BEAM

There is an age old technique that harnesses the facility of deflecting the scanning beam instead of scanning the sample. This however means that most of the time the beam would not be passing through the center of the focusing lens. While this is acceptable for standard confocal microscopy where we are interested only in the intensity of reflected light, the situation is more complicated when the polarization is of interest. The rewards related to this achievement are too great not to try and overcome this problem.

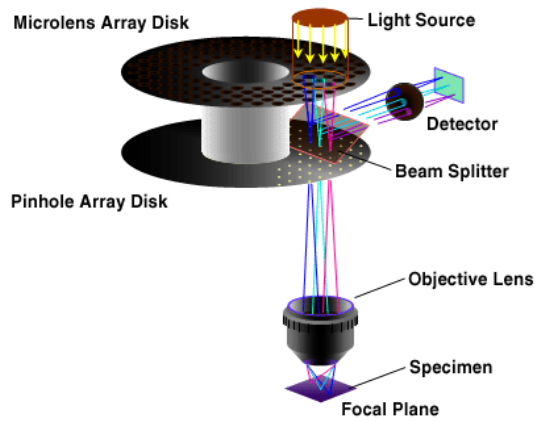


Figure 65: Basic principle of Yokogawa<sup>®</sup> disc confocal microscope

#### LENS ARRAY TECHNIQUES

There are many approaches to confocal microscopy that utilize an array of micro-metric lenses to create a set of simultaneous scanning beams and thus reduce measurement time [174] - for example Yokogawa<sup>®</sup> disc scanning microscope (see Figure 65). The obvious problem here is the availability of precise enough lenses so that there is minimal depolarization occurring on the microlenses.

#### WIDE FIELD MICROSCOPY

The sacrifice of confocal resolution for real-time imaging is probably not justifiable because of the typical size of the observed phenomena.

#### COMBINATION OF SCANNING PROBE AND CFM

A great aspect of confocal microscopy is that it can be readily combined with scanning probe microscopy to achieve both nanometric local resolution on the surface and diffraction limited resolution on a buried interface below.

There is of course an added advantage that such a system is in fact a scattering near-field optical microscope as well. The actual near-field enhancement of polarization sensitivity is unfortunately nowhere as great as one could expect due to a singularity at the apex of the tip.

An exciting possibility is to avoid this problem by functionalizing the tip of the scanning probe microscope. Nitrogen-vacancy pair in the structure of diamond [176, 175], for example, could take this function (see Figure 66). N-V pairs in diamond structure give rise to very unstable band structure which in turn makes this pair an excellent magnetic sensor capable of sensitivity down to single magnetic spin, in league with most potent currently available methods. N-V center

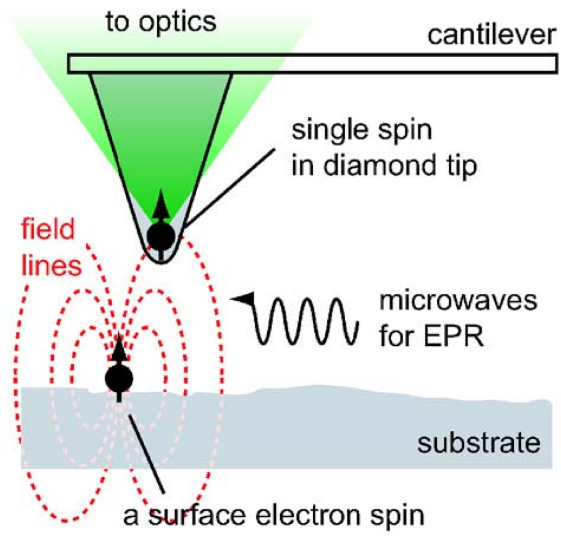


Figure 66: Basic principle of diamond magnetometer adapted from [175]

can be pumped and probed through the same lens and single electron spin sensitivity with AFM lateral resolution could be achieved.





## BIBLIOGRAPHY

---

- [1] B.E.A. Saleh and M.C. Teich. *Fundamentals of Photonics*. Wiley Series in Pure and Applied Optics. Wiley, 2007. ISBN 9780471358329. (Cited on pages 3, 40, and 68.)
- [2] O. Vlasin. *Magneto-optical Kerr effect Measurements at Low Temperatures*. Master Thesis. 2007. (Cited on page 6.)
- [3] J. C. Jacquet and T. Valet. A new magneto-optical effect discovered on magnetic multilayers: The magnetorefractive effect. *MRS Proceedings*, 384, 0 1995. ISSN null. doi: 10.1557/PROC-384-477. URL [http://journals.cambridge.org/article\\_S1946427400323703](http://journals.cambridge.org/article_S1946427400323703). (Cited on page 9.)
- [4] Jose Manuel Caicedo Roque. Magneto-optical spectroscopy of complex systems: Magnetic oxides and photonic crystals. *ICMAB*, 2012. URL <http://www.tesisenred.net/bitstream/handle/10803/96793/jmcr1de1.pdf?sequence=1>. (Cited on pages 9 and 15.)
- [5] Chiara Marchiori Christophe Rossel Marta D. Rossell Rolf Erni Daniele Caimi Marilyne Sousa Alexei Chelnokov Bert J. Offrein Stefan Abel, Thilo Stöferle. A strong electro-optically active lead-free ferroelectric integrated on silicon, 2013. URL <http://www.nature.com/ncomms/journal/v4/n4/full/ncomms2695.html>. (Cited on page 10.)
- [6] Rober E. Newnham. *Properties of Materials: Anisotropy, Symmetry, Structure*. Oxford University Press, UK, 2005. (Cited on page 10.)
- [7] J.P. Joule. Xvii. on the effects of magnetism upon the dimensions of iron and steel bars. *Philosophical Magazine Series 3*, 30(199):76–87, 1847. doi: 10.1080/14786444708645656. URL <http://www.tandfonline.com/doi/abs/10.1080/14786444708645656>. (Cited on page 11.)
- [8] E. Villari. *Ann. Phys. Chem.* 126, 87 (1865), 126(87), 1865. (Cited on page 11.)
- [9] J. C. Kemp. Basic laboratory set-up for various measurements possible with the photoelastic modulator. *Application note, Hinds Instruments, Inc.*, 1975. (Cited on page 17.)
- [10] Robert H Webb. Confocal optical microscopy. *Rep. Prog. Phys.*, 59:427–472, 1996. (Cited on pages 23 and 52.)

- [11] T. Choi, Y. Horibe, H. T. Yi, Y. J. Choi, W. Wu, and S. . Cheong. Insulating interlocked ferroelectric and structural antiphase domain walls in multiferroic  $\text{ymno}_3$ . *Nature Materials*, 9(3):253–258, 2010. URL <http://www.nature.com/nmat/journal/v9/n3/full/nmat2632.html>. (Cited on page 28.)
- [12] W. Eerenstein, N. D. Mathur, and J. F. Scott. Multiferroic and magnetoelectric materials. *Nature*, 442(7104):759–765, 2006. doi: 10.1038/nature05023. URL <http://dx.doi.org/10.1038/nature05023>. (Cited on page 39.)
- [13] Agnès Barthélémy Manuel Bibes. Multiferroics: Towards a magnetoelectric memory, 2008. URL <http://www.nature.com/nmat/journal/v7/n6/full/nmat2189.html>. (Cited on page 39.)
- [14] Evgeny Y. Tsymbal. Spintronics: Electric toggling of magnets, 2011. URL <http://www.nature.com/nmat/journal/v11/n1/full/nmat3205.html>. (Cited on page 39.)
- [15] Nico Dix, Rajaram Muralidharan, Jose-Manuel Rebled, Sonia Estradé, Francesca Peiró, Manuel Varela, Josep Fontcuberta, and Florencio Sánchez. Selectable spontaneous polarization direction and magnetic anisotropy in  $\text{bifeo}_3\text{-cofe}_{204}$  epitaxial nanostructures. *ACS Nano*, 4(8):4955–4961, 2010. doi: 10.1021/nn101546r. URL <http://pubs.acs.org/doi/abs/10.1021/nn101546r>. (Cited on pages 39 and 62.)
- [16] W. Eerenstein, M. Wiora, J. L. Prieto, J. F. Scott, and N. D. Mathur. Giant sharp and persistent converse magnetoelectric effects in multiferroic epitaxial heterostructures. *Nature Materials*, 6:21–29, 2007. (Cited on pages 39 and 61.)
- [17] J. Ma, J. M. Hu, L. Li, and C.-W. Nan. Recent progress in multiferroic magnetoelectric composites: from bulk to thin films. *Adv. Mater.*, 23:1062–1087, 2011. (Cited on pages 39 and 61.)
- [18] N. Lei, T. Devolder, G. Agnus, P. Aubert, L. Daniel, J. . Kim, W. Zhao, T. Trypiniotis, R. P. Cowburn, C. Chappert, D. Ravelosona, and P. Lecoeur. Strain-controlled magnetic domain wall propagation in hybrid piezoelectric/ferromagnetic structures. *Nature Communications*, 4, 2013. (Cited on page 39.)
- [19] M. Weisheit, S. Fähler, A. Marty, Y. Souche, C. Poinson, and D. Givord. Electric field-induced modification of magnetism in thin-film ferromagnets. *Science*, 315(5810):349–351, 2007. (Cited on page 39.)
- [20] Chun-Gang Duan, Julian P. Velev, R. F. Sabirianov, Ziqiang Zhu, Junhao Chu, S. S. Jaswal, and E. Y. Tsymbal. Surface magnetoelectric effect in ferromagnetic metal films. *Phys. Rev.*

- Lett.*, 101:137201, Sep 2008. doi: 10.1103/PhysRevLett.101.137201. URL <http://link.aps.org/doi/10.1103/PhysRevLett.101.137201>. (Cited on pages 39 and 62.)
- [21] T. Maruyama. Large voltage-induced magnetic anisotropy change in a few atomic layers of iron. *Nature Nanotechnology*, 4 (227201):158–161, 2009. URL [10.1103/PhysRevLett.97.227201](http://link.aps.org/doi/10.1103/PhysRevLett.97.227201). (Cited on pages 39 and 61.)
- [22] A. Mardana, S. Ducharme, and S. Adenwalla. Ferroelectric control of magnetic anisotropy. *Nano Letters*, 11(9):3862–3867, 2011. (Cited on pages 39 and 62.)
- [23] Y. Geng, H. Das, A. L. Wysocki, X. Wang, S. . Cheong, M. Mostovoy, C. J. Fennie, and W. Wu. Direct visualization of magnetoelectric domains. *Nature Materials*, 2013. Article in Press. (Cited on page 39.)
- [24] T. Hoffmann, P. Thiel, P. Becker, L. Bohat and M. Fiebig. Time-resolved imaging of magnetoelectric switching in multiferroic  $\text{mnwo}_4$ . *Physical Review B - Condensed Matter and Materials Physics*, 84(18), 2011. (Cited on page 40.)
- [25] A. Glavic, C. Becher, J. Voigt, E. Schierle, E. Weschke, M. Fiebig, and T. Brückel. Stability of spin-driven ferroelectricity in the thin-film limit: Coupling of magnetic and electric order in multiferroic  $\text{tbmno}_3$  films. *Physical Review B - Condensed Matter and Materials Physics*, 88(5), 2013. (Cited on page 40.)
- [26] R. M. Corn and D. A. Higgins. Optical second harmonic generation as a probe of surface chemistry. *Chemical reviews*, 94(1): 107–125, 1994. (Cited on page 40.)
- [27] A. Zvezdin and V. Kotov. *Modern Magneto-optics and Magneto-optical Materials*. Taylor & Francis: London, 2007. (Cited on page 40.)
- [28] S. Abel, T. Stöferle, C. Marchiori, C. Rossel, M. D. Rossell, R. Erni, D. Caimi, M. Sousa, A. Chelnokov, B. J. Offrein, and J. Fompeyrine. A strong electro-optically active lead-free ferroelectric integrated on silicon. *Nature Communications*, 4, 2013. (Cited on page 40.)
- [29] R.E. Newnham. *Properties of Materials: Anisotropy, Symmetry, Structure*. Oxford Univ. Press, 2005. (Cited on page 41.)
- [30] T. H. E. Lahtinen, J. O. Tuomi, and S. Van Dijken. Pattern transfer and electric-field-induced magnetic domain formation in multiferroic heterostructures. *Advanced Materials*, 23(28):3187–3191, 2011. (Cited on page 41.)

- [31] T. H. E. Lahtinen, Y. Shirahata, L. Yao, K. J. A. Franke, G. Venkataiah, T. Taniyama, and S. Van Dijken. Alternating domains with uniaxial and biaxial magnetic anisotropy in epitaxial Fe films on BaTiO<sub>3</sub>. *Applied Physics Letters*, 101(26), 2012. (Cited on page 41.)
- [32] T. H. E. Lahtinen, K. J. A. Franke, and S. Van Dijken. Electric-field control of magnetic domain wall motion and local magnetization reversal. *Scientific Reports*, 2, 2012. (Cited on page 41.)
- [33] A. J. Millis. Lattice effects in magnetoresistive manganese perovskites. *Nature*, 392(6672):147–150, 1998. (Cited on page 41.)
- [34] E. Dagotto, T. Hotta, and A. Moreo. Colossal magnetoresistant materials: The key role of phase separation. *Physics Report*, 344(1-3):1–153, 2001. (Cited on page 41.)
- [35] H. H. Wieder. Electrical behavior of barium titanate single crystals at low temperatures. *Physical Review*, 99(4):1161–1165, 1955. (Cited on page 41.)
- [36] I. Fina, N. Dix, J. M. Rebled, Marti X. Gemeiner, P. F. Peiro, B. Dkhil, F. Sanchez, L. Fabrega, and J. Fontcuberta. The direct magnetoelectric effect in ferroelectric-ferromagnetic epitaxial heterostructures. *Nat. Comm.*, 4:1378, 2013. (Cited on pages 44 and 61.)
- [37] M. Scigaj, N. Dix, I. Fina, R. Bachelet, B. Warot-Fonrose, J. Fontcuberta, and F. Sánchez. Ultra-flat BaTiO<sub>3</sub> epitaxial films on Si(001) with large out-of-plane polarization. *Applied Physics Letters*, 102(11), 2013. (Cited on page 44.)
- [38] A. Schilling, T. B. Adams, R. M. Bowman, J. M. Gregg, G. Catalan, and J. F. Scott. Scaling of domain periodicity with thickness measured in BaTiO<sub>3</sub> single crystal lamellae and comparison with other ferroics. *Phys. Rev. B*, 74:024115, Jul 2006. doi: 10.1103/PhysRevB.74.024115. URL <http://link.aps.org/doi/10.1103/PhysRevB.74.024115>. (Cited on page 48.)
- [39] R.H. Webb. Separate interface and strain-mediated converse magnetoelectric coupling dynamics in Co/Pb(Zr<sub>0.2</sub>Ti<sub>0.8</sub>)O<sub>3</sub> bilayers. 2013. (Cited on page 56.)
- [40] C. A. F. Vaz, J. Hoffman, C. H. Ahn, and R. Ramesh. Magnetoelectric coupling effects in multiferroic complex oxide composite structures. *Advanced Materials*, 22(26-27):2900–2918, 2010. (Cited on pages 57 and 62.)
- [41] M. Stengel, D. Vanderbilt, and N. A. Spaldin. Enhancement of ferroelectricity at metal-oxide interfaces. *Nature Materials*, 8(5):392–397, 2009. (Cited on page 57.)

- [42] L. Pintilie, I. Vrejoiu, D. Hesse, and M. Alexe. The influence of the top-contact metal on the ferroelectric properties of epitaxial ferroelectric  $\text{Pb}(\text{Zr}_{0.2}\text{Ti}_{0.8})\text{O}_3$  thin films. *Journal of Applied Physics*, 104(11), 2008. (Cited on page 57.)
- [43] G. C. Milward, M. J. Calderón, and P. B. Littlewood. Electronically soft phases in manganites. *Nature*, 433(7026):607–610, 2005. (Cited on page 57.)
- [44] N. Mathur and P. Littlewood. Mesoscopic texture in manganites. *Physics Today*, 56(1):25–30, 2003. (Cited on page 57.)
- [45] C. Aruta, G. Ghiringhelli, V. Bisogni, L. Braicovich, N. B. Brookes, A. Tebano, and G. Balestrino. Orbital occupation, atomic moments, and magnetic ordering at interfaces of manganite thin films. *Physical Review B - Condensed Matter and Materials Physics*, 80(1), 2009. (Cited on page 57.)
- [46] X. Hong, A. Posadas, A. Lin, and C. H. Ahn. Ferroelectric-field-induced tuning of magnetism in the colossal magnetoresistive oxide  $\text{La}_{1-x}\text{Sr}_x\text{MnO}_3$ . *Physical Review B - Condensed Matter and Materials Physics*, 68(13):1344151–1344155, 2003. (Cited on page 57.)
- [47] A. K. Debnath and J. G. Lin. Current-induced giant electroresistance in  $\text{La}_{0.7}\text{Sr}_{0.3}\text{MnO}_3$  thin films. *Physical Review B - Condensed Matter and Materials Physics*, 67(6):644121–644125, 2003. (Cited on page 57.)
- [48] C. Thiele, K. Dörr, L. Schultz, E. Beyreuther, and W. . Lin. Piezoelectrically induced resistance modulations in  $\text{La}_{0.7}\text{Sr}_{0.3}\text{MnO}_3/\text{Pb}(\text{Zr,Ti})\text{O}_3$  field effect devices. *Applied Physics Letters*, 87(16):1–3, 2005. (Cited on page 57.)
- [49] A. S. Dhoot, C. Israel, X. Moya, N. D. Mathur, and R. H. Friend. Large electric field effect in electrolyte-gated manganites. *Physical Review Letters*, 102(13), 2009. (Cited on page 57.)
- [50] H. J. A. Molegraaf, J. Hoffman, C. A. F. Vaz, S. Gariglio, D. Van Der Morel, C. H. Ahn, and J. . Triscone. Magnetoelectric effects in complex oxides with competing ground states. *Advanced Materials*, 21(34):1–5, 2009. (Cited on page 57.)
- [51] C. . Chong, D. Hsu, W. . Chen, C. . Li, Y. . Huang, H. . Han, J. G. Lin, L. . Chen, K. . Chen, and Y. . Chen. Giant room temperature electric-field-assisted magnetoresistance in  $\text{La}_{0.7}\text{Sr}_{0.3}\text{MnO}_3/\text{NiSi}$  nanotip heterojunctions. *Nanotechnology*, 22(12), 2011. (Cited on page 57.)
- [52] M. Uehara, S. Mori, C. H. Chen, and S. . Cheong. Percolative phase separation underlies colossal magnetoresistance

- in mixed-valent manganites. *Nature*, 399(6736):560–563, 1999. (Cited on page 57.)
- [53] M. Fäth, S. Freisem, A. A. Menovsky, Y. Tomioka, J. Aarts, and J. A. Mydosh. Spatially inhomogeneous metal-insulator transition in doped manganites. *Science*, 285(5433):1540–1542, 1999. (Cited on page 57.)
- [54] Ch Renner, G. Aeppli, B. . Kim, Y. . Soh, and S. . Cheong. Atomic-scale images of charge ordering in a mixed-valence manganite. *Nature*, 416(6880):518–521, 2002. (Cited on page 57.)
- [55] L. Zhang, C. Israel, A. Biswas, R. L. Greene, and A. De Lozanne. Direct observation of percolation in a manganite thin film. *Science*, 298(5594):805–807, 2002. (Cited on page 57.)
- [56] K. H. Ahn, T. Lookman, and A. R. Bishop. Strain-induced metal-insulator phase coexistence in perovskite manganites. *Nature*, 428(6981):401–404, 2004. (Cited on page 57.)
- [57] Y. . Soh, G. Aeppli, N. D. Mathur, and M. G. Blamire. Temperature dependent phenomena in  $\text{La}_{1-x}\text{Sr}_x\text{MnO}_3$  films studied by magnetic force microscopy. *Journal of Applied Physics*, 87(9 III): 6743–6745, 2000. (Cited on page 57.)
- [58] Y. . Soh, G. Aeppli, N. D. Mathur, and M. G. Blamire. Mesoscale magnetism at the grain boundaries in colossal magnetoresistive films. *Physical Review B - Condensed Matter and Materials Physics*, 63(2):204021–204024, 2001. (Cited on page 57.)
- [59] Nicola A. Spaldin and Manfred Fiebig. The renaissance of magnetoelectric multiferroics. *Science*, 309(5733):391–392, 2005. doi: 10.1126/science.1113357. URL <http://www.sciencemag.org/content/309/5733/391.short>. (Cited on page 61.)
- [60] R. Ramesh and N. Spaldin. Multiferroics: progress and prospects in thin films. *Nature Materials*, 6:348–351, 2007. (Cited on page 61.)
- [61] M. Bibes and Barthélémy. Giant sharp and persistent converse magnetoelectric effects in multiferroic epitaxial heterostructures. *Nature Materials*, 7:425–426, 2008. (Cited on page 61.)
- [62] M. Bibes. Nanoferronics is a winning combination. *Nature Materials*, 11:354–357, 2012. (Cited on page 61.)
- [63] M. Buzzi, R. V. Chopdekar, J. L. Hockel, A. Bur, T. Wu, N. Pilet, P. Warnicke, G. P. Carman, L. J. Heyderman, and F. Nolting. Single domain spin manipulation by electric fields in strain coupled artificial multiferroic nanostructures. *Phys. Rev. Lett.*, 111:027204, Jul 2013. doi: 10.1103/PhysRevLett.111.



027204. URL <http://link.aps.org/doi/10.1103/PhysRevLett.111.027204>. (Cited on page 61.)

- [64] S. Valencia, A. Crassous, L. Bocher, V. Garcia, X. Moya, R. O. Cherifi, C. Deranlot, K. Bouzehouane, S. Fusil, A. Zobelli, A. Gloter, N. D. Mathur, A. Gaupp, R. Abrudan, F. Radu, A. Barthélémy, and M. Bibes. Interface-induced room-temperature multiferroicity in batio<sub>3</sub>. *Nature Materials*, 10(10):753–758, 2011. (Cited on pages 61 and 62.)
- [65] V. Laukhin, V. Skumryev, and X. Marti. Electric-field control of exchange bias in multiferroic epitaxial heterostructures. *Physical Review Letters*, 97(227201), 2006. URL [10.1103/PhysRevLett.97.227201](http://link.aps.org/doi/10.1103/PhysRevLett.97.227201). (Cited on page 61.)
- [66] V. Garcia. Ferroelectric control of spin polarization. *Science*, 327:1106–1110, 2010. (Cited on page 61.)
- [67] V. Skumryev. Magnetization reversal by electric-field decoupling of magnetic and ferroelectric domain walls in multiferroic-based heterostructures. *Phys. Rev. Lett.*, 106(057206), 2011. (Cited on page 61.)
- [68] Y. Shiota, T. Nozaki, F. Bonell, S. Murakami, T. Shinjo, and Y. Suzuki. Induction of coherent magnetization switching in a few atomic layers of fco using voltage pulses. *Nat. Mater.*, 11:39–43, 2012. (Cited on page 61.)
- [69] W. G. Wang, M. G. Li, S. Hageman, and C. L. Chien. Electric-field-assisted switching in magnetic tunnel junctions. *Nat. Mater.*, 11:64–68, 2012. (Cited on page 61.)
- [70] Y. Shiota, S. Miwa, T. Nozaki, F. Bonell, N. Mizuochi, T. Shinjo, H. Kubota, S. Yuasa, and Y. Suzuki. Pulse voltage-induced dynamic magnetization switching in magnetic tunneling junctions with high resistance-area product. *Applied Physics Letters*, 101(10), 2012. (Cited on page 61.)
- [71] A. Pimenov, A. A. Mukhin, V. Y. Ivanov, V. D. Travkin, A. M. Balbashov, and A. Loidl. Possible evidence for electromagnons in multiferroic manganites. *Nature Physics*, 2(2):97–100, 2006. (Cited on page 61.)
- [72] A. B. Sushkov, R. V. Aguilar, S. Park, S. . Cheong, and H. D. Drew. Electromagnons in multiferroic ymn<sub>2</sub>o<sub>5</sub> and tbn<sub>2</sub>o<sub>5</sub>. *Physical Review Letters*, 98(2), 2007. (Cited on page 61.)
- [73] A. Pimenov, A. Shuvaev, A. Loidl, F. Schrettle, A. A. Mukhin, V. D. Travkin, V. Y. Ivanov, and A. M. Balbashov. Magnetic and magnetoelectric excitations in tbn<sub>3</sub>o<sub>3</sub>. *Physical Review Letters*, 102(10), 2009. (Cited on page 61.)

- [74] M. Mochizuki and N. Nagaosa. Theoretically predicted picosecond optical switching of spin chirality in multiferroics. *Physical Review Letters*, 105(14), 2010. (Cited on page 61.)
- [75] Y. Takahashi, R. Shimano, Y. Kaneko, H. Murakawa, and Y. Tokura. Magnetoelectric resonance with electromagnons in a perovskite helimagnet. *Nature Physics*, 8(2):121–125, 2012. (Cited on page 61.)
- [76] Y. Takahashi, Y. Yamasaki, and Y. Tokura. Terahertz magnetoelectric resonance enhanced by mutual coupling of electromagnons. *Physical Review Letters*, 111(3), 2013. (Cited on page 61.)
- [77] J. Wang, J. B. Neaton, H. Zheng, V. Nagarajan, S. B. Ogale, B. Liu, D. Viehland, V. Vaithyanathan, D. G. Schlom, U. V. Waghmare, N. A. Spaldin, K. M. Rabe, M. Wuttig, and R. Ramesh. Epitaxial bifeo<sub>3</sub> multiferroic thin film heterostructures. *Science*, 299(5613):1719–1722, 2003. (Cited on page 61.)
- [78] S. . Cheong and M. Mostovoy. Multiferroics: A magnetic twist for ferroelectricity. *Nature Materials*, 6(1):13–20, 2007. (Cited on page 61.)
- [79] H. Zheng, J. Wang, S. E. Lofland, Z. Ma, L. Mohaddes-Ardabili, T. Zhao, L. Salamanca-Riba, S. R. Shinde, S. B. Ogale, F. Bai, D. Viehland, Y. Jia, D. G. Schlom, M. Wuttig, A. Roytburd, and R. Ramesh. Multiferroic batio<sub>3</sub>-cofe<sub>2</sub>o<sub>4</sub> nanostructures. *Science*, 303(5658):661–663, 2004. doi: 10.1126/science.1094207. URL <http://www.sciencemag.org/content/303/5658/661.abstract>. (Cited on page 62.)
- [80] M. Liu, O. Obi, J. Lou, Y. Chen, Z. Cai, S. Stoute, M. Espanol, M. Lew, X. Situ, K. S. Ziemer, V. G. Harris, and N. X. Sun. Giant electric field tuning of magnetic properties in multiferroic ferrite/ferroelectric heterostructures. *Advanced Functional Materials*, 19(11):1826–1831, 2009. (Cited on page 62.)
- [81] Jia-Mian Hu and C. W. Nan. Electric-field-induced magnetic easy-axis reorientation in ferromagnetic/ferroelectric layered heterostructures. *Phys. Rev. B*, 80:224416, Dec 2009. doi: 10.1103/PhysRevB.80.224416. URL <http://link.aps.org/doi/10.1103/PhysRevB.80.224416>. (Cited on page 62.)
- [82] Tao Wu, Alexandre Bur, Ping Zhao, Kotekar P. Mohanchandra, Kin Wong, Kang L. Wang, Christopher S. Lynch, and Gregory P. Carman. Giant electric-field-induced reversible and permanent magnetization reorientation on magnetoelectric ni/(011) [pb(mg<sub>1/3</sub>nb<sub>2/3</sub>)o<sub>3</sub>](1-x)-[pbtio<sub>3</sub>]x heterostructure. *Applied Physics Letters*, 98(1):012504, 2011. doi: <http://dx>.



- doi.org/10.1063/1.3534788. URL <http://scitation.aip.org/content/aip/journal/apl/98/1/10.1063/1.3534788>. (Cited on page 62.)
- [83] J. T. Heron, M. Trassin, K. Ashraf, M. Gajek, Q. He, S. Y. Yang, D. E. Nikonov, Y-H. Chu, S. Salahuddin, and R. Ramesh. Electric-field-induced magnetization reversal in a ferromagnet-multiferroic heterostructure. *Phys. Rev. Lett.*, 107:217202, Nov 2011. doi: 10.1103/PhysRevLett.107.217202. URL <http://link.aps.org/doi/10.1103/PhysRevLett.107.217202>. (Cited on page 62.)
- [84] S. Zhang, Y. G. Zhao, P. S. Li, J. J. Yang, S. Rizwan, J. X. Zhang, J. Seidel, T. L. Qu, Y. J. Yang, Z. L. Luo, Q. He, T. Zou, Q. P. Chen, J. W. Wang, L. F. Yang, Y. Sun, Y. Z. Wu, X. Xiao, X. F. Jin, J. Huang, C. Gao, X. F. Han, and R. Ramesh. Electric-field control of nonvolatile magnetization in  $\text{Co}_{40}\text{Fe}_{40}\text{B}_{20}/\text{Pb}(\text{Mg}_{1/3}\text{Nb}_{2/3})_{0.7}\text{Ti}_{0.3}\text{O}_3$  structure at room temperature. *Phys. Rev. Lett.*, 108:137203, Mar 2012. doi: 10.1103/PhysRevLett.108.137203. URL <http://link.aps.org/doi/10.1103/PhysRevLett.108.137203>. (Cited on page 62.)
- [85] C A F Vaz. Electric field control of magnetism in multiferroic heterostructures. *Journal of Physics: Condensed Matter*, 24(33):333201, 2012. URL <http://stacks.iop.org/0953-8984/24/i=33/a=333201>. (Cited on page 62.)
- [86] Z. G. Sheng, J. Gao, and Y. P. Sun. Coaction of electric field induced strain and polarization effects in  $\text{La}_{0.7}\text{Ca}_{0.3}\text{MnO}_3\text{PmNPT}$  structures. *Phys. Rev. B*, 79:174437, May 2009. doi: 10.1103/PhysRevB.79.174437. URL <http://link.aps.org/doi/10.1103/PhysRevB.79.174437>. (Cited on page 62.)
- [87] Q. X. Zhu, W. Wang, S. W. Yang, X. M. Li, Y. Wang, H.-U. Habermeier, H. S. Luo, H. L. W. Chan, X. G. Li, and R. K. Zheng. Coaction and competition between the ferroelectric field effect and the strain effect in  $\text{Pr}_{0.5}\text{Ca}_{0.5}\text{MnO}_3$  film/ $\text{Pb}(\text{Mg}_{1/3}\text{Nb}_{2/3})\text{O}_3$ - $\text{PbTiO}_3$  crystal heterostructures. *Applied Physics Letters*, 101(17):172906, 2012. doi: <http://dx.doi.org/10.1063/1.4761948>. URL <http://scitation.aip.org/content/aip/journal/apl/101/17/10.1063/1.4761948>. (Cited on page 62.)
- [88] Tao Jiang, Shengwei Yang, Yukuai Liu, Yuewei Yin, Sing Dong, Wenbo Zhao, and Xiaoguang Li. Coaction and distinguishment of converse piezoelectric and field effects in  $\text{La}_{0.7}\text{Ca}_{0.3}\text{MnO}_3/\text{SrTiO}_3$ / $\text{Pb}(\text{Mg}_{1/3}\text{Nb}_{2/3})\text{O}_3$ - $\text{PbTiO}_3$  heterostructures. *Applied Physics Letters*, 103(5):053504, 2013. doi: <http://dx.doi.org/10.1063/1.4817018>.

URL <http://scitation.aip.org/content/aip/journal/apl/103/5/10.1063/1.4817018>. (Cited on page 62.)

- [89] Chun-Gang Duan, S. S. Jaswal, and E. Y. Tsymbal. Predicted magnetoelectric effect in Fe/batio<sub>3</sub> multilayers: Ferroelectric control of magnetism. *Phys. Rev. Lett.*, 97:047201, Jul 2006. doi: 10.1103/PhysRevLett.97.047201. URL <http://link.aps.org/doi/10.1103/PhysRevLett.97.047201>. (Cited on page 62.)
- [90] J. D. Burton and E. Y. Tsymbal. Magnetoelectric interfaces and spin transport. *Philosophical Transactions of the Royal Society A: Mathematical, Physical and Engineering Sciences*, 370(1977):4840–4855, 2012. (Cited on page 62.)
- [91] S. Cao, P. Liu, J. Tang, H. Lu, C. . Bark, S. Ryu, C. B. Eom, A. Gruverman, and P. A. Dowben. Magnetoelectric coupling at the euo/batio<sub>3</sub> interface. *Applied Physics Letters*, 102(17), 2013. (Cited on page 62.)
- [92] Laura Bocher, Alexandre Gloter, Arnaud Crassous, Vincent Garcia, Katia March, Alberto Zobelli, Sergio Valencia, Shaima Enouz-Vedrenne, Xavier Moya, Neil D. Marthur, Cyrile Deranlot, Stéphane Fusil, Karim Bouzehouane, Manuel Bibes, Agnes Barthélémy, Christian Colliex, and Odile Stéphan. Atomic and electronic structure of the batio<sub>3</sub>/fe interface in multi-ferroic tunnel junctions. *Nano Letters*, 12(2):1113–1113, 2012. doi: 10.1021/nl300315t. URL <http://pubs.acs.org/doi/abs/10.1021/nl300315t>. (Cited on page 62.)
- [93] M. Ye. Zhuravlev, R. F. Sabirianov, S. S. Jaswal, and E. Y. Tsymbal. Giant electroresistance in ferroelectric tunnel junctions. *Phys. Rev. Lett.*, 94:246802, Jun 2005. doi: 10.1103/PhysRevLett.94.246802. URL <http://link.aps.org/doi/10.1103/PhysRevLett.94.246802>. (Cited on page 62.)
- [94] P. Hejda. Simple representation of magnetic characteristics by smooth functions. *Czechoslovak Journal of Physics*, 35(4):442–458, 1985. (Cited on page 67.)
- [95] C. Hermann. Surface-enhanced magneto-optics in metallic multilayer films. *Phys. Rev. B: Condens. Matter Mater. Phys.*, 64:235422, 2001. (Cited on page 77.)
- [96] J. B. González-Díaz, García-Martín A., Armelles G., García-Martín J. M., Clavero C., Cebollada A., Lukaszew R. A., Skuza J. R., Kumah D. P., and Clarke R. Surface-magnetoplasmon non-reciprocity effects in noble-metal/ferromagnetic heterostructures. *Phys. Rev. B: Condens. Matter Mater. Phys.*, 76:153402, 2007. (Cited on pages 77 and 87.)

- [97] V. V. Temnov. Active magneto-plasmonics in hybrid metal-ferromagnet structures. *Nat. Photonics*, 4:107, 2010. (Cited on page 77.)
- [98] G. Ctistis. Optical and magnetic properties of hexagonal arrays of subwavelength holes in optically thin cobalt films. *Nano Lett.*, 9:1, 2009. (Cited on page 77.)
- [99] E. T. Papaioannou. Magneto-optic enhancement and magnetic properties in fe antidot films with hexagonal symmetry. *Phys. Rev. B: Condens. Matter Mater. Phys.*, 81:054424, 2010. (Cited on page 77.)
- [100] J. F. Torrado. Plasmon induced modification of the transverse magneto-optical response in fe antidot arrays. *Phys. Status Solidi RRL*, 4:271, 2010. (Cited on page 77.)
- [101] J. F. Torrado. Tunable magneto-photon response of nickel nanostructures. *Appl. Phys. Lett.*, 99:193109, 2011. (Cited on page 77.)
- [102] E. T. Papaioannou. Surface plasmons and magneto-optic activity in hexagonal ni anti-dot arrays. *Opt. Express*, 19:23867, 2011. (Cited on page 77.)
- [103] V. I. Belotelov. Enhanced magneto-optical effects in magneto-plasmonic crystals. *Nat. Nanotechnol.*, 6:370, 2011. (Cited on page 77.)
- [104] G. X. Du. Evidence of localized surface plasmon enhanced magneto-optical effect in nanodisk array. *Appl. Phys. Lett.*, 96:081915, 2010. (Cited on page 77.)
- [105] J. Chen. Plasmonic nickel nanoantennas. *Small*, 7:2341, 2011. (Cited on page 77.)
- [106] D. M. Newman. Magneto-optic behaviour in the presence of surface plasmons. *J. Phys.: Condens. Matter*, 20:345230, 2008. (Cited on page 78.)
- [107] S. A. Maier. Plasmonics: Fundamentals and applications. *Springer Science + Business Media LLC: New York*, 2007. (Cited on pages 79, 85, 87, and 100.)
- [108] N. G. Tognalli. From single to multiple ag-layer modification of au nanocavity substrates: A tunable probe of the chemical surface-enhanced raman scattering mechanism. *ACS Nano*, 5:5433, 2011. (Cited on page 79.)
- [109] N. Tognalli. Sers in pah-os and gold nanoparticle self-assembled multilayers. *J. Chem. Phys.*, 123:044707, 2005. (Cited on page 79.)

- [110] K. Takahashi. Study on magnetophotonic crystals for use in reflection-type magneto-optical spatial light modulators. *J. Appl. Phys.*, 103:07B331, 2008. (Cited on page 79.)
- [111] J. V. Boriskina. Enhancement of the magnetorefractive effect in magnetophotonic crystals. *Phys. Solid State*, 48:717, 2006. (Cited on page 79.)
- [112] A. A. Fedyanin. Enhanced faraday and nonlinear magneto-optical kerr effects in magnetophotonic crystals. *J. Magn. Magn. Mater.*, 282:256, 2004. (Cited on page 79.)
- [113] M. Inoue. Magnetophotonic crystals. *J. Phys. D: Appl. Phys.*, 39:R151, 2006. (Cited on page 79.)
- [114] A. K. Zvezdin. Magneto-optical properties of two dimensional photonic crystals. *Eur. Phys. J. B*, 37:479, 2004. (Cited on pages 79 and 86.)
- [115] N. Liu. Three-dimensional photonic metamaterials at optical frequencies. *Nat. Mater.*, 7:31, 2008. (Cited on page 79.)
- [116] M. Fang. Effect of embedding  $Fe_3O_4$  nanoparticles in silica spheres on the optical transmission properties of three-dimensional magnetic photonic crystals. *J. Appl. Phys.*, 108:103501, 2010. (Cited on page 79.)
- [117] I. Simkiene. Magneto-optics of opal crystals modified by cobalt nanoparticles. *Lith. J. Phys.*, 50:7, 2010. (Cited on page 79.)
- [118] V. V. Pavlov. Optical study of three-dimensional magnetic photonic crystals opal/ $Fe_3O_4$ . *J. Magn. Magn. Mater.*, 321:840, 2009. (Cited on page 79.)
- [119] J. M. Caicedo. Facile route to magnetophotonic crystals by infiltration of 3d inverse opals with magnetic nanoparticles. *J. Magn. Magn. Mater.*, 322:1494, 2010. (Cited on page 79.)
- [120] J. M. Caicedo. Magnetophotonic response of three-dimensional opals. *ACS Nano*, 5:2957, 2011. (Cited on pages 79 and 103.)
- [121] O. Pascu. Ultrathin conformal coating for complex magnetophotonic structures. *Nanoscale*, 3:4811, 2011. (Cited on pages 79 and 102.)
- [122] E. Yablonovitch. Photonics: One-way road for light. *Nature*, 461:744, 2009. (Cited on page 79.)
- [123] P. N. Bartlett, J. J. Baumberg, Peter R. Birkin, M. A. Ghanem, and M. C. Netti. Highly ordered macroporous gold and platinum films formed by electrochemical deposition through templates assembled from submicron diameter monodisperse

- polystyrene spheres. *Chemistry of Materials*, 14(5):2199–2208, 2002. doi: 10.1021/cm011272j. URL <http://pubs.acs.org/doi/abs/10.1021/cm011272j>. (Cited on page 79.)
- [124] P. D. Lacharmoise. Imaging optical near fields at metallic nanoscale voids. *Phys. Rev. B: Condens. Matter Mater. Phys.*, 78:125410, 2008. (Cited on page 79.)
- [125] O. Pascu. Magneto-optical characterization of colloidal dispersions. application to nickel nanoparticles. *Langmuir*, 26:12548, 2010. (Cited on pages 80, 102, 103, and 109.)
- [126] Oana Pascu. *Synthesis of Magnetic Nanoparticles and Strategies Towards Magneto-photonic Materials*. Doctoral Thesis - UAB, 2012. (Cited on page 80.)
- [127] T. A. Kelf. Localized and delocalized plasmons in metallic nanovoids. *Phys. Rev. B: Condens. Matter Mater. Phys.*, 74:245415, 2006. (Cited on pages 83, 84, 85, and 90.)
- [128] R. M. Cole. Understanding plasmons in nanoscale voids. *Nano Lett.*, 7:2094, 2007. (Cited on page 83.)
- [129] N. G. Tognalli. Incident wavelength resolved resonant sers on au sphere segment void (ssv) arrays. *J. Phys. Chem. C*, 116:3414, 2012. (Cited on pages 83, 84, and 85.)
- [130] M. Fox. Optical properties of solids. *Oxford University Press:Oxford*, 2001. (Cited on page 85.)
- [131] D. R. Lide. Crc handbook of chemistry and physics. *CRC Press*, 1996. (Cited on page 85.)
- [132] P. Nordlander. Plasmon hybridization in nanoparticle dimers. *Nano Lett.*, 4:899, 2004. (Cited on page 85.)
- [133] J. Jung. Electrostatic plasmon resonances of metal nanospheres in layered geometries. *Phys. Rev. B: Condens. Matter Mater. Phys.*, 81:125413, 2010. (Cited on page 85.)
- [134] V. Antonov. Electronic structure and magneto-optical properties of solids. *Springer: New York*, 2004. (Cited on page 86.)
- [135] E. Snoeks. Measuring and modifying the spontaneous emission rate of erbium near an interface. *Phys. Rev. Lett.*, 74:2459, 1995. (Cited on page 87.)
- [136] J. B. González-Díaz. Plasmon-enhanced magneto-optical activity in ferromagnetic membranes. *Appl. Phys. Lett.*, 94:263101, 2009. (Cited on page 87.)

- [137] P. M. Hui and D. Stroud. Theory of faraday rotation by dilute suspensions of small particles. *Applied Physics Letters*, 50(15): 950–952, 1987. (Cited on page 97.)
- [138] Y. Li, Q. Zhang, A. V. Nurmikko, and S. Sun. Enhanced magneto-optical response in dumbbell-like ag-cofe<sub>2</sub>o<sub>4</sub> nanoparticle pairs. *Nano Letters*, 5(9):1689–1692, 2005. (Cited on page 97.)
- [139] T. K. Xia, P. M. Hui, and D. Stroud. Theory of faraday rotation in granular magnetic materials. *J. Appl. Phys.*, 67(6):2736–2741, 15 March 1990. (Cited on page 97.)
- [140] M. Abe. Derivation of nondiagonal effective dielectric-permeability tensors for magnetized granular composites. *Phys. Rev. B*, 53(11):7065–7075, 15 March 1996. (Cited on page 97.)
- [141] Ch.-Y. You, S.-Ch. Shin, and S.-Y. Kim. Modified effective-medium theory for magneto-optical spectra of magnetic materials. *Phys. Rev. B*, 55(9):5953–5958, 1 March 1997. (Cited on page 97.)
- [142] M. Barthélémy and D. J. Bergman. Faraday effect in composites. *Physical Review B - Condensed Matter and Materials Physics*, 58(19): 12770–12781, 1998. (Cited on page 97.)
- [143] X. P. Miao, L. Gao, and P. Xu. Faraday magneto-optical rotation in compositionally graded films. *Journal of Applied Physics*, 103(2), 2008. (Cited on page 97.)
- [144] P. K. Jain, Y. Xiao, R. Walsworth, and A. E. Cohen. Surface plasmon resonance enhanced magneto-optics (supremo): Faraday rotation enhancement in gold-coated iron oxide nanocrystals. *Nano Letters*, 9(4):1644–1650, 2009. (Cited on page 97.)
- [145] R. K. Dani, H. Wang, S. H. Bossmann, G. Wysin, and V. Chikan. Faraday rotation enhancement of gold coated fe<sub>2</sub>o<sub>3</sub> nanoparticles: Comparison of experiment and theory. *Journal of Chemical Physics*, 135(22), 2011. (Cited on page 97.)
- [146] S. Pakdel and M. Miri. Faraday rotation and circular dichroism spectra of gold and silver nanoparticle aggregates. *Physical Review B - Condensed Matter and Materials Physics*, 86(23), 2012. (Cited on page 97.)
- [147] A. Mendoza-Galván, K. Järrendahl, A. Dmitriev, T. Pakizeh, M. Käll, and H. Arwin. Optical response of supported gold nanodisks. *Optics Express*, 19(13):12093–12107, 2011. (Cited on page 97.)
- [148] V. Bonanni, S. Bonetti, T. Pakizeh, Z. Pirzadeh, J. Chen, J. Nogués, P. Vavassori, R. Hillenbrand, J. Åkerman, and

- A. Dmitriev. Designer magnetoplasmonics with nickel nanoferromagnets. *Nano Letters*, 11(12):5333–5338, 2011. (Cited on page 97.)
- [149] J. C. Banthí, D. Meneses-Rodríguez, F. García, M. U. González, A. García-Martín, A. Cebollada, and G. Armelles. High magneto-optical activity and low optical losses in metal-dielectric au/co/au-sio<sub>2</sub> magnetoplasmonic nanodisks. *Advanced Materials*, 24(10):OP36–OP41, 2012. (Cited on page 97.)
- [150] G. Armelles, A. Cebollada, A. García-Martín, and M. U. González. Magnetoplasmonics: Combining magnetic and plasmonic functionalities. *Advanced Optical Materials*, 1(1):10–35, 2013. (Cited on page 97.)
- [151] F. Pineider, C. De Julián Fernández, V. Videtta, E. Carlino, A. Al Hourani, F. Wilhelm, A. Rogalev, P. D. Cozzoli, P. Ghigna, and C. Sangregorio. Spin-polarization transfer in colloidal magnetic-plasmonic au/iron oxide hetero-nanocrystals. *ACS Nano*, 7(1):857–866, 2013. (Cited on page 97.)
- [152] M. Rubio-Roy, O. Vlašín, O. Pascu, J. M. Caicedo, M. Schmidt, A. R. Goñi, N. G. Tognalli, A. Fainstein, A. Roig, and G. Herranz. Magneto-optical enhancement by plasmon excitations in nanoparticle/metal structures. *Langmuir*, 28(24):9010–9020, 2012. doi: 10.1021/la301239x. URL <http://pubs.acs.org/doi/abs/10.1021/la301239x>. (Cited on page 97.)
- [153] B. Sepúlveda, J. B. González-Díaz, A. García-Martín, L. M. Lechuga, and G. Armelles. Plasmon-induced magneto-optical activity in nanosized gold disks. *Physical Review Letters*, 104(14), 2010. (Cited on pages 97 and 106.)
- [154] N. Maccaferri, A. Berger, S. Bonetti, V. Bonanni, M. Kataja, Q. H. Qin, S. Van Dijken, Z. Pirzadeh, A. Dmitriev, J. Nogués, J. Åkerman, and P. Vavassori. Tuning the magneto-optical response of nanosize ferromagnetic ni disks using the phase of localized plasmons. *Physical Review Letters*, 111(16), 2013. (Cited on page 97.)
- [155] S. Vandendriessche, S. Van Cleuvenbergen, P. Willot, G. Henrich, M. Srebro, V. K. Valev, G. Koeckelberghs, K. Clays, J. Autschbach, and T. Verbiest. Giant faraday rotation in mesogenic organic molecules. *Chemistry of Materials*, 25(7):1139–1143, 2013. (Cited on pages 97 and 108.)
- [156] P. Gangopadhyay, R. Voorakaranam, A. Lopez-Santiago, S. Fossier, J. Thomas, R. A. Norwood, A. Persoons, and N. Peyghambarian. Faraday rotation measurements on thin films of regioregular alkyl-substituted polythiophene derivatives. *Jour-*



- nal of Physical Chemistry C*, 112(21):8032–8037, 2008. (Cited on pages 97 and 108.)
- [157] G. Kumar, S. K. Apte, S. N. Garaje, M. V. Kulkarni, S. M. Mahajan, and B. B. Kale. Magneto-optic characteristics of ferric oxide quantum-dot-phosphate glass nanocomposite. *Applied Physics A: Materials Science and Processing*, 98(3):531–535, 2010. (Cited on page 97.)
- [158] O. Levy and D. Stroud. Maxwell garnett theory for mixtures of anisotropic inclusions: Application to conducting polymers. *Physical Review B - Condensed Matter and Materials Physics*, 56(13): 8035–8046, 1997. (Cited on pages 99 and 102.)
- [159] J. C. Maxwell Garnett. Colours in metal glasses, in metallic films, and in metallic solutions. ii. *Philosophical Transactions of the Royal Society of London. Series A, Containing Papers of a Mathematical or Physical Character*, 205:237–288, 1906. ISSN 02643952. URL <http://www.jstor.org/stable/90933>. (Cited on pages 99, 102, and 110.)
- [160] Pochi Yeh. Optics of anisotropic layered media: A new  $4 \times 4$  matrix algebra. *Surf. Sci.*, 96:41–53, 1980. (Cited on page 99.)
- [161] S. Višňovský. Magneto-optical ellipsometry. *Czechoslovak Journal of Physics*, 36(5):625–650, 1986. (Cited on page 99.)
- [162] S. Višňovský, V. Pařízek, M. Nývlt, P. Kielar, V. Prosser, and R. Krishnan. Magneto-optical kerr spectra of nickel. *Journal of Magnetism and Magnetic Materials*, 127(1-2): 135–139, 1993. doi: DOI:10.1016/0304-8853(93)90206-H. URL <http://www.sciencedirect.com/science/article/B6TJJ-46GD1T0-10R/2/1b6b1150ca4b4a11f22bad2f8543fb1a>. (Cited on page 99.)
- [163] Š. Višňovský, R. Lopušník, M. Bauer, J. Bok, J. Rassbender, and B. Hillebrands. Magneto-optic ellipsometry in multilayers at arbitrary magnetization. *Opt. Express*, 9:121–135, 2001. URL <http://www.opticsexpress.org/oearchive/source/33990.htm>. (Cited on page 99.)
- [164] K. Kerl and H. Varchmin. Refractive index dispersion (rid) of some liquids in the uv/vis between 20 deg. c and 60 deg. c. *Journal of Molecular Structure*, 349:257 – 260, 1995. ISSN 0022-2860. doi: DOI:10.1016/0022-2860(95)08758-N. URL <http://www.sciencedirect.com/science/article/B6TGS-3YMMH6-12/2/81cace405277fc0d8520bc20a40db50e>. *Molecular Spectroscopy and Molecular Structure* 1994. (Cited on pages 99, 100, and 105.)



- [165] E. D. Palik, editor. *Handbook of Optical Constants of Solids I, II, III*. Academic Press, 1991. (Cited on pages 99 and 105.)
- [166] P. B. Johnson and R. W. Christy. Optical constants of copper and nickel as a function of temperature. *Phys. Rev. B*, 11(4): 1315–1323, Feb 1975. doi: 10.1103/PhysRevB.11.1315. (Cited on pages 99 and 105.)
- [167] J. V. Vlek. *The Theory Of Electric And Magnetic Susceptibilities*. Oxford University Press, 1932. (Cited on pages 101 and 105.)
- [168] A. Balbin Villaverde and D. A. Donatti. Verdet constant of liquids; measurements with a pulsed magnetic field. *The Journal of Chemical Physics*, 71(10):4021–4024, 1979. doi: 10.1063/1.438169. URL <http://link.aip.org/link/?JCP/71/4021/1>. (Cited on page 102.)
- [169] C. G. Darwin and W. H. Watson. The constants of the magnetic dispersion of light. *Proceedings of the Royal Society of London. Series A, Containing Papers of a Mathematical and Physical Character*, 114(768):474–490, 1927. ISSN 09501207. URL <http://www.jstor.org/stable/94823>. (Cited on page 102.)
- [170] B. Sepúlveda, A. Calle, L. M. Lechuga, and G. Armelles. Highly sensitive detection of biomolecules with the magneto-optic surface-plasmon-resonance sensor. *Optics Letters*, 31(8):1085–1087, 2006. (Cited on page 106.)
- [171] D. Regatos, B. Sepúlveda, D. Farina, L. G. Carrascosa, and L. M. Lechuga. Suitable combination of noble/ferromagnetic metal multilayers for enhanced magneto-plasmonic biosensing. *Optics Express*, 19(9):8336–8346, 2011. (Cited on page 106.)
- [172] J. Homola. Surface plasmon resonance sensors for detection of chemical and biological species. *Chemical reviews*, 108(2):462–493, 2008. (Cited on page 106.)
- [173] W. Stiver and D. Mackay. A spill hazard ranking system for chemicals. *Environment Canada First Technical Spills Seminar, Toronto, Canada*, 1993. (Cited on page 111.)
- [174] A. Orth and K. B. Crozier. Scanning confocal microscopy with a microlens array. *Frontiers in Optics*, (FWS7), 2011. (Cited on page 116.)
- [175] C. L. Degen. Scanning magnetic field microscope with a diamond single-spin sensor, 2008. (Cited on pages 116 and 117.)
- [176] Kevin Kai Chang. *Custom built atomic force microscope for nitrogen-vacancy diamond magnetometry*. Massachusetts Institute of Technology, 2011. URL <http://hdl.handle.net/1721.1/68549>. (Cited on page 116.)